Advancements in Optically Detected Nuclear Magnetic Resonance Applied to Nanoscopic GaAs/AlGaAs Heterostructures

Dissertation for the degree of

Doktor der Naturwissenschaften

in the Fachbereich Physik
at the University of Dortmund

by Björn Lenzmann

Dortmund, September 2001

To my parents and my wife

Acknowledgement

As with any work of substantial nature, it could not have been completed without the help of many others.

I would like to thank Prof. Dr. Dieter Suter, my doctoral supervisor, for the freedom in scientific reasearch and the opportunity to develop my own ideas. Without his guidance this thesis would never have come to life.

Thanks must, of course, be extended to Prof. Dr. "A.P." Sophia Hayes, my favorite chemisist who was a reliable and tireless research partner in- and outside the lab. Her benchmarking brought out the best in me. I wish her the best of luck.

Marcus Eickhoff, my labmate, gave me his tremendous support on every challenge to be conquered. Many thanks for his immense patience and best wishes for his scientific career.

It has been my pleasure to collaborate with Dr. Gregory Flinn who introduced me into optical spectroscopy and ODNMR.

I acknowledge Dr. Soheyla Eshlaghi and Prof. Dr. Andreas Wieck from Ruhruniversität Bochum. Without the samples grown by them none of the experiments in this thesis could have been conducted.

Not to be forgotten Prof. Dr. Ullrich Pietsch from Universität Potsdam. He and his group supported the simulation of internal strain distribution in chapter 6.

Many thanks belong also to the Präparationslabor and the Werkstatt of Universität Dortmund. Without their little pieces and devices built and grown for my lab and the experiments some of my ideas would never have been realized.

I would like to thank the "Graduiertenkolleg Festkörperphysik" of Universität Dortmund for financial funding of my project.

Contents

1 Introduction **1**
1.1 Background . . . 2
1.2 Outline . . . 3

2 Quantum Well Properties **5**
2.1 Sample Properties . . . 6
2.2 Optical Properties . . . 8
2.2.1 Band Structure . . . 8
2.2.2 Photoluminescence . . . 9
2.2.3 Optical Pumping . . . 11

3 The ODNMR Spectrometer **15**
3.1 Introduction . . . 16
3.2 Experimental Setup . . . 16
3.3 Laser . . . 18
3.4 Detection of Polarization . . . 19
3.5 Optical Spectrometer . . . 21
3.6 Optical Cryostat . . . 21
3.7 External B_0 Field . . . 22
3.8 Radio Frequency Field . . . 22
3.9 Data Acquisition and Evaluation . . . 25

4 Coupling of Electron and Nuclear Spin Systems **27**
4.1 Optical Pumping . . . 28
4.1.1 The Coupling Constant . . . 28
4.1.2 Nuclear Magnetic Field . . . 30
4.1.3 Electronic Magnetic Field . . . 32
4.1.4 Dynamic Nuclear Polarization . . . 33
4.1.5 Electron Localization . . . 35
4.2 Optical Detection . . . 37
4.2.1 The Hanle Effect in an External Field . . . 38

4.2.2 Influence of Nuclear Fields 41
4.3 Experimental Results 44
4.3.1 Hanle Curves 44
4.3.2 Direct Measurement of the Nuclear Field 49
4.4 Summary 52

5 Nuclear Magnetic Resonance 55
5.1 Introduction 56
5.2 Resonance Spectra 57
5.2.1 Simulation of NMR Spectra 62
5.2.2 Results of Simulation 65
5.3 Relaxation Times 68
5.3.1 "Dark" Relaxation 69
5.3.2 Pumping Time 70
5.4 Adiabatic Rapid Passage 72
5.5 Summary 76

6 Electric Quadrupole Effects 77
6.1 Introduction 78
6.2 Quadrupole Splitting 78
6.3 Resonance Line Splitting 80
6.4 Internal Strain 82
6.5 External Strain 90
6.6 Electric Field Effects 94
6.7 Summary 95

7 Conclusions 96

Chapter 1

Introduction

1.1 Background

Nuclear magnetic resonance (NMR) has been a powerful tool in the determination of condensed phase structures since its introduction. Its ability for studying both static and dynamic behaviour makes it very attractive for the research of nanostrucures in semiconductor systems. The resonance transitions of the istopes within the solid can provide details about lattice defects, dopants or strain through line shifts, splittings and broadening of the resonance lines. Semiconductor heterostructures forming low dimensional systems like quantum wells or quantum dots are often only a few monolayers thick. It can therefore be expected that for those small systems, the lattice deviates from a perfect structure, an effect that should be visible in NMR experiments.

The method of conventional NMR is limited, though, in two ways: for thermal polarization a sufficiently high number of spins are needed ($N > 10^{18}$) in order to achieve the necessary signal-to-noise ratio; and since signals are a bulk average, it is not possible to distinguish signals from the quantum well under investigation from signals in the barrier or the substrate. One way to overcome these limitations of the conventional NMR method is to incorporate optical techniques.

Optical pumping of the conduction band electrons of a semiconductor material creates a huge polarization of the electron spin system which is transferred to the nuclear system, analogous to the Overhauser effect in metals [1]. This effect has been first achieved in semiconductors by Georges Lampel [2] who optically pumped the ^{29}Si isotopes in n-type silicon. Due to the vast increase of nuclear polarization, the number of nuclei needed for NMR detection is reduced by several orders of magnitude. Since the changes of polarization in the nuclear system are transferred back by the same mechanism to the electron spins, it is possible to detect the NMR optically (ODNMR).

Pioneering experimental and theoretical work with gallium arsenide (GaAs) bulk crystals has been carried out in the 1970's and 1980's by A.I. Ekimov, V.I. Safarov, M.I. D'yakonov et al. ([3], [4], [5], [6]); by B.P. Zakharchenya, V.G. Fleisher et al. ([7], [8], [9], [10]); and by D. Paget ([11], [12], [13]). The main aspects of optical pumping of nuclei in GaAs and other semiconductor materials are published in *Optical Orientation*, edited by F. Meier and B.P. Zakharchenya [14].

The combination of the high degree of nuclear polarization and the sensitivity of optical detection makes it possible to investigate systems with only a small number of spins ($N \sim 10^{11}$ or less). The first observation of ODNMR in GaAs/AlGaAs quantum wells has been published by G.P. Flinn et al. [15] [16] and later in heterostructures by M. Schreiner et al. [17] [18] [19] and T. Wimbauer et al. [20]. Various techniques have been demonstrated in either GaAs bulk or GaAs/AlGaAs heterojunctions by S. Buratto, J.A. Marohn, D.P. Weitekamp et al. [21] [22]. Even directly (radio frequency, RF) detected optically pumped NMR has been observed in GaAs quantum wells by S.E.Barrett, R. Tycko et al. [23] utilizing only the high degree of nuclear polarization. However, the direct RF detection method lacks the second high advantage of optical detection of the NMR signal, which imparts the selectivity to the quantum well of interest. Each quantum well absorbs and emits light depending on its width. By selectively exciting and detecting a certain wavelength it is possible to distinguish between quantum wells of different sizes, the AlGaAs barrier, and the GaAs substrate. The incredibly high sensitivity and selectivity of this method has been demonstrated by D. Gammon et al. [24], detecting about $N \sim 10^5$ spins in single quantum dots using ODNMR.

The most recent technique developments have been carried out in the Suter lab and by J.M. Kikkawa, G. Salis, D.D. Awschalom et al. ([25] [26]). These groups use an all-optical method wherein the radio frequency field for NMR is applied by modulation of the intensity or polarization of the exciting laser light.

1.2 Outline

This thesis presents advancements in optically detected nuclear magnetic resonance applied to GaAs/AlGaAs quantum wells of various thicknesses and the application to the investigation of structural problems in nanoscopic systems.

In chapter 2 some basic properties of the sample itself and the sample growths are summarized. The band structure of bulk GaAs and the deviations in a two-dimensional structure are discussed. The resulting optical properties such as absorption and fluorescence are briefly treated and their impact on ODNMR are analyzed.

Chapter 3 gives an overview of the experimental setup and the components involved. Each part and its function is explained in the necessary detail to understand the functionality of the ODNMR spectrometer.

In chapter 4, the main aspects of the electron-nuclear spin coupling are discussed in detail. The main contribution of electrons to the polarization is evaluated which makes it possible to give an approximation for the maximum nuclear fields created by optically pumped nuclei. Measurements of the displaced Hanle curve in different quantum wells reveal the generated nuclear field, and from the calculations it is possible to obtain a value for the degree of nuclear polarization. Field dependent experiments show some new aspects of the coupling of the electron-nuclear spin system.

Chapter 5 presents the observation of optically detected nuclear magnetic resonance in GaAs quantum wells. The nuclear system is pumped in an oblique field, and the ODNMR signal is detected by observing the shift of the displaced

Hanle curve as the nuclear polarization is destroyed under NMR conditions. The optical signal can be fitted, thereby obtaining the underlying NMR spectrum. The experimental data are compared with simulated spectra revealing information about the population distribution of the nuclear system.

In chapter 6, quantum-well dependent ODNMR spectra are presented. The resonance lines are split which is attributed to a quadrupole interaction. The splitting is quantum well-dependent, and a model for explanation of this behaviour is presented. The satellite lines show significant broadening, and possible reasons are discussed and compared with simulations.

Chapter 2

Quantum Well Properties

2.1 Sample Properties

The samples investigated in this thesis are all multi-quantum well structures with gallium arsenide (GaAs) quantum wells and barriers composed of either aluminum gallium arsenide (AlGaAs) or aluminum arsenide (AlAs) short period superlattice (SPS) barriers. They are grown by molecular beam epitaxy (MBE), a well established technique for producing high quality crystal structures. The advantage of MBE compared to other crystal growth techniques, such as metal organic chemical vapor deposition (MOCVD), is the possibility of *in situ* characterization of the growth process.

Each atomic component is provided separately in its own effusion cell which is controlled by a shutter. In this way, the stoichiometric compilation of the final compound can be regulated to a very high degree, and one can grow different materials on a monolayer scale. The substrate (GaAs in the case of the samples covered in this thesis) is spinned and heated during the growth, preventing inhomogeneous distribution of the grown material. It is possible to grow with a rate of about one monolayer/s, and growth interruptions at each interface of several seconds provide for high quality interfaces. In the case of GaAs/AlGaAs heterostructures, it is possible to produce interfaces with hardly any intermixture of aluminum into the GaAs quantum well. In addition, the interface defect density is very low, which is shown by optical characterization of the samples.

The samples are grown by Soheyla Eshlaghi in the laboratory of Andreas D. Wieck of the Department of Applied Physics at University of Bochum. Details of the growth process and conditions, as well of the characterization by photoluminescence spectroscopy performed here, in the Suter laboratory, are published in the Ph.D. thesis of S. Eshlaghi [27].

In particular, three different samples are investigated during this thesis. The main work is carried out at sample with $\#1431$, and some experiments are done with the samples $\#1056$ and $\#1294$ in order to compare results. The principal structure of the multi-quantum well samples is depicted in figure 2.1. As a substrate, a commercial 0.5 mm thick GaAs wafer is used, orientated in the $\langle 001 \rangle$ direction. Whereas all quantum wells are intentionally undoped with an impurity density of less than $10^{11}\,\mathrm{cm}^{-3}$, the substrate is doped with tellurium in sample $\#1431$. Hence, it is semiconducting, which could be used to apply an external field to this particular sample. Initially a GaAs buffer layer or an AlAs/GaAs SPS is grown in order to suppress detrimental effects from surface roughness and lattice defects from the substrate . The detailed structure of the samples is summarized in table 2.1.

The growth order of the quantum wells is such that the widest well is on the bottom, and the smallest well is on the top of the sample. This is a condition that permits optical access to all quantum wells as will be made clear later in the

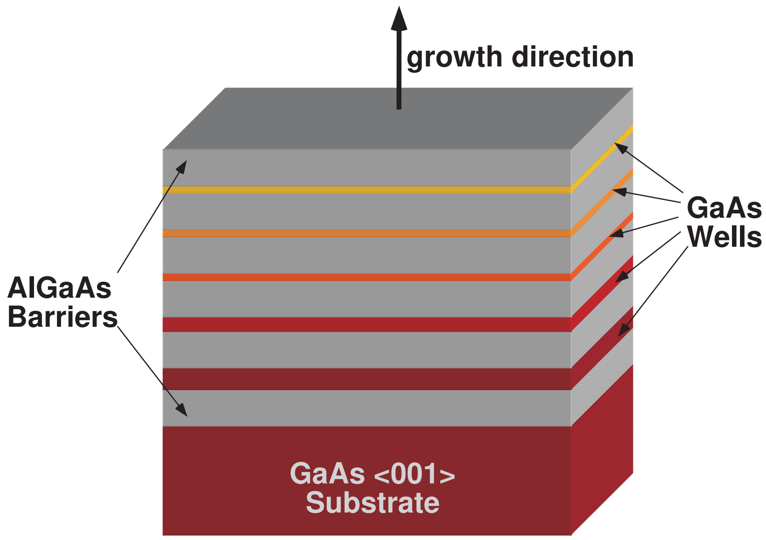

Figure 2.1: Principal schematic of the multi-quantum well samples. The relative dimensions in the picture are not to scale in order to increase readability.

chapter. The samples are grown on one-quarter of the substrate wafer and then cut into pieces of 2 mm by 5 mm. The size of the pieces is chosen to fit onto the sample holder of the ODNMR apparatus between the RF coils.

GaAs and AlAs are considered to be lattice matched; in other words the differences in the lattice constant between the two alloys are very small. The lattice constant of bulk GaAs is $a = 0.5653$ nm and of bulk is AlAs $a = 0.5660$ nm [28]. The properties of ternary compounds such as $\text{Al}_x\text{Ga}_{x-1}\text{As}$ are regulated by variation of the aluminum content, x. The lattice constant of $\text{Al}_x\text{Ga}_{x-1}\text{As}$ can be calculated using Vegard's law [29] [30] [31] (see section 6.4 for details) and increases linearly from GaAs to AlAs as the ratio of gallium to aluminum is varied. The small difference in lattice constant facilitates the growth of heterostructures composed of these alloys and leads to samples which are strain free, to a certain extent. For thin layers grown onto a thick substrate, the underlying lattice cannot be distorted significantly. Therefore, the layer is strained in the growth direction in order to conform to the GaAs lattice positions in the plane of the junction. Thus, the lattice constant of AlAs or AlGaAs in the lateral plane is that of GaAs while the usual elastic response causes it to lengthen along the direction of growth, causing a large amount of elastic energy to build up which in turn has an impact on the GaAs at the interface. Details about the magnitude of the relative strain at the interface of GaAs/AlGaAs and its influence on ODNMR spectra are discussed in chapter 6.

2.2 Optical Properties

2.2.1 Band Structure

GaAs, AlAs and AlGaAs all possess a zinc blende solid state structure. A small part of the band structure near the center of the Brillouin zone of GaAs is shown in figure 2.2. GaAs and AlGaAs with an Al-content of up to about 43% [32] belong to the group of direct bandgap semiconductors with a maximum of the valence band and a minimum of the conduction band at the Γ-point (**k**=**0**). The band gaps of GaAs and $Al_{0.35}Ga_{0.65}As$ are $1.519\,\mathrm{eV}$ and $\sim 1.95\,\mathrm{eV}$, respectively [33]. Due to the bandgap energy difference of both materials, the carriers are confined in the growth direction in the region of lower energy, which is in the GaAs well.

The carriers in the crystal are subjected to the influence of the periodic lattice potential which is taken into account by an effective mass. The masses are different for each carrier type and mirror the curvature of the energy band. Since the degeneracy of the Γ_8 valence bands is removed for $k \neq 0$, the holes have different masses depending on which band they belong to. One distinguishes between light (lh) and heavy (hh) holes. The effective mass for electrons in GaAs is $m_e = 0.0665$, and for the holes are $m_{lh} = 0.094$ and $m_{hh} = 0.34$ [34]. The difference in the band gap is distributed by the shifting of both the conduction and valence bands by a ratio of 65% to 35%, and the potential well in the conduction band is about 0.28 eV high. The GaAs/AlGaAs quantum wells belong to the class of type I semiconductor heterostructures, meaning that the minimum of the conduction band and the maximum of the valence band are both in the well. Hence, the electrons and holes are both situated within the quantum well, which serves as the source of high recombination rates and photoluminescence intensities.

As a first approximation, the electron confined in the conduction band of the quantum well can be treated as a particle in a square potential well with finite potential height, treated in various textbooks. Movement of the electron in the growth direction (z-direction) is suppressed by the confinement that produces simple discrete energy states for the electron, whereas movement in the xy-plane shows the dispersive energy band similar to that of the bulk crystal. The changes going from a bulk solid to a quantum well are schematically depicted in figure 2.2 with the parabolic approximation of the energy band at the Γ point. Note, that the split-off valence band, which is much lower on the energy scale, is not shown in any of the pictures.

The confinement has, in principle, two effects on the electron and hole energy levels. The levels are shifted to higher energy compared to bulk, and the degeneracy is removed at the Γ-point in the valence band due to the different

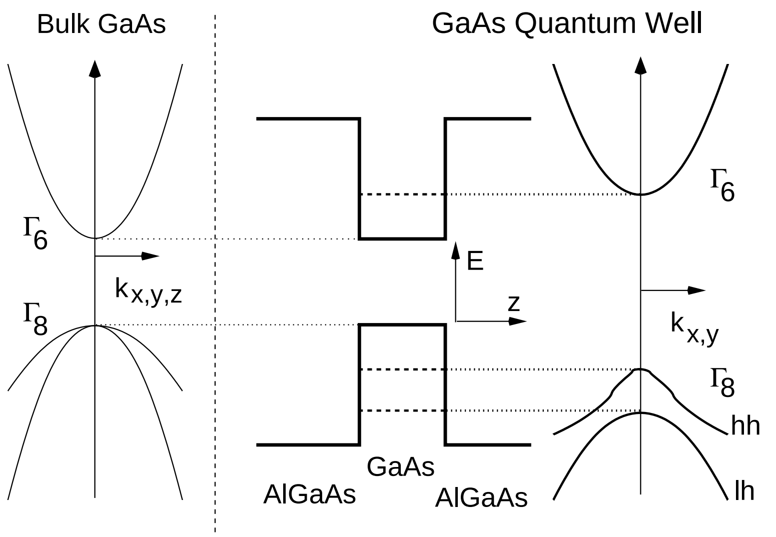

Figure 2.2: The band structure of bulk GaAs and that of a GaAs quantum well near the center of the Brillouin zone. The energy levels become discrete normal to the well, whereas they are still dispersive in the lateral direction. The degeneracy of the light (lh) and heavy hole (hh) is removed in the quantum well in the k_z direction.

effective masses of the two highest valence band levels. The size of the valence band splitting depends on the width of the quantum well according to

$$E_n(L_z) = E_{gap} + \frac{(\hbar\pi n)^2}{2m_0 L_z^2}\left(\frac{1}{m_e} - \frac{1}{m_h}\right) \tag{2.1}$$

where L_z is the width of the quantum well, m_0 the free electron mass, n the order of the energy state, and m_h the effective mass of the light or heavy hole. This equation is valid for an infinitely deep potential well, but it describes the confinement effects here to a sufficient extent. When calculating the energy levels, it easy to see, that a lower effective mass for the light hole creates a bigger splitting than for the heavy hole.

2.2.2 Photoluminescence

Photoluminescence (PL) is an efficient tool for studying electronic properties since its intensity and wavelength are determined by the density of electrons, transition probabilities, and populations of the various states. In principle, three different kinds of photoluminescence are distinguished in semiconductor optics: intrinsic, extrinsic and excitonic. Intrinsic photoluminescence is connected to band-to-band transitions of free electrons and holes. Exciton luminescence is

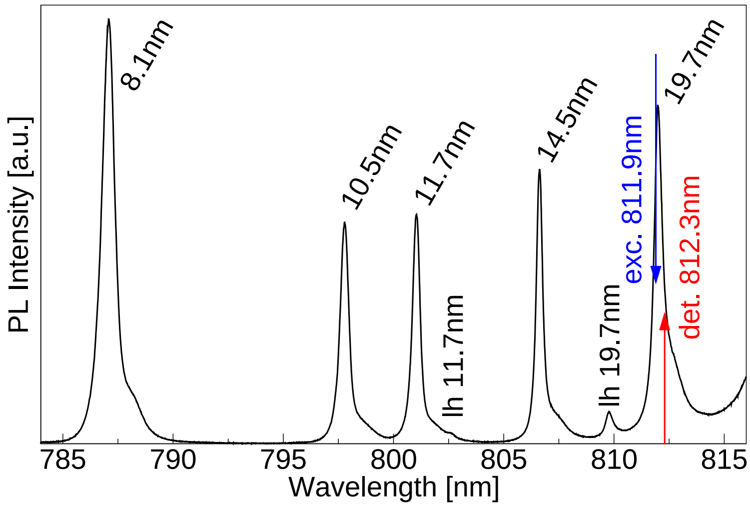

Figure 2.3: Photoluminescence spectrum of a multiple quantum well structure (sample # 1431). Each heavy hole emission line is labeled with the width of the quantum well source. The lines labeled with lh are attributed to light hole transitions, assigned by comparison with PLE spectra. The arrows denote the typical spectral position of the laser and optical spectrometer for resonant excitation and fluorescence detection, respectively, in an ODNMR experiment.

created in the recombination of free, impurity-bound and localized excitons. "Impurity" or extrinsic luminescence originates from the recombination of free electrons with acceptor-bound holes or of electrons bound to donors with free holes.

Excitonic effects occur as a result of the Coulombic interaction of the hole and electron and can cause the position of the quantum well emission line [35] to vary substantially. The transition energy is reduced by the amount of the exciton binding energy. In sharp contrast to bulk GaAs, the dominant contribution to the luminescence in these type I quantum wells is of excitonic origin [36]. The wavelength of the emission depends strongly on the width of the quantum well due to the confinement (see equation 2.1), as observed in a portion of such a fluorescence spectrum from sample $\#1431$ in figure 2.3. The sample is excited into the continuum of the conduction band, and the spectrum is taken by scanning the grating of the monochromator. The emission lines can easily be recognized as the heavy hole transitions of the various quantum wells. Figure 2.3 reveals one of the two main advantages of ODNMR. Each quantum well can be excited separately from the others by tuning the laser to be resonant with the heavy hole transition of the quantum well in question. By setting the optical spectrometer to the transition line of that quantum well, one also spectrally discriminates the signal from the excited quantum well from the rest of the sample.

The energy of the exciton depends on the width of the quantum well; therefore, the width of the emission line is a measure of the quality of the sample. Quantum wells of low quality have defects at the heterostructure interface. Bastard et al. [37] have shown that the in-plane center of mass motion of the exciton creates bound levels due to localization at interface defects of one to two monolayers in height. A distribution of defect islands would therefore significantly broaden the emission line, in some cases from 5 meV to 10 meV [38]. The emission lines in the PL spectra of the different samples are all very narrow but show small differences in broadening. Sample $\#1294$ has very sharp and narrow lines indicating a very high interface quality. According to this argument, sample $\#1056$ has the most interface roughness and therefore the highest exciton localization.

The relaxation of the excitons into the potential minima of the interface defects cause a red shift of the emission line compared to the absorption energy, called the Stokes shift. Measuring the Stokes shift therefore gives insights, as well, to the interface quality. However, absorption measurements are only possible if one removes the substrate from the sample by etching; therefore, photoluminescence excitation (PLE) spectroscopy is used instead. The variation of the intensity of a given luminescence line is measured versus the wavelength of the exciting light source in PLE. The information obtained is equivalent to an absorption spectrum for quantum wells for excitation energies below the continuum. For higher excitations, intra-band transitions are involved which give rise to discrepancies between absorption and PLE spectra. A schematic PLE spectrum is shown on the left of figure 2.4.

As shown in figure 2.4, the excitation of the heavy and light hole transitions occur at different excitation energies. The light holes relax non-radiatively to the top of the valence band, hence the emission takes place for both heavy and light hole excitation in the e-hh transition which is recorded with the optical spectrometer. The PLE spectra from the samples investigated during this work show no resolvable Stokes shift except for the smaller wells of sample $\#1056$. This result validates the conclusions drawn from the PL spectra, with regard to increased interface roughness in the sample. Interface roughness would lead to trapping of excitons and hence to a Stokes shift of the emission line.

By comparison of the energy of the light hole in the PLE spectra with the PL spectrum in figure 2.3, the two low-intensity lines are attributed to light hole transitions.

2.2.3 Optical Pumping

Optical pumping is based on the optical selection rules which apply to both GaAs bulk and quantum wells. The total angular momentum of the valence

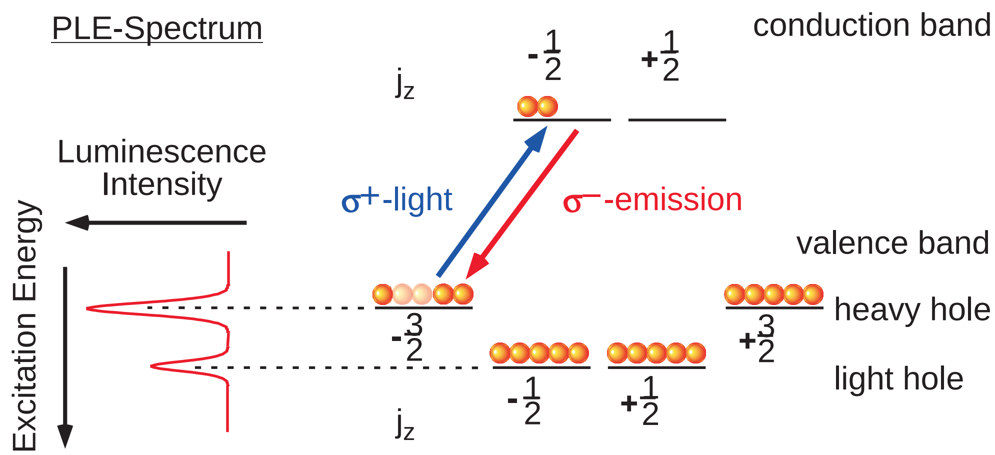

Figure 2.4: PLE spectrum and discrete $n = 1$ energy levels of a GaAs quantum well at $\mathbf{k} = 0$, where the degeneracy of the valence band is removed. Varying the excitation energy of the laser light resonantly excites the hh-e and then the lh-e transition. The emission occurs in both cases for the e-hh transition which is detected with the optical spectrometer. j_z is the projection of the total angular momentum on the quantization axis.

band is $J = 3/2$ corresponding to an atomic p-orbital state. The heavy hole states are $j_z = \pm 3/2$, the light hole states $j_z = \pm 1/2$. The conduction electron is s-type, and the selection rule for inter-band transitions are the same as for transitions between the atomic levels, $^2P_{3/2}$ and $^2S_{1/2}$ [39]. Since the total angular momentum is conserved for absorption of a photon, σ^+ (σ^-) circularly polarized light induces $\Delta m = +1$ ($\Delta m = -1$) inter-band transitions, whereas π linearly polarized light induces $\Delta m = 0$ transitions. Figure 2.5 shows the allowed transitions for the different polarizations of the exciting light. Of course, the same selection rules hold for the recombination, which changes the helicity of the fluorescence compared to the corresponding excitation light as shown in figure 2.4.

Exciting the electron with a circular polarized laser resonant to the heavy hole transition (blue arrow in figure 2.4) populates only one of the two spin states in the conduction band. The polarization of the conduction electron spin system is defined by

$$P_e = \frac{n_+ - n_-}{n_+ + n_-} \tag{2.2}$$

where $n_\pm$ are the populations of spin states $j_z = +1/2$ and $j_z = -1/2$, respectively. It is therefore in principle possible to create an electron spin polarization (P_e) of 100 % in the quantum well. This is indeed twice as big as in the bulk case, where due to the degeneracy of the valence band, both the heavy hole and

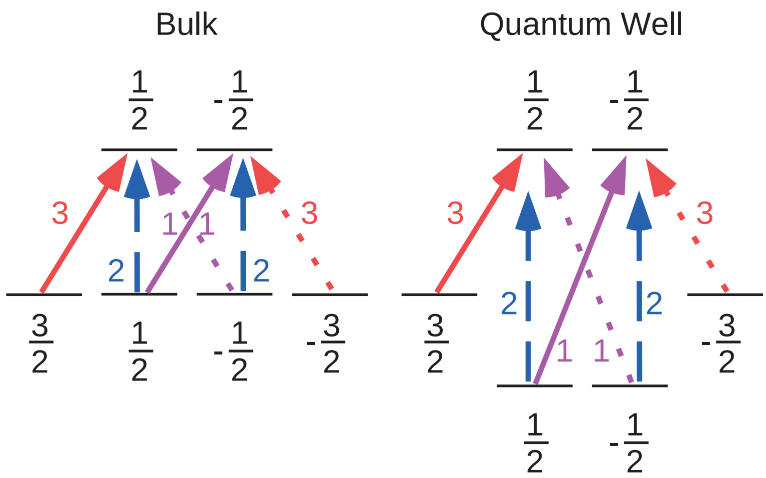

Figure 2.5: Relative transition probabilities in GaAs for different excitation polarization. Solid line: σ^+, dotted line σ^-, dashed line: π. The numbers close to the energy levels denote the projection of the total angular momentum on the quantization axis.

the light transitions are excited. A polarization in the bulk case is only created due to the different transition probabilities of the heavy and light hole transitions as shown in figure 2.5, and therefore has a maximum value of 50%.

The polarization of the emission light is in the case of the quantum well 100%; the polarization of the photoluminescence is therefore a direct measure of the electron spin polarization. In contrast for bulk GaAs the photoluminescence polarization is due to the transition probabilities, which has a maximum of 25% in maximum. These represent only theoretical values for polarization which are modified by spin-lattice relaxation, discussed in greater detail in chapter 4.

sample id	#1056	#1294	#1431
buffer composition	GaAs buffer $Al_{0.31}Ga_{0.69}As$/GaAs SPS GaAs buffer =520 nm	GaAs buffer AlAs/GaAs SPS =278.2 nm	AlAs/GaAs SPS =78 nm
barrier type	$Al_{0.35}Ga_{0.65}As$ =26.2 nm	AlAs/GaAs/AlAs SPS =31.6 nm	$Al_{0.35}Ga_{0.65}As$ =30.9 nm
quantum well widths	19.4 nm 14.9 nm 11.8 nm 9.8 nm 7.8 nm 5.9 nm	19.8 nm 15.2 nm 12.2 nm 9.9 nm 8.3 nm 7.1 nm 6.3 nm 5.6 nm 5.1 nm 4.5 nm 4.0 nm 3.3 nm	39.3 nm 19.7 nm 14.5 nm 11.7 nm 10.5 nm 8.1 nm 6.8 nm 5.8 nm 5.1 nm 4.3 nm 3.9 nm 3.4 nm 2.8 nm
cladding	12 nm	2.9 nm	13.4 nm

Table 2.1: Thickness of various quantum wells for the different samples. The first row denotes the number of the sample, the second shows the structure of the buffer layer with its total thickness. Then the type of barrier with its thickness is given, and the fourth row summarizes the width of the various GaAs quantum wells. The last row gives the thickness of the cladding GaAs layer on top of the sample.

Chapter 3

The ODNMR Spectrometer

3.1 Introduction

The experiments for this project were performed primarily with the same apparatus. The spectrometer used for optically detected nuclear magnetic resonance was designed and built in the Suter laboratory at the University of Dortmund. The system includes the optics and lasers for optical excitation, the magnet and cryostat holding the sample, and the optics and monochromator for optical detection of the signal. An overall picture of the setup is illustrated in figure 3.1, and it will be discussed in section 3.2. The remaining sections of this chapter will treat the different components in detail.

3.2 Experimental Setup

As a laser source for this project, different diode laser systems were used which will be discussed in section 3.3. Since diode lasers are very sensitive to back-reflected light from surfaces of other optical components in the setup, special care was taken to reduce this detrimental effect with an optical isolator. As shown in figure 3.1, the beam from the laser system is steered with mirrors M1 and M2 through an optical isolator (OI), which attenuates the reflected light by 40dB. The mirrors M1 and M2 are replaceable mirrors on a kinematic mount. The top plate of the mount can be removed and replaced automatically to an exact location. A set of mirrors belongs to each laser (i.e., LD1, LD2, LD3), hence the mirrors have to be adjusted only once, and lasers can be switched very easily during the experiment. For fine tuning, the alignment of the laser beam is steered with the mirrors M1 and M2 through two irises, I1 and I2.

After passing the isolator, the beam is split with a polarizing beam splitter (PBS). One part is used for analyzing the beam with a wavemeter, and the other beam with the most intensity goes to the experiment. The wavemeter from NewFocus has an accuracy of 0.01 Å, and the vacuum wavelength is measured. The $\lambda/2$-plate (LHP1) is needed to rotate the polarization of the laser beam and therefore makes it feasible to change the intensities of the splitted beams. The linearly polarized beam is directed with the mirror (M3) through the lens (L1) onto the sample. The focal length of lens L1 is 300 mm and focuses the laser beam down to a minimum of 50 μm in diameter. Using a quarter wave plate (QWP) creates either left-hand or right-hand circularly polarized light, depending on the angle of the E-field vector with the main axis of the quarter wave plate. The orientation of the fast and the slow axis of the quarter wave plate cannot be changed and are parallel and perpendicular to the laser table, respectively. To rotate the polarization of the laser beam to either 45° or -45° with respect to one of the QWP axes, a second $\lambda/2$-plate (LHP2) is placed in front of mirror M3.

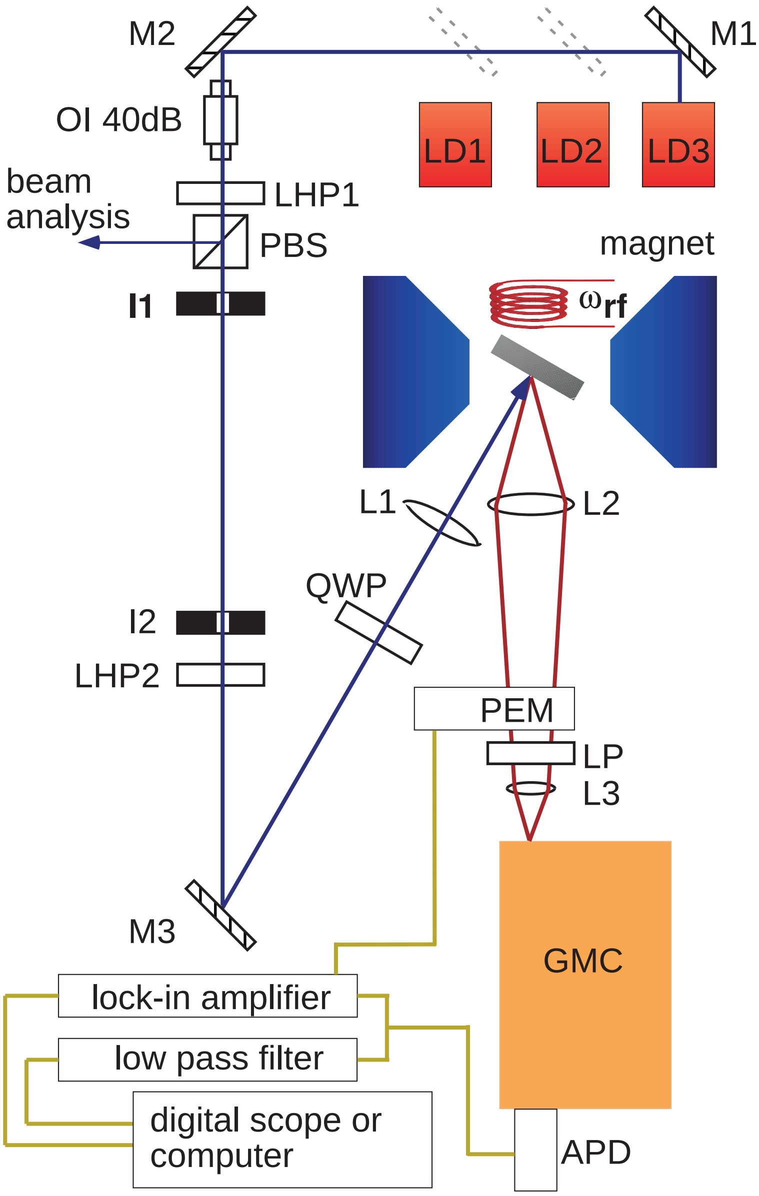

Figure 3.1: The geometry of the experimental setup. The mirrors in front of LD1 and LD2 are easily replaceable in order to change the wavelength of the laser system. The radio frequency is applied perpendicular to the plane of the diagram. The photoluminescence is detected with the grating monochromator (GMC) and the avalanche photodiode (APD).

In this configuration the sample will be illuminated by a fixed type of polarization which will create nuclear polarization in the presence of an external field.

The sample is placed into a cold-finger cryostat with the surface perpendicular to the incoming laser beam. A B_0-field is created with an electromagnet at an angle of 74° with respect to the excitation light. The photoluminescence is emitted backward by the sample, picked up with a large (48 mm clear aperture) collimating lens (L2), and focused with lens L3 into the spectrometer. The focal lengths and positions of the lenses are chosen to maximize the collected luminescence light and to properly illuminate the first spectrometer mirror. The optical detection system magnifies the picture of the sample by a factor of 1.3. Lens L2 is placed on three positioning stages with micrometer screws. This setup allows for highly accurate and reproducible alignment of the collimating lens. If the sample is not removed from the cryostat, the position on the sample being investigated in an experimental run can easily be identified with the aid of the micrometer screws over several days. For analyzing the degree of luminescence polarization, a photo elastic modulator (PEM) and a linear polarizer (LP) are placed in front of lens L3.

For experiments in which it is necessary to prevent the nuclear system from polarizing (for example, Hanle measurements) the PEM is placed into the excitation path taking the place of the quarter wave plate. The helicity of the circular polarization is modulated with the PEM frequency (50 kHz), hence the polarization of the electron system is reversed within a time which is very short compared to the optical pumping time constant. Therefore, the coupling of the electron and nuclear systems is suppressed. Since the polarization of the luminescence is now modulated in this setup, the quarter wave plate is placed into the detection path in front of the linear polarizer in order to analyze the degree of polarization.

3.3 Laser

Several diode lasers are used to provide the requisite optical radiation to excite electrons in the different quantum wells. The laser excitation system consists of non stabilized (free running) diode lasers, a tunable external cavity laser with a Littrow configuration, and a second tunable external cavity laser with a Littman configuration.

The free running diodes are placed in a homemade vacuum chamber and are actively cooled with a peltier element. This construction provides the ability to tune the wavelength of the laser over a range of up to 3 nm by varying the temperature of the diode from about 40° C to -10° C. The output power typically lies between 80 mW and 100 mW. The wavelength stability of these diode lasers depends on the current and temperature control; therefore, a controller for the laser system was developed which met the desired specifications for the beam stability required.

Tuning the free running diode lasers is limited, and specific wavelengths might not be reachable due to mode hops of the laser. Therefore, a laser system from TUI-Optics (now Toptica Photonics) is used with an external cavity in a Littrow configuration. The laser light is diffracted at an optical grating, and the first order diffraction beam is directed back into the laser thereby creating the external cavity. Wavelength selection is achieved by turning the grating; the system has a tuning range of about ± 4 nm. The output power is reduced by about 50 % compared to the free running diode lasers, but it is still sufficient for optical pumping. An automatic scan of the wavelength cannot be implemented because the angle of the emerging beam depends on the wavelength and changes during a scan, requiring realignment of the optics.

To accommodate automatic tuning of the laser wavelength in order to take, for example, a photoluminescence excitation (PLE) trace, a system from EOSI (Newport) is used. This system has a Littman configuration with a grating and a retroreflection mirror. The angle of the emerging beam is wavelength independent and therefore does not move during the scan. A tunable wavelength range of up to ± 10 nm can be achieved with an output power of about 10 mW to 15 mW. The entire system including these various lasers covers a wavelength range from 776 nm to 820 nm. However, a gap in the spectral range of the system at 787 nm impedes the investigation of the 8.1 nm wide quantum well.

3.4 Detection of Polarization

For optical detection of the nuclear magnetic resonance, the degree of the photoluminescence polarization is observed. The timescale for measuring changes in the polarization must be fast with respect to the physical processes occurring during the experiment; in other words, the detection must be faster than the passage through the resonance. The analysis of the circular polarization is greatly aided by using the combination of a Hinds Instruments model PEM-90 photo elastic modulator and a linear polarizer oriented at an angle of $45°$ to the PEM's axis (see figure 3.1, components PEM and LP). The PEM contains an isotropic optical element (glass) connected to a piezoelectrical crystal. With a tuned circuit, the piezoelectric crystal is excited to periodic oscillations at 50 kHz and induces uniaxial strain into the glass, such that it becomes birefringent. Therefore, the polarization components of the transmitted light are affected differently by the two axes of the PEM. The path length of the component of the light parallel to the strained axis is modulated, and the maximum path length difference between the strained and the unstrained axes can be arbitrarily chosen. In the case of

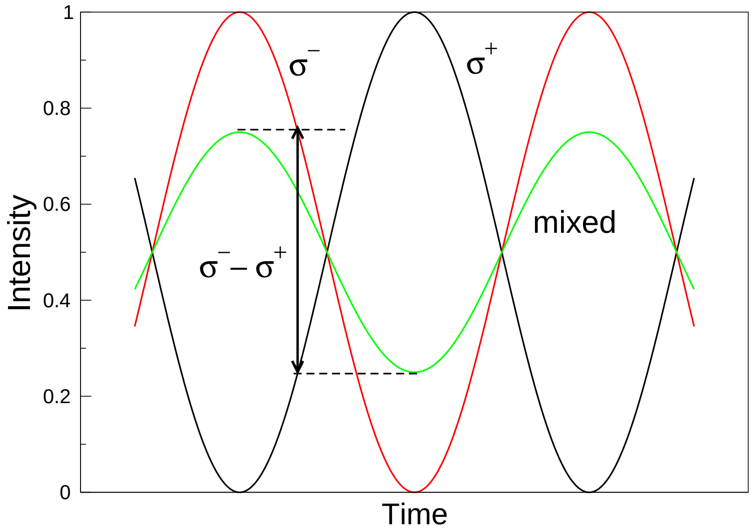

Figure 3.2: The transmission function of the combination of a PEM with a linear polarizer. In case of purely right- or left-hand polarized light, the transmission is modulated between zero and 1. For mixed polarizations, the transmission does not reach the extreme values. The lock-in amplifier measures the difference between the extrema.

analyzing circular polarization emitted from the sample, it is set to one-quarter of the wavelength. With the PEM only the changes of the nuclear polarization can be detected; the precession frequency of the nuclear spin is higher than the bandwidth of the optical detection system and therefore cannot be observed.

The signal that is measured, after the combination of a PEM and a linear polarizer, depends on the polarization of the incoming light. The principle of measuring the polarization is explained by Jasperson and Schnatterly [40]. The laser excites the sample with either left-hand (LHCP) or right-hand circularly polarized (RHCP) light. If there are no losses in the sample, the emitted photoluminescence is also circularly polarized. In one extreme of the oscillation (of the strained glass), LHCP light passing the PEM is transformed into one of the linearly polarized components. In the other extreme, it is transformed into the orthogonal linear component. In between, the light is elliptically polarized. With the linear polarizer after the PEM, only one component of the linear polarization is selected, thus converting the polarization modulation into an intensity modulation with a frequency of 50 kHz. For example, in case of LHCP light, the relative intensity can be modulated between 0 and 1. The signal is depicted in figure 3.2. The signal for RHCP light is phase shifted by $180°$ relative to the LHCP signal. In the usual case of mixed circular polarization emitted from the sample, light will pass the polarizer in both extrema of the PEM modulation.

The minimum of the modulated intensity does not reach zero in this case. If I_+ is the intensity for RHCP light and I_- for LHCP light, the difference between the maximum and the minimum of the signal is proportional to the difference $(I_+ - I_-)$ of the amount of LHCP and RHCP light passing the PEM. Normalized to the total intensity $(I_+ + I_-)$ light passing the PEM reveals the relative degree of polarization emitted from the sample.

The difference signal $(I_+ - I_-)$ is detected with a Stanford Research lockin amplifier referenced to the frequency of the PEM. A lowpass filter from Stanford Research works as an integrator and measures the total intensity $(I_+ + I_-)$ passing the PEM. The division of both signals is carried out by the lockin amplifier. In order to reveal an absolute value for the degree of circular polarization, the polarization of the scattered laser light is detected, and the photoluminescence polarization is normalized to this value.

3.5 Optical Spectrometer

The signal is detected with a spectrometer consisting of a Spex 1704 monochromator and an avalanche photodiode Module C5460-01 from Hamamatsu. The 1 m focal length monochromator is equipped with variable input and output slits and a motor drive for turning the diffraction grating. The maximum resolution is 0.061 Å at a slit width of 8.03 μm. During the NMR experiments the slits were usually 100 μm to 200 μm wide in order to increase the signal intensity, which reduces the resolution to 0.075 nm and 0.15 nm, respectively.

The avalanche photodiode module (APD) is equipped with the diode and a low-noise current-to-voltage amplifier circuit, and it is attached to the output slit of the monochromator. The spectral sensitivity of the APD has its maximum of 0.5 A/W in the region of interest at about 800 nm. The current is transformed to a voltage with a $10\,\Omega$ resistor and amplified by a factor of 30. The cut-off frequency is 100 kHz, sufficiently high to operate as a detector for modulated signals at 50 kHz. The noise equilvalent power (NEP) is 0.02 pW/$\sqrt{\text{Hz}}$. The bandwith of the lock-in amplifier is about 500 Hz giving a NEP of 0.44 pW.

3.6 Optical Cryostat

All experiments for this project are carried out below liquid helium temperatures. To cool the sample, it is mounted on the sample holder and placed into the vacuum chamber of a home-built stainless steel flow cryostat. The vacuum space is maintained at a pressure of approximately 10^{-6} mbar by continuous pumping with a Pfeiffer turbo molecular pump. The sample is glued with silver thermal epoxy to the copper sample holder which itself is glued to the cold finger of the cryostat. This method provides the best thermal contact and a maximum of flexibility to exchange the sample and the sample holder. Helium is transferred from an external reservoir into the cryostat, and the inner part of the cold finger is cooled by the liquid helium. Pumping on the helium level reduces the vaporization temperature, and temperatures down to 2.5 K (measured on the surface of the cold finger) are reached. Despite the good thermal contact, the sample is only at a temperature of about 3.5 K. The temperature is measured at the cold finger and at the terminal end of the sample holder with magnetic field-independent GaAs diodes (TG-120 CU from Lakeshore). Heating wire attached to the cold finger provides the ability to set the temperature to values above 2.5 K. The temperature sensors and the heating wire are controlled by a Oxford ITC 502 temperature controller.

For optical access to the sample, the cryostat is equipped with a window perpendicular to the direction of the external field. Since the sample is in vacuum, detrimental effects due to helium gas or bubbles of boiling helium are not of any concern.

3.7 External B_0 Field

The cryostat is placed between the poles of a Bruker electromagnet. The magnet's field can be arbitrarily set up to a maximum of about 1.4 T. With the aid of two shimming coils, a field antiparallel to the electromagnet's field can be created, extending the range below 0 T to -11 mT. The power supply of the magnet is controlled with a digital-to-analog converter (DAC) and the computer. The resolution of the DAC is 20 bit, but the stability of the power supply is not sufficient to permit measurements of chemical or Knight shifts. The size of the magnetic field is measured with a Hall probe outside of the cryostat and a Hameg HM 8112-2 voltmeter. The field can be measured with an accuracy of 0.01 mT, but the absolute value at the position of the sample cannot be obtained because of the inhomogenity of the field.

3.8 Radio Frequency Field

The sample, mounted on the copper sample holder, is placed between two RF coils in a Helmoltz configuration as depicted in figure 3.3. This setup allows optical access to the sample and minimizes photoluminescence losses. Each coil contains 40 turns wound around a cylinder made out of Teflon. The RF circuit is not matched with tuning components, resulting in reflected power of about

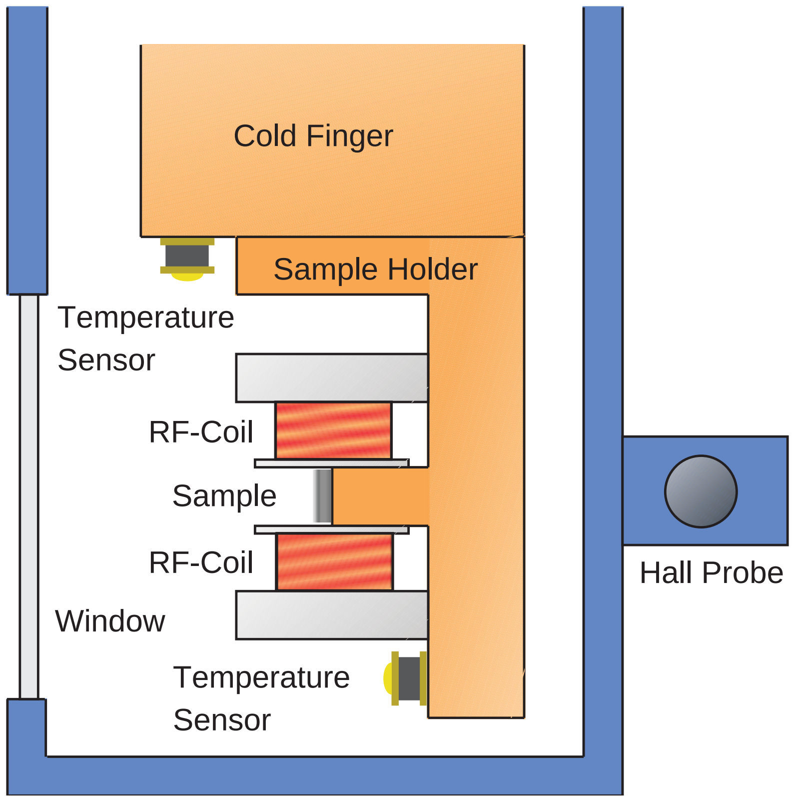

Figure 3.3: Sketch of the sample holder and the RF supply to the sample inside the cryostat (blue). The external field is perpendicular to the plane of the diagram. The room temperature Hall probe is positioned outside of the cryostat.

90% measured with directional couplers. Nevertheless, the RF field produced with this simple circuit is sufficiently high for the ODNMR experiments and can be used over the entire frequency range of interest, which is from DC to about 20 MHz.

A Hameg HM 8131-2 function generator and a Hameg 8133-2 synthesizer are used as the primary RF sources. The maximum amplitude of the RF created by the function generator is 7 V_{rms}, and no amplifier is needed. It is equipped with an IEEE-488(GPIB) interface for computer control and is used for a single rf-scan ODNMR experiment. The synthesizer is used for rapid scanning in frequency modulation mode, for example, in the adiabatic fast passage experiment. The synthesizer's amplitude is limited to 500 mV_{rms}, and an ENI 350L amplifier must be used in conjunction with the synthesizer to create sufficient RF power.

The RF power is measured indirectly by observing the time dependence of the nuclear spin polarization after switching on the RF modulation. For a spin $I = 3/2$ system with resolved quadrupolar splitting, the nuclear spin polarization decays as [41]

$$I_z(t) = I_{z\omega_{q_-}} e^{-2W_{\omega_{q_-}} t} + I_{z\omega_0} e^{-2W_{\omega_0} t} + I_{z\omega_{q_+}} e^{-2W_{\omega_{q_+}} t} \tag{3.1}$$

where the indices $(q_-, 0, q_+)$ refer to the three transitions $(+\frac{3}{2} \leftrightarrow +\frac{1}{2}, +\frac{1}{2} \leftrightarrow -\frac{1}{2}, -\frac{1}{2} \leftrightarrow -\frac{3}{2})$. The radio frequency saturation can be treated as a time dependent perturbation, and the transition probability between state m and $m-1$ is given by

$$W_{m,m-1} = \frac{2\pi}{\hbar^2} |\langle m| \mathcal{H}_{int} |m-1\rangle|^2 f(\omega) \tag{3.2}$$

where $f(\omega)$ is the spectral density function and $\mathcal{H}_{int}$ the interaction Hamiltonian. For calculating the transition probability between different states, the Hamiltonian in the rotating frame approximation can be written as

$$\mathcal{H}_{int} = \frac{1}{2}\hbar\omega_1 I_\pm. \tag{3.3}$$

$B_1 = \gamma_n \omega_1$ is the amplitude of the rotating field coupling to the spins $I_\pm$. According to equations 3.2 and 3.3, the transition probabilities in equation 3.1 become

$$W_{\omega_{q-}} = \frac{3}{2}\pi\omega_1^2 f(\omega_0 - \omega_q) \tag{3.4}$$

$$W_{\omega_0} = 2\pi\omega_1^2 f(\omega_0) \tag{3.5}$$

$$W_{\omega_{q+}} = \frac{3}{2}\pi\omega_1^2 f(\omega_0 + \omega_q) \tag{3.6}$$

with $f(\omega)$ being the spectral density function of the relevant transitions and ω_q the quadrupole splitting.

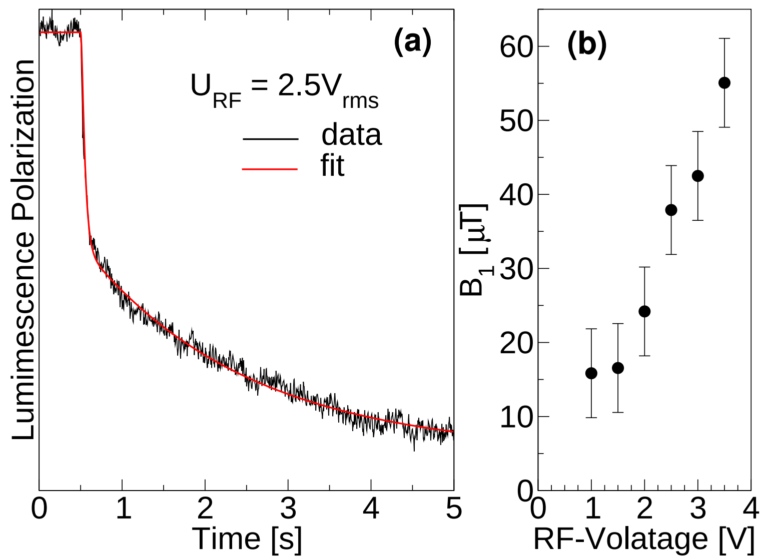

Figure 3.4: (a)Time evolution of polarization during resonant saturation of central quadrupole transition of ^{75}As. See text for details about the fit. (b)B_1 field obtained by the fit depending on the radio frequency voltage applied to the sample.

Figure 3.4(a) shows an example of the time evolution of the polarization. It is obvious that there is more than one decay process occurring, attributable to the central transition (fast decay) and the satellite transitions (slow decay). The red line in figure 3.4(a) is a fit using equation 3.1. The photoluminescence polarization depends on the nuclear field that is proportional to I_z as will be pointed out in chapter 4. Utilizing equations 4.12, 4.40 and 3.1, simulation of the detected optical signal is possible, giving a value for the radio frequency field, B_1.

The radio frequency absorption is measured for different RF-powers applied to the circuit. The B_1-values obtained by the fit are presented in figure 3.4(b). B_1 shows a linear dependence on the rf-voltage supplied by the function generator, as expected. The uncertainty of the fit stems from the inexact determination of the different fit parameters. However, the fit is reliable enough to give a good approximation of the radio frequency field applied to the sample.

3.9 Data Acquisition and Evaluation

Most parts of the experimental apparatus are controlled with a computer, especially the monochromator, the external field, and the EOSI laser. Data acquisition is done with the computer which is equipped with an IEEE-488(GPIB) interface and an analog-to-digital converter (ADC). In the case of NMR experiments, the timing is too critical for the data acquisition with the computer, and a LeCroy 9310A 400 MHz digital oscilloscope is used instead. The synchronization of the experiments is done with the computer for single RF scans or with a Stanford Research Systems DG 535 pulse generator for adiabatic fast passage experiments.

All data is evaluated with software developed in-house. For fitting the theoretical functions to the data, the Levenberg-Marquardt algorithm is used.

Chapter 4

Coupling of Electron and Nuclear Spin Systems

4.1 Optical Pumping

Optical pumping of the nuclear spin system is based on a transfer of the polarization from the orientated electron spin system to the nuclei. The spin polarized electrons in the conduction band are coupled to the nuclei by hyperfine interaction. For electrons in the conduction band described by s-type wavefunctions the Fermi contact hyperfine interaction prevails, given by this Hamiltonian:

$$\mathcal{H}_{hf} = -a_{N\alpha}(\mathbf{r}_i)\hat{I} \cdot \hat{S} \tag{4.1}$$

with the coupling constant

$$a_{N\alpha}(\mathbf{r}_i) = \frac{2}{3}\hbar g_0 \mu_0 \mu_B \gamma_\alpha \left|\Psi_q(\mathbf{r}_i)\right|^2 \tag{4.2}$$

where g_0 is the free electron g-factor, μ_0 the permeability of free space, μ_B the Bohr magneton, γ_α the nuclear gyromagnetic ratio, and $|\Psi_q(\mathbf{r}_i)|^2$ the probability of finding the electron at the location, $\mathbf{r}_i$, of the nucleus. The interaction of the nuclei with the p-orbital symmetry holes in the valence band is of a dipole-dipole type [42] and therefore considerably weaker.

For a nucleus, i, at position, $\mathbf{r}_i$, the hyperfine interaction is equivalent to a Zeeman interaction in a magnetic field of electronic origin [11]:

$$\hat{B}_e^i = -\frac{2}{3} g_0 \mu_0 \mu_B \sum_q \hat{S}_q \left|\Psi_q(\mathbf{r}_i)\right|^2 \tag{4.3}$$

In the same way, a conduction electron in an orbital state, ψ_q, and an effective g-factor, $g^\star$, feels a nuclear magnetic field [11]:

$$\hat{B}_n^q = -\frac{2}{3}\hbar \frac{g_0}{g^\star} \sum_i \gamma_i \hat{I}_i \left|\Psi_q(\mathbf{r}_i)\right|^2 \tag{4.4}$$

The magnetic fields in equations 4.3 and 4.4 between the electron and nucleus have several consequences in magnetic resonance; they are responsible for: the Knight shift of nuclear resonance lines, the Overhauser shift in conduction electron resonance experiments, and dynamic polarization (also known as the Overhauser effect [1]).

4.1.1 The Coupling Constant

In order to calculate the coupling constant, $a_{N\alpha}(\mathbf{r}_i)$, one has to find an expression for the wavefunction, $\Psi_q(\mathbf{r}_i)$. Electrons near the bottom of the conduction band are usually described as a product of an envelope function, $F_q(\mathbf{r})$, of the q-th electron and a rapidly varying periodic function, $u_0'(\mathbf{r})$ [43]:

$$\Psi_q(\mathbf{r}) = F_q(\mathbf{r})u_0'(\mathbf{r}) = F_q(\mathbf{r})u_0(\mathbf{r})\sqrt{\frac{V}{\Omega}} \tag{4.5}$$

where $u_0(\mathbf{r})$ is the $\mathbf{k} = 0$ Bloch function, V the volume of the sample, and Ω the volume of the primitive unit cell. The values for the electronic density, $d_\alpha = |u_0'(\mathbf{r}_\alpha)|^2$, have been calculated by Paget et al. [11]

$$\begin{aligned} d_{^{75}\mathrm{As}} &\backsimeq 9.8 \times 10^{31}\,\mathrm{m}^{-3} \\ d_{^{69}\mathrm{Ga}} = d_{^{71}\mathrm{Ga}} &\backsimeq 5.8 \times 10^{31}\,\mathrm{m}^{-3} \end{aligned} \tag{4.6}$$

For delocalized electrons at the bottom of the conduction band, the value of $F_q(\mathbf{r})$ is $\sqrt{\Omega/V}$ inside the crystal and zero outside. Therefore, the coupling of delocalized electrons can be neglected. The quantum wells contain almost no impurity centers which means that electrons are not bound to any donor states. Instead, they usually form an exciton, which is a coupled electron hole pair, attracted to each other through Coulomb interaction. The wavefunction for the exciton in a quantum well has been derived by Grundmann and Bimberg [44] and by Bastard et al. [37] [45]. It is a product of the electron wavefunction, $\Psi_e(z_e)$, the hole wavefunction in the potential well, $\Psi_h(z_h)$, and an envelope function, $\Phi_{ex}(\rho)$, describing the extension of the exciton in the plane of the well:

$$\Psi_{ex}(z, \rho) = \Psi_e(z_e)\Psi_h(z_h)\Phi_{ex}(\rho) \tag{4.7}$$

where z is the coordinate in the growth direction of the quantum well and ρ the distance from the center of the exciton in the xy-plane. Since the wavefunction of the hole has p-orbital symmetry, the interaction of the hole with the nuclei is much weaker compared to that with the electron and will therefore be neglected. The envelope wavefunction of the electron in a potential well is given by:

$$\begin{aligned} F(z, \rho) &= \tfrac{1}{\sqrt{\Omega}}\cos(kz)e^{-\rho/a_B^\star} && \text{for} \quad |z| < L_z/2 \\ F(z, \rho) &= \tfrac{A}{\sqrt{\Omega}}e^{-\kappa z}e^{-\rho/a_B^\star} && \text{for} \quad |z| \geqslant L_z/2 \end{aligned} \tag{4.8}$$

where k and κ are the wave vectors in the quantum well and the barrier, respectively; L_z is the width of the quantum well; and A, a normalizing factor to meet the continuity conditions at the interface between the quantum well and the barrier. The effective Bohr radius, $a_B^\star$, of the exciton in the xy-plane of the quantum well is proportional to the square root of the width, L_z [44]. $a_B^\star$ can be calculated from the data in [44] assuming that it has the 3D-value for the 20 nm quantum well, $a_B^{3\mathrm{D}} = 16$ nm [46]. The values of the Bohr radii for different quantum wells are listed in table 4.1.

L_z [nm]	$a_B^\star$ [nm]	$F^2(0) \cdot 10^{-5}$	$a_N(^{75}\mathsf{As})/h$	$a_N(^{71}\mathsf{Ga})/h$	$a_N(^{69}\mathsf{Ga})/h$
20	16	1.01	0.112	0.118	0.093
15	14	1.7	0.189	0.199	0.157
10	11	3.9	0.433	0.456	0.359
5	8	12.7	1.410	1.486	1.170

Table 4.1: Effective Bohr radii and hyperfine coupling constants calculated for different well widths. The hyperfine constant is specified in units of MHz. The gyromagnetic ratios used in equation 4.10 are $\gamma_{^{75}\mathsf{As}} = 45.82 \cdot 10^6$ rad(sT)$^{-1}$, $\gamma_{^{71}\mathsf{Ga}} = 81.58 \cdot 10^6$ rad(sT)$^{-1}$ and $\gamma_{^{69}\mathsf{Ga}} = 64.21 \cdot 10^6$ rad(sT)$^{-1}$.

The envelope function is normalized to the volume of the primitive unit cell

$$\int_{-\infty}^{\infty} |F(z,\rho)|^2 d^3 r = \Omega \tag{4.9}$$

where $\Omega = \frac{1}{4} a_l^3$ [47]. The lattice constant of GaAs is $a_l = 0.565$ nm [28], and therefore $\Omega = 0.045$ nm^3. The depth of the potential well is 1.071 eV [28], and the gap between valence and conduction band is 1.52 eV. After normalization of the electron wavefunction one can rewrite $\Psi_q(\mathbf{r}_i) = F(0)\psi_q(\mathbf{r}_i)$, and the hyperfine coupling is

$$\begin{aligned} a_{N\alpha}(\mathbf{r}_i) &= a_{N\alpha} |\psi_q(\mathbf{r}_i)|^2 \\ a_{N\alpha} &= \tfrac{2}{3} \hbar g_0 \mu_0 \mu_B \gamma_\alpha d_\alpha F^2(0) \end{aligned} \tag{4.10}$$

The values of $F^2(0)$ for different quantum well widths are listed in table 4.1. The coupling constant has been calculated for the three isotopes and for different quantum well widths. The values are also listed in table 4.1. The strength of the coupling in the wide wells is comparable with the coupling in doped bulk GaAs crystals [11] but is an order of magnitude bigger in the small wells.

4.1.2 Nuclear Magnetic Field

The nuclear field felt by the electrons consists of the fields created by each nucleus summed over all nuclei that couple to the electron during its lifetime. As described by equation 4.4, the maximum nuclear magnetic field can be calculated with the aid of the wavefunction from section 4.1.1 and the assumption of a homogeneously polarized nuclear spin system. In this case, $\hat{I}_i$ can be replaced by its average value $\left\langle \hat{I}_z \right\rangle$ which is independent of the position of the nucleus. Hence, there is no difference between the field "seen" by an exciton diffusing in the xy-plane of a homogeneously polarized quantum well or a trapped exciton, and the field is calculated for the latter case.

L_z [nm]	u [nm]	v [nm]	s [nm]	$V_{\mathrm{qw}}^{\mathrm{eff}}$ [nm^3]	$V_{\mathrm{bar}}^{\mathrm{eff}}$ [nm^3]	$\mathrm{N}_{\mathrm{UC}}^{\mathrm{qw}}$	$\mathrm{N}_{\mathrm{UC}}^{\mathrm{bar}}$
20	11.1	11.3	0.006	4453	2.3	24740	13
15	8.6	9.9	0.010	2648	2.9	14710	16
10	6.0	7.8	0.019	1147	3.6	6370	20
5	3.4	5.7	0.053	347	5.4	1930	30

Table 4.2: discussed in the text for different well widths. u is the effective height in growth direction, and v the effective radius of the exciton in the xy-plane. $V_{\mathrm{qw}}^{\mathrm{eff}}$ and $V_{\mathrm{bar}}^{\mathrm{eff}}$ are the effective volumes of the exciton in the quantum well and the barrier, respectively. $\mathrm{N}_{\mathrm{UC}}^{\mathrm{qw}}$ and $\mathrm{N}_{\mathrm{UC}}^{\mathrm{bar}}$ are the numbers of unit cells in the quantum well or barrier volume.

Suppose the electron is trapped at a position, $\mathbf{r} = \mathbf{0}$. The interaction probability of each nucleus is given by equation 4.10. One has to calculate the coupling constant of each nucleus at a distance, $\mathbf{r} = \mathbf{r}_i$, and sum over all nuclei in the sample (which is cumbersome). Instead, the exciton can be modeled as a cylinder with its circular base of radius, v, in the xy-plane of the well and height, $h = u + s$, in growth direction. u is the height of the associated cylinder in the quantum well, and s the height of the cylinder part in the barrier. The sum over all nuclei in equation 4.4 can be replaced by an integral over the whole sample. The coupling strength of each nucleus within the cylinder is $a_{N\alpha}$ and zero outside. The probabilities for the interaction have to hold for the following conditions:

$$
\begin{aligned}
\int_{-L_z/2}^{L_z/2} \cos^2(kz)dz &= u && \text{z-direction in quantum well, } |\Psi_e|^2 \\
\int_0^{2\pi}\int_0^{\infty} \rho e^{-2\rho/a_B^{\star}} d\rho\, d\varphi &= \pi v^2 && \text{xy-plane in quantum well and barrier, } |\Phi_{ex}|^2 \\
2\int_{L_z/2}^{\infty} A e^{2\kappa z} dz &= s && \text{z-direction in barrier, } |\Psi_e|^2
\end{aligned}
\tag{4.11}
$$

The values for u ,v and s and the resulting volumes, V^{eff}, of the cylinder in the quantum well and the barrier have been calculated and are summarized in table 4.2.

A comparison of the effective volumes of the quantum well and the barrier shows that the influence of nuclei in the barrier can be neglected in most cases. Even in the 5 nm well, the fraction of nuclei in the barrier is only 1.5 % of the total amount of the nuclei. Therefore, no signal of ^{27}Al situated in the barrier should appear in NMR experiments.

$\mathrm{N}_{\mathrm{UC}}^{\mathrm{qw}}$ and $\mathrm{N}_{\mathrm{UC}}^{\mathrm{bar}}$ are the numbers of unit cells in the effective volumes of the quantum well and the barrier part of the exciton, respectively. Each unit cell contains eight atoms, four ^{75}As and four $^{69/71}$Ga. The nuclear field created by a uniform nuclear polarization is therefore

$$\hat{B}_\alpha = a_{N\alpha}\frac{1}{g^\star \mu_B} 4 \cdot \mathsf{N}_{\mathsf{UC}} \cdot x_\alpha \left\langle \hat{I}_\alpha \right\rangle \tag{4.12}$$

x_α is the fraction of the nuclear species

$$x_{^{75}\mathsf{As}} = 1 \qquad x_{^{69}\mathsf{Ga}} = 0.6 \qquad x_{^{71}\mathsf{Ga}} = 0.4 \tag{4.13}$$

The maximum nuclear fields appear for a fully polarized system $\left\langle \hat{I}_\alpha \right\rangle = 3/2$ and are listed in table 4.3

L_z [nm]	$g^\star$	$\vec{B}_{^{75}\mathsf{As}}$ [T]	$\vec{B}_{^{69}\mathsf{Ga}}$ [T]	$\vec{B}_{^{71}\mathsf{Ga}}$ [T]	$\sum B_N$ [T]
20	-0.4	-2.97	-1.25	-1.48	-5.7
15	-0.3	-3.41	-1.44	-1.70	-6.55
10	-0.25	-4.74	-2.00	-2.36	-9.1
5	0.1	11.8	4.99	5.90	22.69

Table 4.3: The maximum nuclear field of each isotope calculated for a homogeneous polarization. The values for $g^\star$ are taken from Snelling et al. [48]

Comparison with the nuclear field calculation by Paget et al. [11] shows good agreement with the values calculated above. The sum of the nuclear fields in a 20 nm quantum well is 5.7 T, which is about three times smaller than in [11], on the other hand, the coupling constant is also scaled by a factor of three.

4.1.3 Electronic Magnetic Field

The static magnetic field created by the electrons acting on one nucleus can be calculated in a similar way to the calculation of the nuclear field in section 4.1.2. The maximum field created by an electron (spin, $S = 0.5$) at $\mathbf{r} = 0$ and with an infinite lifetime is given by the coupling constant, $a_{N\alpha}$, divided by the gyromagnetic ratio, γ_α, of the nucleus, α and multiplied by $|\psi_e(\mathbf{r})|^2 = \frac{1}{\mathsf{N}_{\mathsf{UC}}^{\mathsf{qw}}}$. For ^{75}As in the 20 nm quantum well, the field would be $B_e = 0.08\,\mu$T at each nucleus. A nucleus interacts only a fraction (Γ_t) of the total time with an electron. Thus, the strength of the magnetic field of electronic origin acting on a nucleus at a distance, $\mathbf{r}$, from the center of the exciton is

$$\left\langle \hat{B}_e^\alpha(\mathbf{r}) \right\rangle = \Gamma_t^{-1} a_{N\alpha} \frac{1}{\hbar\gamma_\alpha} |\psi_e(\mathbf{r})|^2 \left\langle \hat{S} \right\rangle \tag{4.14}$$

The value of Γ_t depends on the number of electrons in the sample and therefore on the intensity of the light. The power absorbed in a quantum well is

$$I^{qw} = I_0(1 - e^{-\alpha^{\mathrm{abs}} L_z}) \tag{4.15}$$

where I_0 is the intensity of the laser and α^{abs} the absorption coefficient. $\alpha^{\mathrm{abs}} = 10^5\,\mathrm{cm}^{-1}$ has been measured by Marquezini et al. [49] for a 7 nm quantum well and is taken to be independent of L_z here. The intensity of the laser is usually about 30 mW/area and is focused down to 100 μm in diameter. Therefore, the intensity absorbed in a 20 nm well is 5.4 mW/area. The energy of a photon in this quantum well is $E_{ph} = h \cdot c/\lambda$, and the number of photons absorbed per area and time is I^{qw}/E_{ph}. With $\lambda = 810\,\mathrm{nm}$, the number of photons per time is $2.2 \cdot 10^{16}\,\mathrm{s}^{-1}$. Each absorbed photon creates an electron in the conduction band, and the number of electrons per unit volume with a lifetime of 1 ns present in a 20 nm quantum well is about $2.2 \cdot 10^7$. The number of atoms in the excited volume is $3.6 \cdot 10^{11}$, therefore one electron is excited every 10000 nuclei. The electrons form excitons with a diameter that extends over several unit cells. With the values listed in table 4.2, one finds that each exciton in the 20 nm well extends over 10^5 ^{75}As nuclei, meaning that each nucleus feels 10 excitons at the same time. This gives the occupation rate to $\Gamma_t^{-1} = 10$. The maximum field created by the electrons without trapping is therefore $0.8\,\mu$T $(= B_e \cdot \Gamma_t^{-1})$.

4.1.4 Dynamic Nuclear Polarization

The electron spin, $\hat{S}$, precesses in the external magnetic field, B_0. The projection of $\hat{S}$ on the external field creates a magnetic field of electronic origin which is static during the lifetime of the electron. The components of $\hat{S}$ perpendicular to the external field create a fluctuating field felt by the nuclei. As in thermal relaxation, [41] these modulations of the hyperfine interaction cause dynamic polarization of the nuclear spin system as a relaxation process. The spin is transferred from the electron to the nuclear system by flip-flop processes which conserve the total spin. Hence, the balance equation for the steady state populations, N_m, of the nuclear spin levels has the form [42]

$$W_{m,m-1} N_m n_- = W_{m-1,m} N_{m-1} n_+, \tag{4.16}$$

where, m, is the projection of the nuclear spin on the direction of the external magnetic field, $\mathbf{B}_0$; $W_{m,m-1}$ the probability for a transition from state m to $m-1$; and $n_\pm = 1/2 \pm S$ are the populations of the electronic states with spin up or down. D'yakonov and Perel' [50] calculated the transition probabilities taking the modulation of the hyperfine interaction as a random perturbation to the external field. The populations for each energy state, m, follow the thermodynamic relation

$$N_m = \frac{1}{Z} e^{mx/I} \tag{4.17}$$

$$x = I\left(\frac{\hbar\Omega_e}{k_B T} + \ln\left[\frac{(1+2S)(1-2S_T)}{(1-2S)(1+2S_T)}\right]\right), \tag{4.18}$$

where $Z = \sum_m e^{mx/I}$ is a normalization factor, S is the mean value of the projection of the electron spin along the direction of the magnetic field, $\mathbf{B}_0$, Ω_e the precession frequency of the electron in the external magnetic field, and

$$S_T = -\frac{1}{2}\tanh\left(\frac{\mu_B g^\star B}{2k_B T}\right) \tag{4.19}$$

is the equilibrium value of the average electron spin. The temperature, T, in equation 4.18 is the temperature of the lattice, which has an infinite heat capacity [41] meaning that the lattice temperature is not affected by the optically pumped spin systems. The energy needed for the spin transitions is provided by the lattice [42].

A convenient way to calculate the populations of the different spin systems is the concept of a spin temperature [51], which will be used in this thesis. The basic idea of spin temperature theory is the assumption that the spin systems behave like systems described by thermodynamics. According to Goldman [51], the spin temperature hypothesis can be stated as follows: "A spin system isolated from the lattice and subjected to spin-spin interactions proceeds toward a state of internal equilibrium such that the probabilities of finding the system in any of its energy levels are given by a Boltzmann distribution, $e^{-E_i/k_B T_S}$." The distribution defines the spin temperature, T_S.

For the optically cooled electron system one can define a spin temperature, T_S, and the second term of equation 4.18 can be written as $-\hbar\Omega_e/k_B T_S$. The average nuclear spin, $\langle I\rangle = \sum_m mN_m$, created by dynamical polarization is expressed in terms of the Brillouin function [47]

$$I_0 = IB_I(x) \tag{4.20}$$

Equation 4.20 describes the polarization of the nuclear spin system due to a difference of spin temperature between the electrons and the lattice. The ratio, $\langle I_z\rangle / I$, is the limiting value of nuclear spin polarization depending on the polarization of the electron system.

The time dependence of the mean nuclear spin is, according to [50]:

$$\frac{d\langle I_z\rangle}{dt} = -\frac{1}{T_{1e}(r)}\left(\langle I_z\rangle - I_0\right) - \frac{1}{T_1}\langle I_z\rangle \tag{4.21}$$

where T_1 is the lattice relaxation time, and I_0 the steady state nuclear spin calculated with equation 4.20. The longitudinal nuclear spin relaxation time, $T_{1e}(\mathbf{r}_i)$, due to the hyperfine interaction is given by

$$\frac{1}{T_{1e}(\mathbf{r}_i)} = \Gamma_t^{-1} \frac{1}{\hbar^2} a_{N\alpha}^2 \left|\psi_e(\mathbf{r}_i)\right|^2 (1 - 4SS_T) \frac{\Gamma_e}{\Gamma_e^2 + \Omega_e^2} \tag{4.22}$$

where Γ_t^{-1} is the degree of occupation of a nucleus, Γ_e^{-1} is the time the electron is in the interaction range of a nucleus, and Ω_e is the precession frequency of the electron in the external field.

Non-localized excitons do not contribute to the polarization as can be shown by estimating Γ_e for these excitons. Assuming the diffusion of the excitons within the quantum well to be unrestricted, one can estimate the diffusion radius in a two-dimensional system with

$$\left\langle r^2 \right\rangle = 4Dt \tag{4.23}$$

With a diffusion coefficient, $D = 20\,\text{cm}^2/s$, [52] and the lifetime, $\tau_r = 10^{-9}$s, [53] one gets $r = 2.8\,\mu$m. Comparing this radius with the effective radius of the exciton in a 20 nm well from table 4.2 shows that the mobile exciton sees $6 \cdot 10^4$ more nuclei than a trapped exciton. Hence, the electron spends a time of $\Gamma_e^{-1} = \tau_r \cdot (6 \cdot 10^4)^{-1} = 1.7 \cdot 10^{-14}$ s at a nucleus. Therefore, the relaxation time at $\mathbf{r} = \mathbf{0}$ in zero field, setting $\Gamma_t^{-1} = 10$ s (s. section 4.1.3) and $\Gamma_e^{-1} = 1.7 \cdot 10^{-14}$ s, gives $T_{1e}(0) = 10^6$ s for ^{75}As in a 20 nm quantum well. This value is much longer than spin lattice relaxation time, T_1, of the nuclei which is on the order of a few 100 seconds.

4.1.5 Electron Localization

As has been seen in the previous chapter, the hyperfine interaction of nuclei with electrons of non-localized excitons is too small to produce significant nuclear polarization. The samples under investigation in this thesis are MBE-grown materials and therefore are very ordered and pure, meaning localization due to impurities can be excluded due to the low concentration of defects in the investigated samples. The most probable reason for localization is trapping of the excitons at defects of the interface between the GaAs and AlGaAs layers [37] [54] [55] [56] [57]. Even in high quality MBE-grown quantum wells, the hetero-interface is not truly smooth but usually shows deviations in the well width of 1 monolayer. These deviations of thickness are on different lateral length scales, L. Depending on the size of the lateral defects, a classification of the interface roughness can be obtained [58]. The interface is called *pseudo smooth* if L is much smaller than the diameter of the exciton, $a_B^\star$. The exciton sees, in this case, a distribution of different well widths. When L is larger than $a_B^\star$, the interface is called *smooth*. Finally when L is on the order of the exciton Bohr radius, the interface is called *rough*. The excitons are trapped in islands of different thickness which have diameters much larger than [59], or on the order of [58], the Bohr radius of the exciton. Jahn et al. [60] have shown that the localization in the wide well regions is stronger than in the narrow well regions because of the low confinement energy. Hence, after creating an exciton anywhere in the quantum well, it diffuses to a wide well region. At low temperatures, subsequent diffusion between different islands does not occur [54] because of the monolayer potential step. This effect leads to various regions in the quantum well with high and low exciton concentrations.

Unfortunately, there is no information about the exact size, density and distribution of the trapping islands in the samples investigated herein. In order to demonstrate the influence of localization on the polarization of the nuclei, one can use the following model.

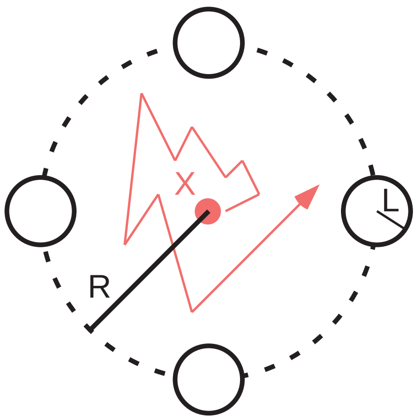

Figure 4.1: Model for exciton trapping at interface defects. The exciton X (red) is excited between defect islands of radius, L, and diffuses within the diffusion radius, R.

Picture a quantum well with lateral defects having radii of $L = 50\,\text{nm}$ within a distance of $1\,\mu$m from center to center ($R = 0.5\,\mu$m) as depicted in figure 4.1. An exciton created between these defects has a diffusion radius of $0.5\,\mu$m during its lifetime. The probability for an exciton to be trapped by the nearest neighbor trapping site is given by the ratio of the circumference of the diffusion circle to the diameter of the interface defects multiplied by their number

$$f = \frac{2\pi R}{4 \cdot 2L} = \frac{R}{4L}\pi \tag{4.24}$$

This means that after $f^{-1} \cdot 3.125 \cdot 10^{-11}\,\text{s} = 5 \cdot 10^{-10}\,\text{s}$, the exciton is trapped in a region of wider well width (see equation 4.23). The exciton stays at the trapping site for $5 \cdot 10^{-10}\,\text{s}$ and diffuses within this area. The number of nuclei interacting with the electron is 10 times bigger than for the case of non-diffusing excitons. This leads to an interaction time of the electron per nucleus of $\Gamma_e^{-1} = 5 \cdot 10^{-11}$s, reducing the hyperfine relaxation time to $T_{1e}(0) = 40\,\text{s}$.

Despite the simplicity of this model it demonstrates the enormous influence of trapping the excitons at interface defects. Following the classification of roughness [58], the interface in the model is considered to be "smooth" but still

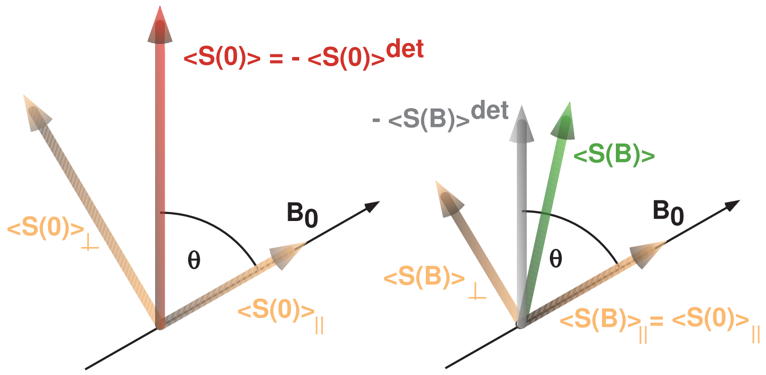

Figure 4.2: The classical picture of the Hanle effect. Left: Optical excitation of the spins creates average spin $\langle S(0) \rangle$ in zero external field colinear with the laser excitation axis. B_0 is only shown to indicate the z-direction of the coordinate system. Right: Applying an external field, $B_0 = B$, causes precession of the spin component perpendicular to the field, $\langle S(B) \rangle_{\perp}$. The parallel component, $\langle S(0) \rangle_{||}$, remains constant. Therefore, the average spin $\langle S(B) \rangle$ becomes field dependent, for which the projection on the excitation axis is detected.

it is rough enough to trap excitons. The PL spectra of the samples investigated during this work show very narrow emission lines implying smooth interfaces. However, even a small density of defects can lead to a huge increase in the interaction probability between electrons and nuclei as was shown by the model.

4.2 Optical Detection

In the previous sections, the transfer of the polarization of the optically oriented electrons to the nuclear spin system has been discussed in detail. The influence of the nuclear field on the optical orientation of the electrons will be the subject of this section. This influence on electrons in semiconductors was directly proven by Ekimov and Safarov [3], who discovered resonance changes in the degree of circular polarization of luminescence under NMR. These changes are due to variations of the absolute value and the direction of the nuclear field during the passage of magnetic resonance. The influence of magnetic fields on the polarization of orientated electrons is called the Hanle effect. This effect will be discussed in detail for two cases, with purely external fields, and with both external and nuclear fields in sections 4.2.1 and 4.2.2, respectively.

The Hanle effect was first discovered and studied in the resonance fluorescence of gases [61], but it also plays an important role in spin orientation in semiconducting materials. In the classical picture the electron spins start to precess in the presence of a magnetic field, B_0, which is oblique with respect to the orientation of light propagation. Because of spin relaxation and the finite lifetime of the excited electrons, the average spin component perpendicular to the magnetic field, $\langle S(B)\rangle_{\perp}$, decreases with increasing field strength. This leads to an observable decrease in the average electron spin in the direction of detection, $\langle S(B)\rangle$, as shown in figure 4.2. The source for a magnetic field in the case of semiconductor materials is an external magnetic field, B_0, as well as the field produced by the nuclei, B_N, through the hyperfine interaction. The influence of the different sources of magnetic fields are treated separately in the following sections.

4.2.1 The Hanle Effect in an External Field

In the experiment, an average spin is observed which involves a large ensemble of electron spins. A powerful method to treat a large spin system is the density matrix formalism as shown by Fano [62]. The spin system as a whole is represented by its density matrix, ρ, and the Hamiltonian operator, $\mathcal{H}$. The diagonal components, ρ_{ii}, of the density matrix represent the populations of the different energy levels, and the off-diagonal components are coherence terms. Throughout this work, rows and columns of the density matrix are sorted in the following way: $m, m-1, \ldots, -(m-1), -m$ from left to right and top to bottom. The time evolution of the density matrix is described by the Von Neumann equation, which has been extended by including the relaxation rates and the optical pumping rate $\tilde{P}'$:

$$\frac{\partial \rho}{\partial t} = -\frac{i}{\hbar}[\mathcal{H}, \rho] - \tilde{\Gamma}_r - \tilde{\Gamma}_s + \tilde{P}' \tag{4.25}$$

where $\tilde{\Gamma}_r$ is the matrix which describes the recombination of the electron from the conduction to the valence band, and $\tilde{\Gamma}_s$ is the matrix for the spin relaxation within the conduction band. The continuous optical pumping of electrons from the valence band to the conduction band is represented by the matrix, $\tilde{P}'$. The values for transverse and longitudinal relaxation times can be taken to be equal [41].

The geometry of the optical pumping setup in an external field is depicted in figure 4.3. Defining the z-direction as the direction of the magnetic field, the Hamiltonian is diagonal and has the form

$$\mathcal{H} = \omega \cdot S_z = \frac{\omega\hbar}{2}\sigma_z. \tag{4.26}$$

With pure left-hand circularly polarized light and a wavelength tuned to the heavy hole transition, only the spin state, ρ_{11}, in the conduction band becomes populated. The matrix for optical pumping in the coordinate system of the

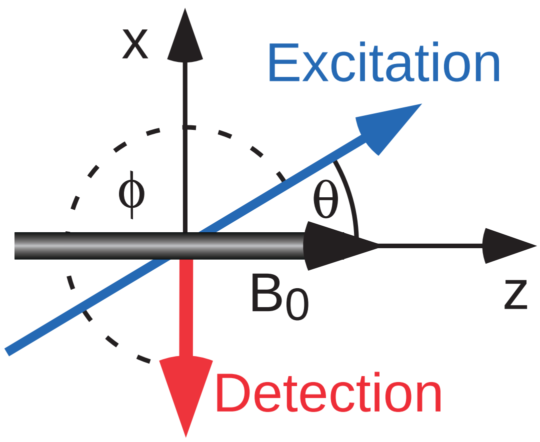

Figure 4.3: The orientation of the excitation light with respect to the external field.

excitation is

$$\tilde{P} = \begin{pmatrix} P & 0 \\ 0 & 0 \end{pmatrix} \tag{4.27}$$

The optical excitation takes place under an angle, θ, with respect to the external field. To include the optical pumping into equation 4.25, $\tilde{P}$ has to be rotated around the y-axis by θ

$$\tilde{P}' = e^{i\frac{\theta}{2}\sigma_y}\tilde{P}e^{-i\frac{\theta}{2}\sigma_y} \tag{4.28}$$

Therefore, the equations of motion for each of the density matrix components, ρ_{ij}, are

$$\begin{array}{lcccccc} \dot{\rho}_{11} & = & & -\Gamma_r\rho_{11} & -\frac{1}{2}\Gamma_s(\rho_{11}-\rho_{22}) & +Pcos^2\frac{\theta}{2} \\ \dot{\rho}_{22} & = & & -\Gamma_r\rho_{22} & -\frac{1}{2}\Gamma_s(\rho_{22}-\rho_{11}) & +Psin^2\frac{\theta}{2} \\ \dot{\rho}_{12} & = & -i\omega\rho_{12} & -\Gamma_r\rho_{12} & -\Gamma_s\rho_{12} & -Psin\frac{\theta}{2}cos\frac{\theta}{2} \\ \dot{\rho}_{21} & = & i\omega\rho_{21} & -\Gamma_r\rho_{21} & -\Gamma_s\rho_{21} & -Psin\frac{\theta}{2}cos\frac{\theta}{2} \end{array} \tag{4.29}$$

The average spin in the magnetic field direction $\langle S_z\rangle$ is proportional to the population difference, and the average transverse spin components, $\langle S_x\rangle$ and $\langle S_y\rangle$, are proportional to the real and imaginary part of the coherence, respectively. Therefore, equation 4.29 is rewritten in the following way

$$\begin{array}{lcccccc} \dot{\Lambda} & = & & -\Gamma_r\Lambda & -\Gamma_s\lambda & +Pcos\theta \\ \dot{\Sigma} & = & & -\Gamma_r\Sigma & & +P \\ \dot{X} & = & -\omega Y & -\Gamma_r X & -\Gamma_s X & -Psin\theta \\ \dot{Y} & = & \omega X & -\Gamma_r Y & -\Gamma_s Y & \end{array} \tag{4.30}$$

with the substitutions: $\Lambda = \rho_{11} - \rho_{22}$, $\Sigma = \rho_{11} + \rho_{22}$, $X = \rho_{12} + \rho_{21}$, and $Y = i(\rho_{12} - \rho_{21})$. The detection rate of the experiment is much slower than the precession and relaxation rates of the electrons, which means that the system is always in the steady state. Thus, the derivatives of equation 4.30 vanish and can be solved exactly.

$$\begin{array}{rcl} \Lambda & = & P\frac{cos\theta}{\Gamma_r+\Gamma_s} \\ \Sigma & = & \frac{P}{\Gamma_r} \\ X & = & -P\frac{(\Gamma_r+\Gamma_s)sin\theta}{(\Gamma_r+\Gamma_s)^2+\omega^2} \\ Y & = & -P\frac{\omega sin\theta}{(\Gamma_r+\Gamma_s)^2+\omega^2} \end{array} \tag{4.31}$$

The expectation value, $\langle A \rangle$, of an operator, A, is calculated in general as $\langle A \rangle = \mathrm{Tr}\{A\rho\}$. Normalized to the total population in the conduction band, the expectation values of the three electron spin components are

$$\begin{array}{rcccccl} \langle S_x \rangle & = & \mathrm{Tr}\{S_x\rho\} & = & \frac{1}{2}\frac{X}{\Sigma} & = & -S_0\frac{\Delta\omega^2 sin\theta}{\Delta\omega^2+\omega^2} \\ \langle S_y \rangle & = & \mathrm{Tr}\{S_y\rho\} & = & \frac{1}{2}\frac{Y}{\Sigma} & = & -S_0\frac{\Delta\omega\cdot\omega sin\theta}{\Delta\omega^2+\omega^2} \\ \langle S_z \rangle & = & \mathrm{Tr}\{S_z\rho\} & = & \frac{1}{2}\frac{\Lambda}{\Sigma} & = & S_0 cos\theta \end{array} \tag{4.32}$$

The equilibrium spin, S_0, is the value of the spin in the absence of a magnetic field and therefore determined by the relaxation rates, Γ_r and Γ_s by:

$$S_0 = \frac{1}{2}\frac{\Gamma_r}{\Gamma_r + \Gamma_s} \tag{4.33}$$

The quantity

$$\Delta\omega = \Gamma_r + \Gamma_s \tag{4.34}$$

is also defined by the relaxation rates and will turn out to be the width of the Hanle curve. Equation 4.32 mirrors what has been explained classically in the introduction. The component parallel to the external field is independent of the field, whereas the two other components show a field dependence. The components decrease with increasing field due to the precession in the magnetic field. The detection polarization, $\langle S_z \rangle^{det}$, can be calculated by transforming the vector, $\langle \vec{S} \rangle = (\langle S_x \rangle, \langle S_y \rangle, \langle S_z \rangle)$, into the coordinate system of detection. The orientation of the sample is shown in figure 4.4. The detection is antiparallel to the excitation with a deviation, ξ, giving a transformation angle, $\phi = 180° + \theta + \xi$. The angle, ξ, is determined by the geometry of the experiment and the refraction of light at the interface:

$$\xi = arcsin\left(\frac{sin(90° - \theta)}{n_{GaAs}}\right) \tag{4.35}$$

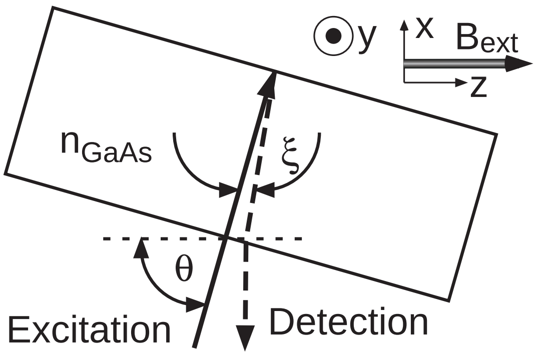

Figure 4.4: Sketch of the orientation of the quantum well sample in the experimental setup. The external field points in the z-direction. The excitation is parallel to the growth direction of the quantum wells, and the detection is antiparallel and slightly off-angle from the excitation. The deviation, ξ, can be neglected, as shown in the text.

Using $n_{GaAs} = 3.3$ [63] and $\theta = 74°$ as typical values from the experiment, gives $\xi = 4.8°$. This small value can be neglected for simplicity, and $\langle \vec{S} \rangle$ is rotated by $\phi = 180° + \theta$ around the y-axis, giving the well-known equation for the detected spin polarization (Hanle curve)

$$\langle S_z \rangle^{det} = S_0 \frac{\Delta B^2 + B_0^2 cos^2\theta}{\Delta B^2 + B_0^2}. \tag{4.36}$$

This equation describes a Lorentzian curve with the maximum, S_0, and the width, $\Delta B = \gamma \Delta\omega$, which have been defined previously. The maximum is at $B_0 = \gamma\omega = 0$, and the polarization drops to zero for high fields for the transverse case ($\theta = 90°$). The polarization has the constant value, S_0, in the longitudinal setup ($\theta = 0$). Figure 4.5 shows Hanle curves for different angles, θ, between the external field and the excitation path.

4.2.2 Influence of Nuclear Fields

If polarization of the nuclear spin system is established, the electrons feel a magnetic field of nuclear origin as shown in section 4.1.2, termed the nuclear field. In steady state conditions, such as when the transverse components of the nuclear field are relaxed, the Hamiltonian in equation 4.26 changes to

$$\begin{aligned} \mathcal{H} = & \ (\omega + \omega_{Nz}) \cdot S_z \\ = & \ \tfrac{(\omega + \omega_{Nz})}{2} \sigma_z \end{aligned} \tag{4.37}$$

where ω_{Nz} is the nuclear field component parallel to the external field. Inserting this Hamiltonian into equation 4.25 leads to a new set of equations of motion for

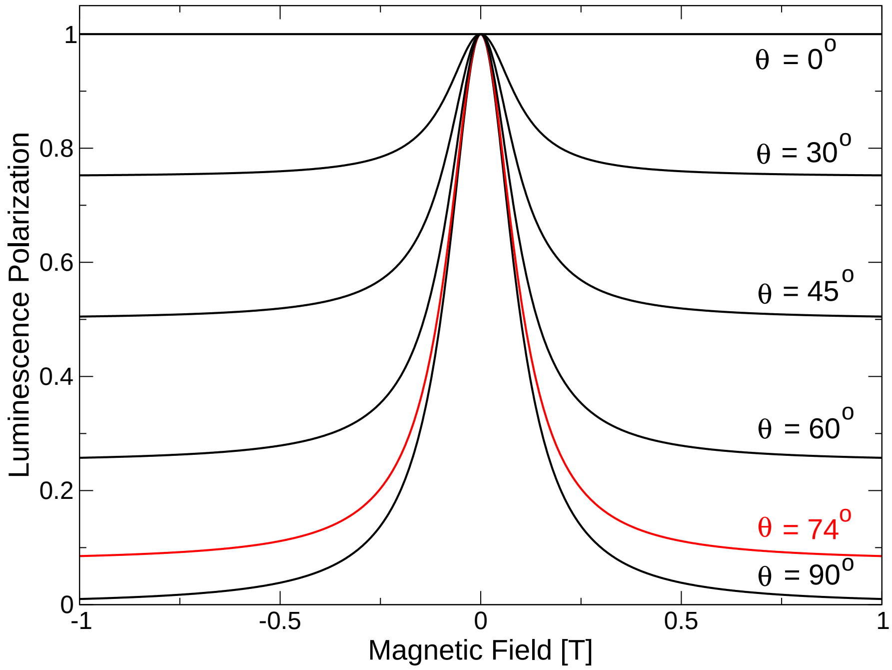

Figure 4.5: Calculated Hanle curves for different angles, θ. The red curve is the theory trace for the angle used in the experimental setup.

the elements of the density function. With the substitution for ρ_{ij} in expressions Λ, Σ, X and Y as explained in the previous section, the equations of motion become

$$\begin{aligned}
\dot{\Lambda} &= -\Gamma_r\Lambda - \Gamma_s\Lambda + Pcos\theta \\
\dot{\Sigma} &= -\Gamma_r\Sigma + P \\
\dot{X} &= -(\omega + \omega_{Nz})Y - \Gamma_r X - \Gamma_s X - Psin\theta \\
\dot{Y} &= (\omega + \omega_{Nz})X - \Gamma_r Y - \Gamma_s Y
\end{aligned} \tag{4.38}$$

In the steady state, this system can be solved exactly as in the case without nuclear polarization. The expectation values for the three spin components then become

$$\begin{aligned}
\langle S_x \rangle &= -S_0 \frac{\Delta\omega^2 sin\theta}{\Delta\omega^2 + (\omega+\omega_{Nz})^2} \\
\langle S_y \rangle &= -S_0 \frac{\Delta\omega\cdot(\omega+\omega_{Nz}) sin\theta}{\Delta\omega^2 + (\omega+\omega_{Nz})^2} \\
\langle S_z \rangle &= S_0 \frac{\Delta\omega^2 cos\theta + (\omega+\omega_{Nz})^2 cos\theta}{\Delta\omega^2 + (\omega+\omega_{Nz})^2}
\end{aligned} \tag{4.39}$$

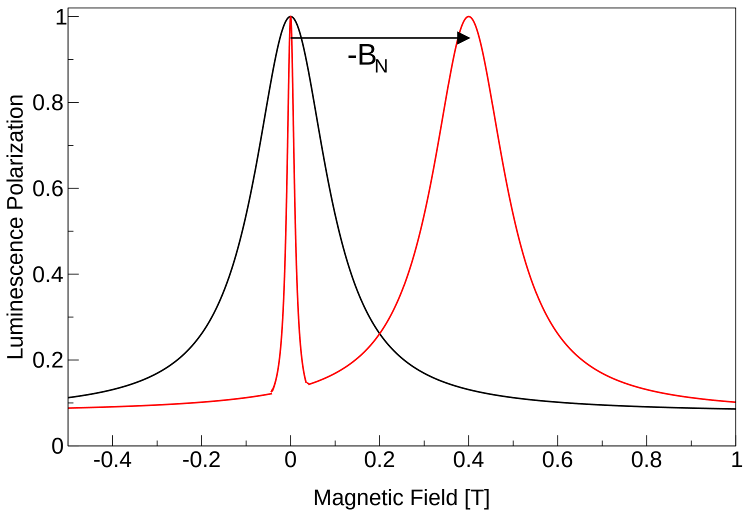

Figure 4.6: Hanle curve with (red) and without (black) the influence of the nuclear field.

The transformation into the coordinate system of detection is accomplished as before, resulting in the Hanle curve with a nuclear magnetic field, given by:

$$\langle S_z \rangle^{det} = S_0 \frac{\Delta B^2 + (B_0 + B_N)^2 cos^2\theta}{\Delta B^2 + (B_0 + B_N)^2} \tag{4.40}$$

A calculated example for a Hanle curve with and without the influence of the nuclear field is given in figure 4.6. These are Lorentzian curves, and the Hanle curve with the nuclear filed has a maximum at $-B_N = \gamma^{-1}\omega_N$, in other words, when the nuclear field compensates the external magnetic field. As can be seen from equation 4.40, the shift of the Hanle curve is a direct measure of the size of the nuclear field acting on the electrons. Any changes in the nuclear polarization lead to changes of the nuclear magnetic field and hence to a shift of the Hanle curve. Therefore, nuclear magnetic resonance can be detected by observing changes in the amplitude of the luminescence polarization.

For low external fields, a second peak appears at $\mathbf{B} = \mathbf{0}$. If the external field is smaller than the local field due to nuclear spin–spin coupling, no nuclear polarization can be established. Thus, the nuclear field is very small, and the electrons experience a zero total field so that their mean spin is S_0. This results in the extra peak centered at zero field and is superimposed on the Lorentzian curve.

4.3 Experimental Results

The optically detected nuclear magnetic resonance experiment in an oblique field is based on the shift of the Hanle curve due to changes of the nuclear polarization. Since the optically detected signal is a convolution of the Hanle curve with the resonance line of the nuclear system, it is necessary to know the details of the Hanle curve in order to deconvolute the NMR signal. In the following section, measurements of the Hanle curve without nuclear polarization are presented.

The investigation of the depolarization function of the electrons with the influence of nuclear magnetic fields offers the possibility to measure the size of these fields. These studies have been carried in detail for the 19.7 nm quantum well, and the results are presented in section 4.3.2.

4.3.1 Hanle Curves

The setup for measuring the Hanle curves in an oblique field is shown in figure 3.1. In order to suppress the buildup of nuclear polarization, the PEM is placed into the excitation path, as discussed in section 3.2. Since the nuclear relaxation rate due to optically orientated electrons is much shorter than the modulation frequency, no nuclear polarization can occur.

The quantum wells are excited resonantly, and the wavelength of the spectrometer is shifted to a higher wavelength for a few tenth of nanometers. This setup suppresses most of the stray laser light from the sample.

Examples for Hanle curves from different quantum wells are depicted in figures 4.7 to 4.12, which all stem from sample $\#1431$. The experimental data can be fitted with equation 4.40, and the fit of each Hanle curve is also plotted as the superimposed red line in each of figures 4.7 to 4.12. Unfortunately, the stray laser light cannot be suppressed completely; therefore, a polarization offset from the laser must be taken into account for the fit. The results of the fits are given in the caption of each figure.

From section 4.2.1, it is clear that the width of the Hanle curve is inversely proportional to the gyromagnetic ratio of the electron, and therefore inversely proportional to the effective g-value, $g^{\star}$. As experimentally shown by Snelling et al. , [48] the g-value has a strong dependence on the well width. The electron in the quantum well sees in the growth direction a mixture of the g-values of GaAs ($g = -0.44$ [28]) and AlGaAs ($g = +0.4$ [64]) with an increasing influence of the barrier at small well widths. This mixture of g-values also means that the effective g-value, $g^{\star}$, is zero for a certain well width. Variation in $g^{\star}$ should lead to a well width (L_z) dependence of the Hanle width, ΔB, resulting in very broad Hanle curves for small wells with g-values close to zero. Figure 4.12 shows an example for such a broad Hanle curve. It is not possible to fit the data with

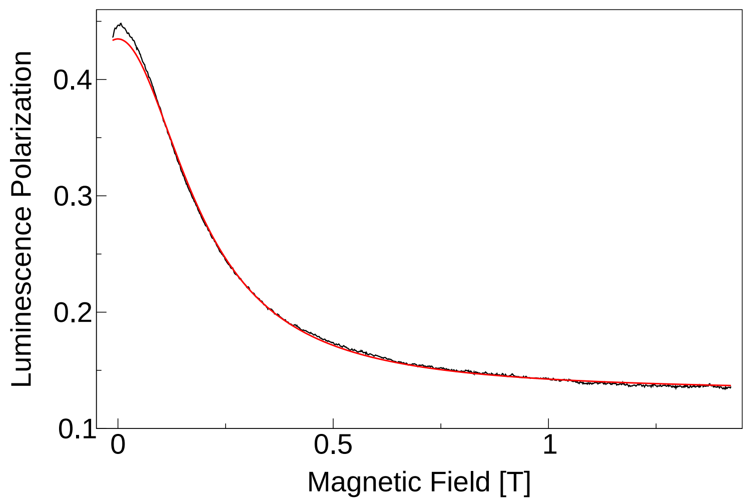

Figure 4.7: Hanle curve of the 19.7 nm quantum well. The fit parameters are: amplitude 0.34, Hanle width 0.19 T, laser offset 0.10.

high certainty in this case because the magnetic field in this experiment is much smaller than the Hanle width. However, it is clear that the width is on the order of several Tesla.

The well width also depends on the recombination ($\tau_r = \frac{1}{\Gamma_r}$) and spin relaxation ($\tau_s = \frac{1}{\Gamma_s}$) times of the electrons, both of which have a temperature dependence. Figures 4.10 and 4.11 both show Hanle curves from the 10.5 nm wide quantum well. These have been measured on different days, and the sample has been re-glued between these two experiments. The width of the Hanle curve in figure 4.11 is about twice as big as in figure 4.10 indicating some difference in the physical properties leading to different curve widths. Recall that the polarization is proportional to the recombination rate, Γ_r, and inversely proportional to the Hanle width, ΔB. Since the polarization is constant in both experiments within the error of the fit, the recombination time is twice as long in the case of figure 4.10 as in figure 4.11, indicating a higher temperature of the sample in the latter case.

Unfortunately, the experimental setup does not provide the possibility of direct measurement of the temperature of the sample, which depends strongly on the intensity of the laser, the thermal contact with the sample holder, and the spot size of the laser. The latter two points are hard to control in the setup and might change from experiment to experiment. Therefore, the width of the Hanle curve is an important indicator of the actual temperature of the sample.

The effective g-values for the quantum wells under investigation in this project are not known. For an estimation of the recombination times, one can use the

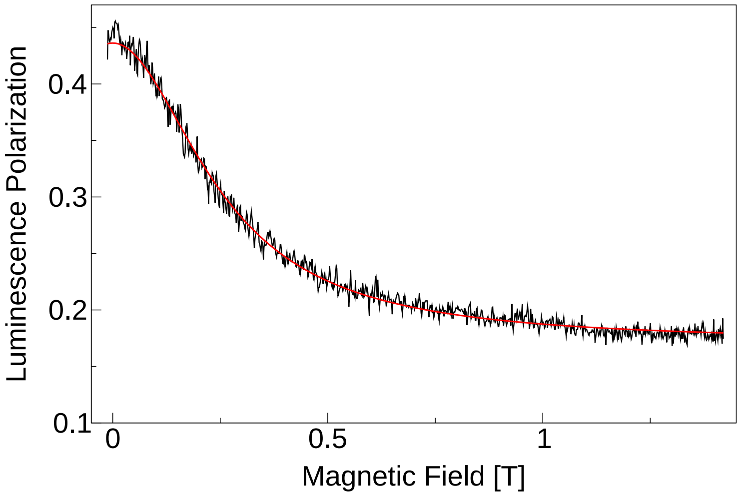

Figure 4.8: Hanle curve of the 14.5 nm quantum well. The fit parameters are: amplitude 0.14, Hanle width 0.18 T, laser offset 0.16.

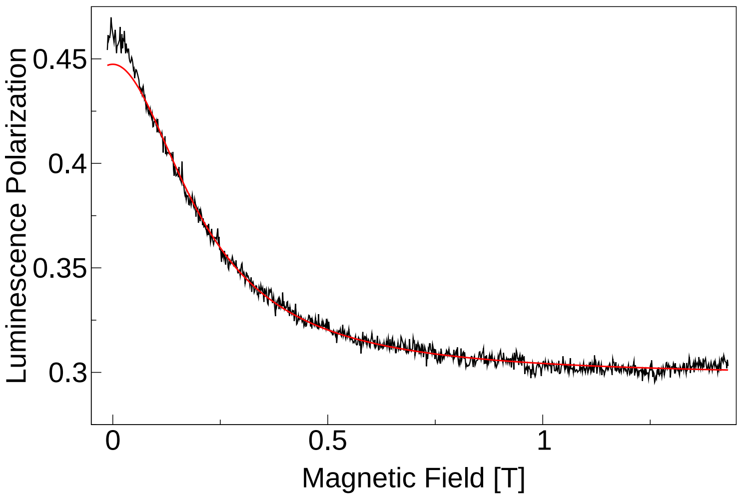

Figure 4.9: Hanle curve of the 11.7 nm quantum well. The fit parameters are: amplitude 0.16, Hanle width 0.26 T, laser offset 0.13.

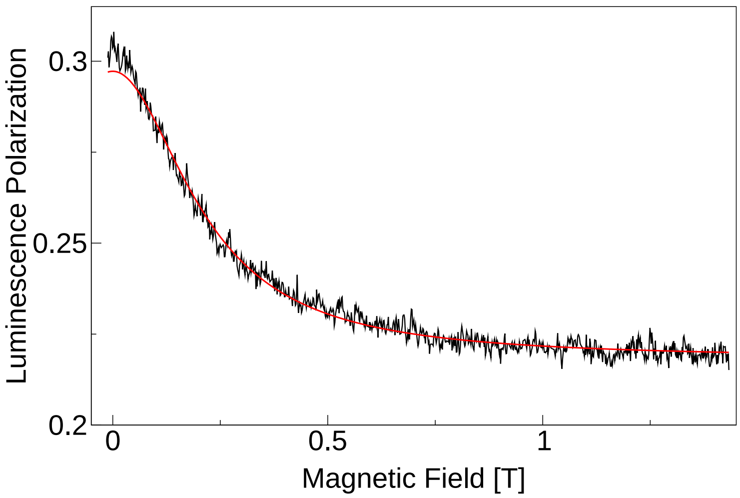

Figure 4.10: Hanle curve of the 10.5 nm quantum well. The fit parameters are: amplitude 0.09, Hanle width 0.22 T, laser offset 0.21.

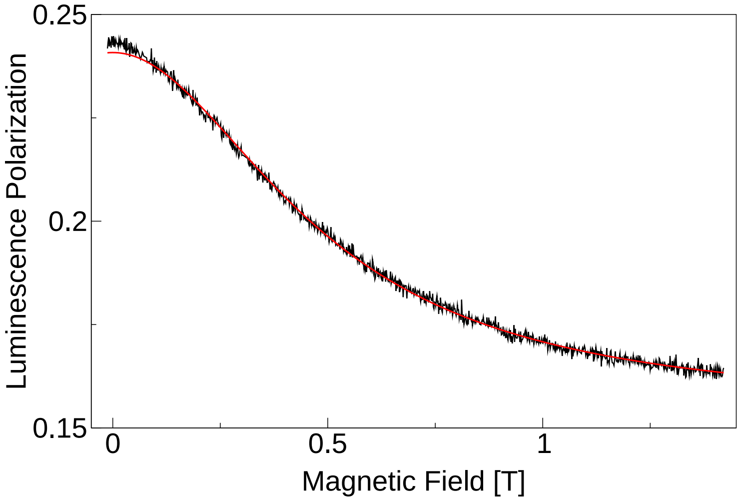

Figure 4.11: Hanle curve of the 10.5 nm quantum well. The fit parameters are: amplitude 0.10, Hanle width 0.48 T, laser offset 0.14. The difference in width from figure 4.10 is due to different sample temperatures, as explained in the text.

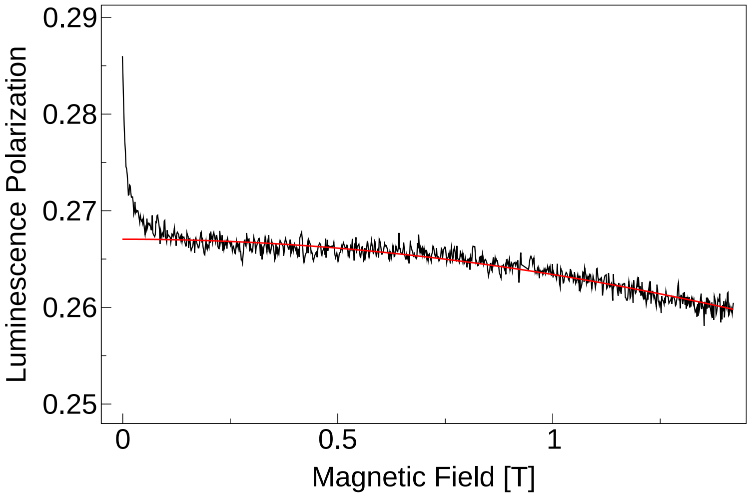

Figure 4.12: Hanle curve of the 6.8 nm quantum well. The fit parameters are: Hanle width about 8 T. The sharp increase at zero magnetic field indicates high laser intensities, as discussed in the text.

values from Snelling et al. [48]. Snelling reports recombination times on the order of a nanosecond, which were used in the calculation for the magnetic fields in the theory sections of this chapter. It is not possible to determine the recombination times with higher accuracy, since the g-values in reference [48] are different from the ones in the experiments described here (to be shown in section 4.3.2). One reason for the difference is the different barrier material in the investigated samples, and the other is a dependence of the g-value on the hole concentration, which is not controlled in the experiments carried out during this work.

In figure 4.12 a peak at zero field is very noticeable but is significantly attenuated in the other graphs of the Hanle curves. An explanation for this effect is proposed by Ekimov et al. [4]. The modulated electron polarization can create nuclear polarization if the electronic field is oscillating at a frequency close to the NMR frequency [65]. This condition is fulfilled for low external magnetic fields. The electrons lose their polarization due to the hyperfine coupling with the nuclei, and they themselves lose their polarization with some time constant. If the coupling time constant is longer than the nuclear relaxation constant, the electrons therefore will couple with unpolarized nuclei continuously. At high excitation intensities, however, the electrons couple with the already polarized nuclei, slowing down the spin relaxation of the electrons on the nuclei and causing an increase in the stationary spin orientation of the electrons. This situation is valid only at low magnetic fields. At higher fields, no nuclear polarization can be created;

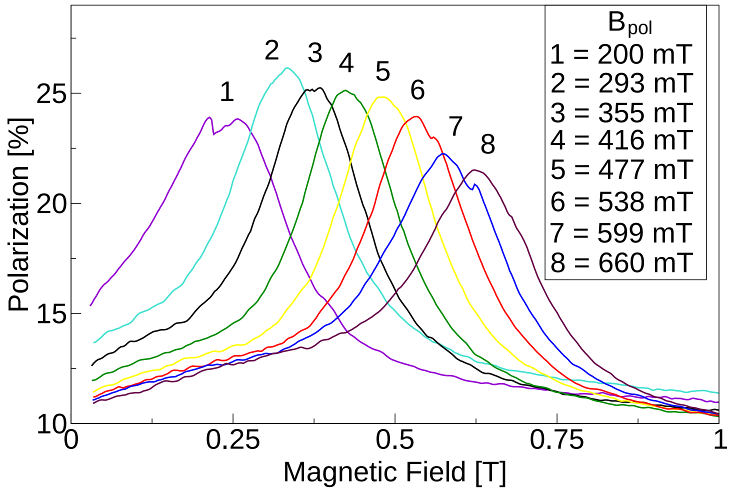

Figure 4.13: Hanle curves of 19.7 nm quantum well (sample $\#1431$). Before measuring, each curve of the system has been polarized for a long time at the external field, B_{pol}. The curves are a compound of two scans, one from $B_{pol} \to B_{max}$ and one from $B_{pol} \to 0$

therefore, the electrons couple with unpolarized nuclei, as in the low excitation situation. Therefore, the stationary orientation decreases rapidly. This effect is more intense when the electronic field is larger, which is observed in the smallest quantum well, as can be seen from the figures 4.7 to 4.12.

4.3.2 Direct Measurement of the Nuclear Field

It has been shown in section 4.2.2 that a nuclear magnetic field, B_N, shifts the maximum of the Hanle curve from zero to $-B_N$. In order to measure this shift, the nuclear spin system has to be polarized. Nuclear polarization in quantum wells is established in all samples, even in sample $\#1294$, which has the highest interface quality.

Displaced Hanle curves are measured after a pumping time which is sufficiently long to polarize the nuclear system to an equilibrium value. After pumping, the external field is scanned up to its maximum value, and simultaneously the luminescence polarization is recorded. Then, the field is set to the previous value again to pump the system to its equilibrium polarization. Another scan down to zero external magnetic field with the same scan rate as before yields a complete picture of the displaced Hanle curve. Examples for displaced Hanle curves in a 19.7 nm quantum well are shown in figure 4.13.

Each curve in figure 4.13 has been taken after pumping at a different external magnetic field. The graph clearly shows that the maximum of the Hanle curve is always positioned at the value of the external field where the nuclear system has been pumped. Hence, the equilibrium nuclear field is always $B_N = -B_{pol}$. This effect cannot be explained by the spin temperature concept from D'yakonov (introduced in section 4.1.4) in which the maximum nuclear polarization depends only on the size of the electron polarization. The experimental results clearly reveal a dependence of the equilibrium value of the nuclear polarization on the external field. The positions of the Hanle curves indicate a preference of the electron-nuclear system to establish an effective field for the electrons close to zero. The Hamiltonian for the coupled system in a magnetic field is:

$$\mathcal{H} = -\Omega_e \hat{S}_z - \omega_0 \sum_i \hat{I}_z^i - a_N \sum_i \hat{I}^i \hat{S} \tag{4.41}$$

where Ω_e is the Larmor frequency of the electron in the *external* magnetic field, ω_0 the nuclear precession frequency, and the sum is over all nuclei within the Bohr radius of the exciton. Presumably, the transfer of the polarization is most effective for equal energy splittings of the electron and nuclear system. In that case, the transfer is energy conserving, and the lattice does not have to provide the energy for the spin flip. This situation is achieved if the coupling term in the Hamiltonian almost cancels out the Zeeman term of the electron. The nuclei are still exposed to the external field (in other words, the effect of the electronic field can be neglected as shown in section 4.1.3). As the nuclear system is polarized, the coupling efficiency increases, until the effective field for the electrons is close to zero. Further increase of nuclear polarization would reverse the sign of the effective field; therefore, the system tries to reduce nuclear polarization, in order to increase coupling efficiency again. Hence, the Hanle curve is locked at the position of the polarizing external field.

The locking of the Hanle curve is very obvious in figure 4.14, measured for each isotope separately. During the scan from high field to negative low field, the Hanle curve is pulled by the external field within some range. The noise of the polarization is most likely due to the unstable effective magnetic field of the unsaturated nucleus experienced by the electrons since it vanishes on the edges of the "Hanle curve".

The displaced Hanle curves in figure 4.13 are broadened compared to the ones without nuclear polarization. This fact indicates a distribution of nuclear fields felt by the electrons during their lifetime. As pointed out in section 4.1.5, only the electrons trapped at interface defects create a discernable nuclear polarization. In the space between two trapping sites, the remaining nuclear spins can be polarized only by spin diffusion. If the density of interface defects is low, in other words, the distance between two trapping sites is bigger than the nuclear spin diffusion radius, no homogeneous nuclear polarization can be established.

Spin diffusion is a spin-energy conserving process driven by the nuclear spin-spin couplings [41]. The spin diffusion rates determine to what extent nuclei outside the trapping site are polarized. The spin diffusion constant has been calculated and measured for ^{75}As to be 10^{-13} cm^2/s [13]. Since the electrons are created at any place within the spot of the laser in the quantum well, they feel an average of the nuclear magnetic fields within their diffusion radius. Since some electrons are trapped for most of their lifetime and some are free (not trapped at any time), the electron polarization reveals a distribution of nuclear fields at the time of recombination which broadens the observed Hanle curve.

The equilibrium value of nuclear polarization has a maximum value which is indicated by the decrease of the amplitude of the displaced Hanle curves. At high fields, other relaxation processes become more efficient than the relaxation due to optically oriented electrons. The maximum of the total nuclear field (as a sum of the fields of each isotope, ^{69}Ga, ^{71}Ga and ^{75}As) is bigger than the maximum external field created by the magnet. Therefore, in order to measure the maximum field, each isotope is investigated separately. The polarization of two isotopes is destroyed by saturating the NMR transitions at the pumping field; the depolarization of the electrons then depends only on the external field and the nuclear polarization of the one remaining isotope. The luminescence polarization is measured by changing the pumping field stepwise and saturating the NMR transitions at each step. This way the maximum nuclear field can be measured with an error of approximately 20 mT, and sample values for the 19.7 nm quantum well are:

$$\begin{aligned} ^{69}\text{Ga:} &\quad 475\,\text{mT} \\ ^{71}\text{Ga:} &\quad 460\,\text{mT} \\ ^{75}\text{As:} &\quad 880\,\text{mT} \end{aligned}$$

These are very high values for the nuclear field compared to the theoretical values calculated in section 4.1.2. Based on the theoretical nuclear fields, the polarization of each isotope is:

$$\begin{aligned} ^{69}\text{Ga:} &\quad 38\% \\ ^{71}\text{Ga:} &\quad 31\% \\ ^{75}\text{As:} &\quad 29\% \end{aligned}$$

These polarizations are much higher than predicted by the spin temperature concept using the average electron spin polarizations observed (about 10% electron polarization, which can generate a maximum of 15% nuclear polarization).

The measurement of the nuclear fields in the 14.5 nm quantum well is carried out in a different way. The system is polarized at maximum field (1.292 T), and the polarizations of two isotopes are destroyed under NMR conditions. After a sufficient time of pumping, the RF is turned off, and the field is scanned down to negative field very rapidly while recording the luminescence polarization and the external field value. The scans for all three isotopes are depicted in figure 4.14.

The positions of the maximum fields are marked in the graphs, and the field values are

$$\begin{aligned} {}^{69}\text{Ga:} \quad 480\,\text{mT} &\;\hat{=}\; 28\% \\ {}^{71}\text{Ga:} \quad 460\,\text{mT} &\;\hat{=}\; 32\% \\ {}^{75}\text{As:} \quad 830\,\text{mT} &\;\hat{=}\; 24\% \end{aligned}$$

The polarization is calculated by comparing the experimental values with the theoretical values for a 15 nm quantum well calculated in section 4.1.2.

For smaller quantum wells the maximum field cannot be measured with this setup. The maximum field is close to or even larger than the maximum magnetic field produced externally. Since the displaced Hanle curves are very broad in the small wells, the maximum of the Hanle curve cannot be identified unambiguously.

However, it is possible to measure the sign of the effective g-value, $g^\star$. If the sign changes from one quantum well to another, the Hanle curve shifts to the opposite direction. This effect can be seen for the 6.8 nm quantum well, indicating that $g^\star > 0$ and emphasizes the argument from section 4.3.1 that the effective g-values in these samples are different from those reported previously[48].

4.4 Summary

In this chapter, the principles of the coupling of the electron and nuclear spin system and their experimental appearance are presented.

The hyperfine coupling constant, governing the electron-nuclear interaction, is derived for quantum wells of various thicknesses. It is pointed out, that the coupling can be described as magnetic fields of nuclear and electron origin. The subsequent calculation of the nuclear magnetic field acting on the electrons shows significant well width dependence and reaches values of over 20 T in a 5 nm wide well. It is shown, that nuclei situated in the barrier do not contribute noticeably to the ODNMR signal, due to the small penetration depth of the electron wavefunction into the barrier. The effective electronic magnetic field on the nuclei is calculated for a 20 nm wide quantum well and is at a maximum on the order of micro tesla.

Trapping of excitons at interface defects is assumed to play the key role in amplifying the hyperfine interaction compared to the interaction with delocalized electrons. A model is presented, to approximate the effect on the hyperfine

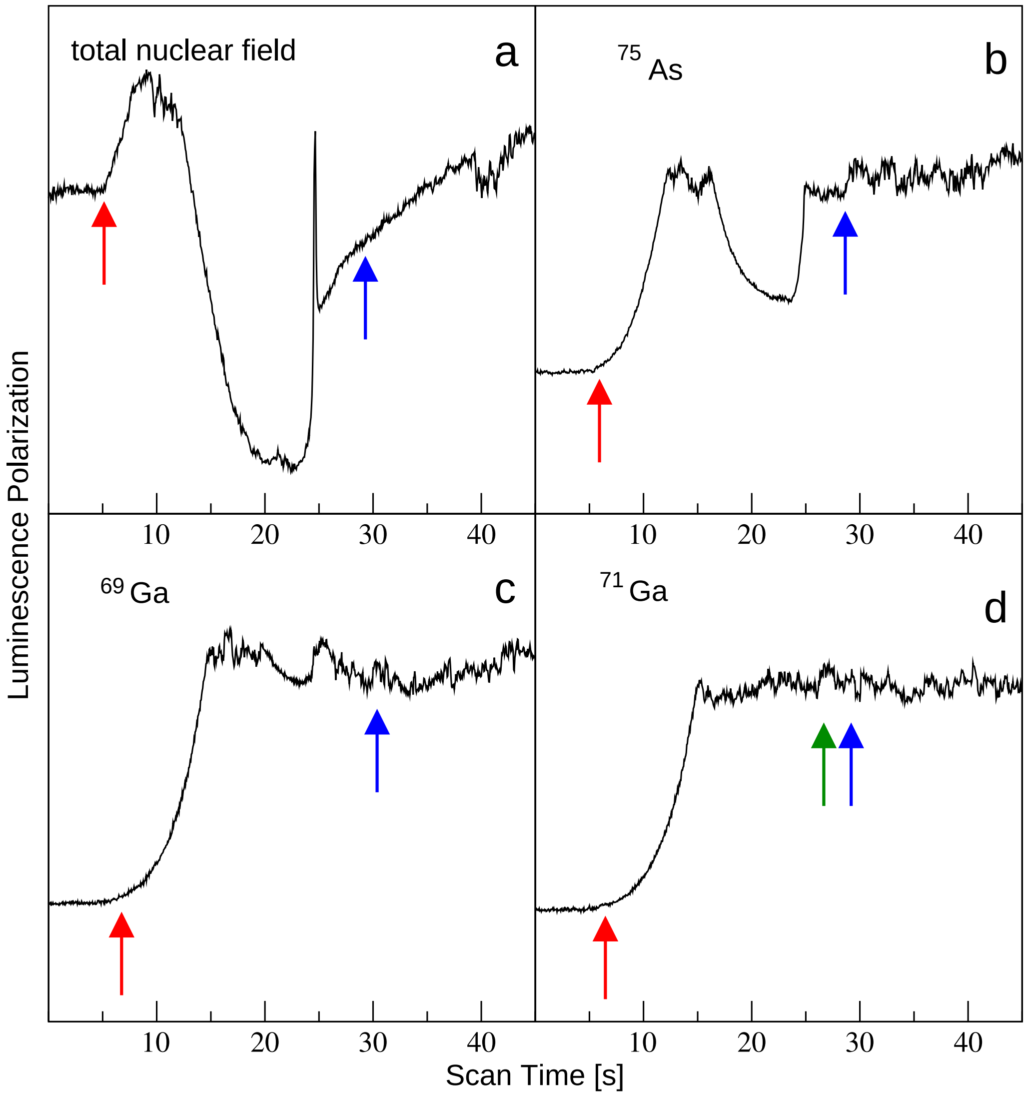

Figure 4.14: Rapid field scans to measure the maximum nuclear magnetic field of all three isotopes together (a) and separately (b)-(d) in the 14.5 nm well of sample $\#1431$. For the separate measurements, the two other isotopes are saturated. The field scan from 1.292 T to -0.011 T over the 40 s of scan time is not linear. The start at 1.292 T of the scan is indicated by the red arrows; the end at -0.011 T by the blue arrows. The zero field peak can be clearly observed in pictures (a)-(c). For ^{71}Ga, zero field is indicated by the green arrow.

relaxation time T_{1e}, and it is found, that the relaxation time is decreased by one to two orders of magnitude compared to unbound excitons. Therefore, optical pumping becomes more efficient than other relaxation processes, and eventually, a nuclear polarization can build up.

The dependence of the luminescence polarization on both the external and nuclear magnetic fields, the so called Hanle effect, is derived. This dependence enables optical detection of nuclear magnetic resonance. Hanle curves for different well widths are shown, and temperature and laser intensity influences are discussed.

The maximum nuclear magnetic field is obtained separately for each isotope by measuring the shift of the Hanle curves. The dependence of the nuclear field on the pumping field applied externally, reveals new information about the hyperfine coupling mechanisms of the electron-nuclear spin system. Within some range of external magnetic field strengths, the nuclear field tries to cancel out the the external field, creating nearly a zero effective field felt by the electrons. This behavior is observed as locking of the top of the Hanle curve to the externally applied field during a field scan.

Chapter 5

Nuclear Magnetic Resonance

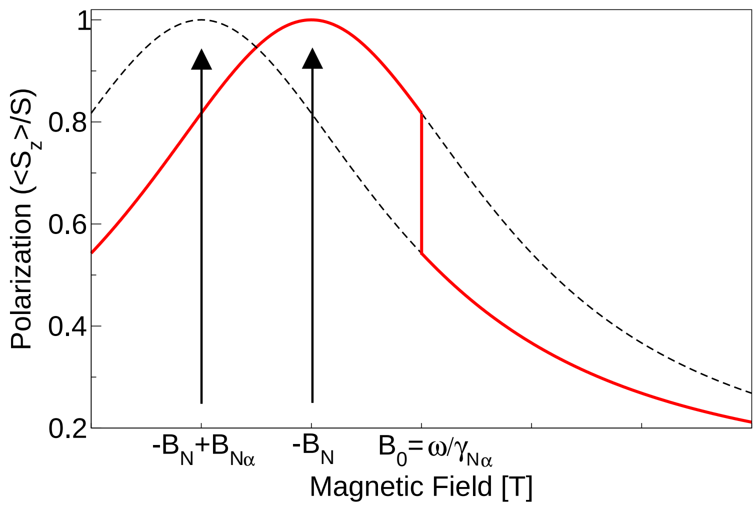

Figure 5.1: Model of the optical NMR signal

5.1 Introduction

In NMR the nuclear system is perturbed by applying a radio frequency field, ω_1 perpendicular to the external field that alters the populations of the nuclear energy levels if the RF field is of sufficient strength. The changes of nuclear polarization are, in principle, detected by changes in the inductance of the RF coil. In this chapter the observation of the NMR signal by optical means (ODNMR) will be explained. In this experiment, the RF coil is the only source for the radio frequency field, whereas the signal is detected optically by observation of the photoluminescence polarization.

It has been shown in chapter 4 that the optical signal strongly depends on the magnetic field that is either applied externally or created by the nuclei via the hyperfine interaction. By measuring the position of the displaced Hanle curve, it is possible to obtain an approximation of the nuclear polarization for each isotope. Changes of the polarization under NMR conditions therefore can be directly measured by observation of the luminescence polarization. If one of the isotopes is resonant with the applied RF field, the associated nuclear field decreases which shifts the Hanle curve to lower field values. This effect can be observed by a sharp change of polarization, as depicted in figure 5.1. The figure shows the signal for a scan of the external field while applying a constant RF field with the frequency $\omega = \gamma_{N\alpha} B_0$. The red line represents the detected signal. As long as the field is less than B_0, the displaced Hanle curve is measured with its maximum at $B = -B_N$, the total nuclear field. If the external field meets the resonance condition of isotope α, the associated nuclear field is destroyed, and the maximum of the Hanle curve is shifted to $B = -(B_N - B_{N\alpha})$. Therefore, the nuclear resonance becomes observable in the sharp decrease of the luminescence polarization at $B = B_{res}$.

In the experiments throughout this work, the magnetic field is usually kept constant, and the radio frequency is swept through the resonance. This does not change the principle of the detection but modifies the signal to some extent. Since the field is constant, one only detects a particular portion of the Hanle curve. At resonance, the Hanle curve is shifted to lower field values, and the change of the nuclear polarization again becomes observable in the sharp decrease of the luminescence polarization.

In conventional (dark) NMR experiments the change of the nuclear magnetization with respect to the frequency is measured, which leads to the typical spectra with peaks at the resonance. Instead in this ODNMR experiment, the nuclear magnetization is measured directly. Hence, the observed signal is obviously a convolution of the Hanle curve with the integrated "conventional" NMR spectrum. The fit routine and simulation discussed in the subsequent sections are based on this fact and give good results in obtaining details from the spectra.

Section 5.2 discusses the main features of the ODNMR spectra and the fitting and simulation routine. The time evolution of the pumping process and the relaxation of the nuclei are discussed in section 5.3. Finally, section 5.4 explains a slightly different ODNMR experiment by adiabatic fast passage.

5.2 Resonance Spectra

A typical ODNMR spectrum is depicted in figure 5.2 wherein the RF is swept from low to high frequencies. The spectrum is taken from the 19.7 nm wide quantum well and clearly reveals many characteristics of an ODNMR signal. Resonances of all three host lattice constituents of the quantum well occur at frequencies of 4.36 MHz, 6.12 MHz and 7.78 MHz for ^{75}As, ^{69}Ga and ^{71}Ga, respectively, in an external field of 600 mT. Evidence for the occurrence of an ^{27}Al signal has not been observed in any quantum well sample, which supports the results of the calculation of the penetration of the electron wavefunction from section 4.1.2. Therefore, it appears that the ODNMR signal stems solely from the 19.7 nm quantum well, and the wavefunction of the electron penetrates the barrier only to a very small amount.

The spectrum in figure 5.2 is a single scan experiment demonstrating the excellent signal-to-noise ratio of the optical method. The high noise level before the first resonance is due to the unstable electron-nuclear system as described in section 4.3.2. After each resonance, the luminescence polarization rises indicating the continuous optical pumping of the nuclear system. As the nuclear field builds

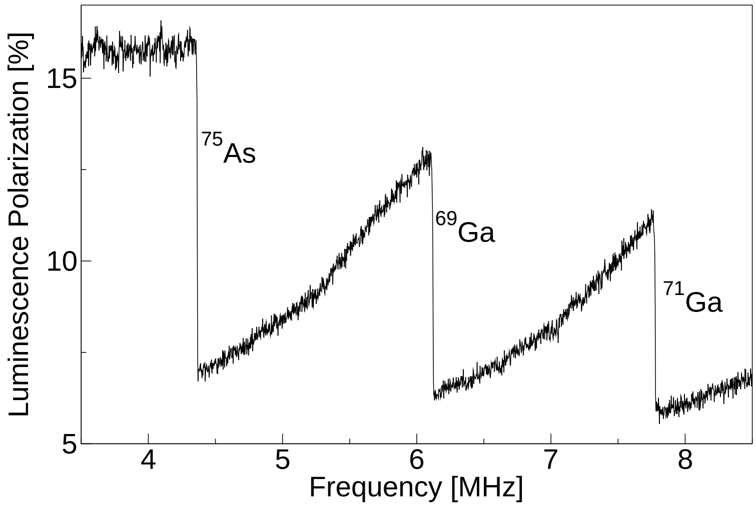

Figure 5.2: ODNMR spectrum of the 19.7 nm quantum well. The single scan was done with a rate of 100 kHz/s in an external field of 600 mT. The maximum polarization of the electrons is about 10% with an offset from the laser of about 5%.

up again, the Hanle curve is shifted to its prior position. The pumping rate of the nuclear system is slow relative to the timescale of the RF scan, that causes the resonance line intensities to decrease. Note that the optical signal decreases in overall intensity later in the scan (i.e, at higher frequencies), since the detection of $^{69/71}$Ga takes place in the wing of the Hanle curve.

In the rising polarization signal after the ^{75}As and ^{69}Ga resonances, a kink can clearly be observed. This feature indicates that the pumping process becomes more efficient at a critical value for the nuclear field, and the relaxation rate of the hyperfine interaction changes. These facts are consistent with the observation of the dragging of the Hanle curve with the scanned external field, shown in figure 4.14, which also terminates if the external field reaches a critical value.

The resolution of the spectrum is too low to find an accurate result for the line widths. A higher resolution is achieved in the spectra of figure 5.3 in which the frequency scan range has been reduced. The NMR signal of each isotope is recorded separately by single shot experiments during a scan time of 20 s. In order to interpret the data, a phenomenological fit function is used that deconvolutes the NMR signal and the Hanle curve. For the NMR signal, Gaussian and Lorentzian line fits have been tried out, where only the Gaussian gives satisfying results. The optical signal is calculated by integrating the Gaussian resonance line, that is, the error function, thereby revealing the nuclear polarization.

The optical pumping is taken into account as a relaxation process with a specific time constant. For the fit, we make the approximation that the optical

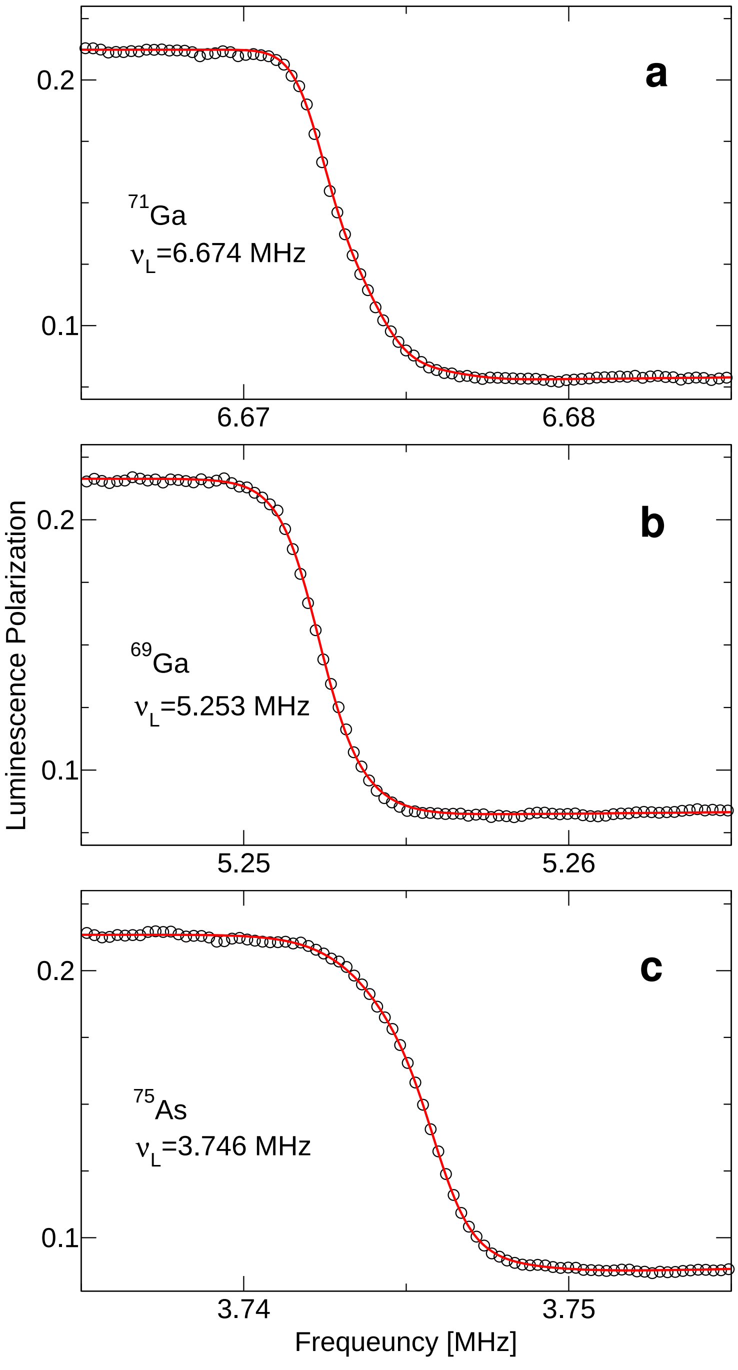

Figure 5.3: Resonance lines of all three isotopes in the 19.7 nm quantum well. The scan rate is 3 kHz/s in a 516 mT field. Circles denote the data; red lines denote the fit. The lines are fitted with the assumption of quadrupole splitting which cannot be resolved but is likely the reason for the broadening. a: ^{71}Ga, $\Delta\nu = 2.3$ kHz (HWHM), b: ^{69}Ga, $\Delta\nu = 1.8$ kHz (HWHM), c: ^{75}As, $\Delta\nu = 2.1$ kHz (HWHM)

	central line $\Delta\nu_c$ [kHz]	satellite line $\Delta\nu_s$ [kHz]	quadrupole splitting $\Delta\nu_q$ [kHz]
Scan up (5.4a)	0.7	3.5	33.4
Scan down (5.4b)	0.8	3.9	34.6

Table 5.1: Results from the fitting of the spectra shown in figure 5.4. The linewidths $\Delta\nu_c$ and $\Delta\nu_s$ are HWHM values.

pumping starts after passing half of the resonance, which partially takes into account the fact that the resonance lines are inhomogeneously broadened. This approximation certainly simplifies the real situation to some extent, but provides a sufficient parameter for the fit routine. The value for this artificially included relaxation time is by no means a measurable time and will not be stated in this work.

As will be pointed out in chapter 6, quadrupole interactions are very important for the ODNMR spectra in GaAs quantum wells. Therefore, the fit routine includes quadrupole splitting, $\Delta\nu_q$, of the resonance lines. In order to get a satisfying fit result for the spectra in figure 5.3, quadrupole splitting is assumed to be present. The line widths obtained range from 1.8 kHz to 2.3 kHz (HWHM), which are comparable to other results reported in publications using different experimental techniques [66] [23]. Nevertheless, it has to be noted that the lines are broadened by unresolved quadrupole splitting.

In case of larger quadrupole splitting, the lines are separated and can be easily resolved as in the spectra of figure 5.4. The figure shows resonance lines of ^{75}As from the 19.7 nm quantum well obtained by scanning the RF from low to high values (figure 5.4a) and vice versa (figure 5.4b). Note the excellent match of the phenomenological fit with the data. The linewidths as a result of the fit are given in table 5.1 for the two scan directions. The differences of the values between the two scans are presumably due to the uncertainty of the fit, rather than being an effect of reversing the scan direction.

The reasons for the broadening of the satellite lines are discussed in chapter 6 and will therefore be neglected here. However, attention should be drawn to the intensities of the resonance lines. Since the widths of the lines are not equal, one must compare the integrated intensities of the resonance lines (see labels in figures 5.4c and 5.4d). For the scan in figure 5.4c, the intensities of the resonance lines increase linearly with the increasing radio frequency. The intensity distribution is also linear but reversed for the scan from high to low frequency values. This experimental result shows a contradiction to the intensity distribution in the common literature of quadrupolar nuclei, where the quadrupole satellite lines each should have $3/4$ of the central line intensity [67].

In order to explain this behavior, the spectra are simulated numerically. As

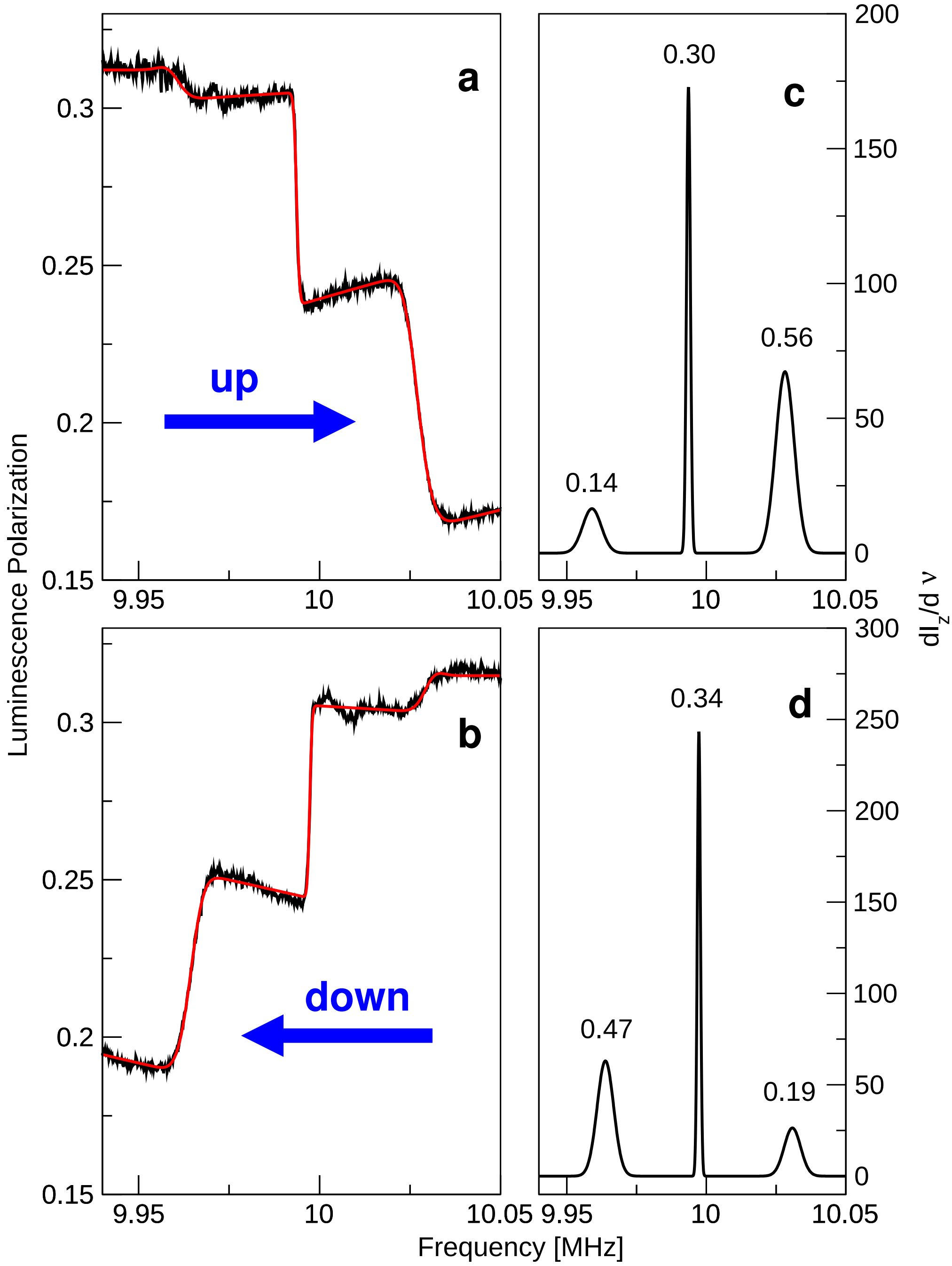

Figure 5.4: ODNMR spectra of ^{75}As from the 19.7 nm quantum well (a and b) and the calculated NMR spectra from the fit (c and d). The red lines in a and b overlaying the spectra are the fits. The direction of the RF scan is reversed from figure a to b, revealing the effect of population transfer to subsequent energy levels during the scan. The scan rate is 5 kHz/s. The numbers in figure c and d above the peaks denote the integrated intensity of each resonance line.

already pointed out, the resonance lines observed by ODNMR are a complicated convolution of both optical and NMR phenomena. Therefore, simulation of the spectra involves calculation of the time evolution of the nuclear system under the resonance condition and calculating the resulting Hanle curve for each time step.

5.2.1 Simulation of NMR Spectra

Time Evolution of the Nuclear Spin System

As already pointed out in section 4.2.1, one feasible description of the time evolution of a spin system utilizes density matrix formalism. The main contribution to the Hamiltonian, $\mathcal{H}$, is basically the Zeeman interaction. Thus, the z-axis of the system is chosen to be parallel to the external field, and the Hamiltonian is diagonal [41].

$$\mathcal{H}_Z = -\omega_0 \hbar I_z \tag{5.1}$$

In chapter 6 the interaction of the nuclear quadrupole moment with an electric field gradient at the site of the nuclei due to external and internal strain will be discussed in detail. The quadrupole interaction in both cases is very small compared to the Zeeman energy and therefore can be treated as a perturbation. At this point, only a constant field gradient with axial symmetry is considered, and the quadrupole interaction is the same for all nuclei of one isotope.

$$\mathcal{H}_Q = \omega_Q \hbar I_z^2 \tag{5.2}$$

Note that ω_Q is proportional to the shift of a single energy level of the nuclei, thence the resonance line is shifted by $\Delta\omega \sim 2\omega_Q$. The radio frequency field, ω_1, rotating with the frequency, ω, is applied in the x-direction and can also be treated as a perturbation to the Zeeman interaction.

$$\mathcal{H}_{RF} = -\frac{1}{2}\omega_1 \hbar (e^{i\omega t} + e^{-i\omega t}) I_x \tag{5.3}$$

All three isotopes, ^{69}Ga, ^{71}Ga, and ^{75}As have spin $I = \frac{3}{2}$; therefore, ρ is a 4×4-matrix in all three cases. The time evolution is calculated with the Von Neumann equation which leads to the following differential equation:

$$\dot{\rho} = -\frac{i}{\hbar}[\mathcal{H}_Z, \rho] - \frac{i}{\hbar}[\mathcal{H}_Q, \rho] - \frac{i}{\hbar}[\mathcal{H}_{RF}, \rho] \tag{5.4}$$

The interaction with the electron system will be neglected at this point and later included as a relaxation process. Utilizing equations 5.1 to 5.4, the differential equation for each component of the density matrix becomes

$$\begin{aligned} \dot{\rho}_{kl} \quad = \quad & \left(i\omega_0(I_z^{kk} - I_z^{ll}) - i\omega_Q[(I_z^{kk})^2 - (I_z^{ll})^2]\right)\rho_{kl} \\ & + i\tfrac{\omega_1}{2}(e^{i\omega t} + e^{-i\omega t})\textstyle\sum_m (I_x^{km}\rho_{ml} - \rho_{km} I_x^{ml}) \end{aligned} \tag{5.5}$$

The indices k, l, m go from 1 to 4, indicating the four spin states of the nuclei $(\frac{3}{2}, \frac{1}{2}, -\frac{1}{2}, -\frac{3}{2})$. For the density matrix the relation $\rho_{kl} = \rho^{\star}_{lk}$ holds, which means that only the upper diagonal matrix has to be calculated.

For this set of equations, the last term on the right-hand side is time dependent which makes it cumbersome to solve. Thus, the equations 5.5 are transformed from the laboratory frame into the frame rotating with the frequency, ω, around the z-axis. In addition to the transformation, the rotating frame approximation (RFA) is used. The components of the density matrix are separated into a slowly-varying part, ρ^{RFA}, and an oscillating part and can be written for a single spin:

$$\begin{array}{rcl} \rho_{kk} & = & \rho^{RFA}_{kk} \\ \rho_{kl} & = & \rho^{RFA}_{kl} e^{i|k-l|\omega t} \end{array} \tag{5.6}$$

Inserting equation 5.6 into 5.5 leads to terms which are rotating with the reference frame and are therefore time independent. Other terms are oscillating with 2ω and are neglected in the rotating frame approximation. The diagonal elements of the density matrix are real; the complex off-diagonal elements are divided into their real and imaginary parts, $\rho^{RFA}_{kl} = x_{kl} + iy_{kl}$. This leads to a set of 16 differential equations in which the radio frequency detuning, $\Delta = \omega_0 - \omega$, is introduced.

$$\begin{array}{rccl}
\dot{x}_{11} & = & & \frac{\omega_1}{2}\sqrt{3}y_{12} \\
\dot{x}_{22} & = & & -\frac{\omega_1}{2}(\sqrt{3}y_{12} - 2y_{33}) \\
\dot{x}_{33} & = & & -\frac{\omega_1}{2}(2y_{33} - \sqrt{3}y_{34}) \\
\dot{x}_{44} & = & & -\frac{\omega_1}{2}\sqrt{3}y_{34} \\
\dot{x}_{12} & = & -(\Delta - 2\omega_Q)y_{12} & +\frac{\omega_1}{2}y_{13} \\
\dot{y}_{12} & = & (\Delta - 2\omega_Q)x_{12} & +\frac{\omega_1}{4}(\sqrt{3}x_{22} - \sqrt{3}x_{11} - 2x_{13}) \\
\dot{x}_{13} & = & -(2\Delta - 2\omega_Q)y_{13} & -\frac{\omega_1}{4}(-2y_{12} - \sqrt{3}y_{14} + \sqrt{3}y_{23}) \\
\dot{y}_{13} & = & (2\Delta - 2\omega_Q)x_{13} & +\frac{\omega_1}{4}(-2x_{12} - \sqrt{3}x_{14} + \sqrt{3}x_{23}) \\
\dot{x}_{14} & = & -3\Delta y_{14} & -\frac{\omega_1}{4}(-\sqrt{3}y_{13} + \sqrt{3}y_{24}) \\
\dot{y}_{14} & = & 3\Delta x_{14} & +\frac{\omega_1}{4}(-\sqrt{3}x_{13} + \sqrt{3}x_{24}) \\
\dot{x}_{23} & = & -\Delta y_{23} & -\frac{\omega_1}{4}(\sqrt{3}y_{13} - \sqrt{3}y_{24}) \\
\dot{y}_{23} & = & \Delta x_{23} & +\frac{\omega_1}{4}(\sqrt{3}y_{13} + 2x_{33} - 2x_{22} - \sqrt{3}y_{24}) \\
\dot{x}_{24} & = & -(2\Delta + 2\omega_Q)y_{24} & -\frac{\omega_1}{4}(-\sqrt{3}y_{23} + \sqrt{3}y_{14} + 2y_{34}) \\
\dot{y}_{24} & = & (2\Delta + 2\omega_Q)x_{24} & +\frac{\omega_1}{4}(-\sqrt{3}x_{23} + \sqrt{3}x_{14} + 2x_{34}) \\
\dot{x}_{34} & = & -(\Delta + 2\omega_Q)y_{34} & -\frac{\omega_1}{2}y_{24} \\
\dot{y}_{34} & = & (\Delta + 2\omega_Q)x_{34} & +\frac{\omega_1}{4}(\sqrt{3}x_{44} + 2x_{24} - \sqrt{3}x_{33})
\end{array} \tag{5.7}$$

So far, no relaxation processes have been taken into account which will be made up in a phenomenological way. Only spin lattice relaxation that connects neighboring states, will be considered here. Since the relaxation into thermal equilibrium plays only a minor role compared to the optical pumping during the RF scan, all other relaxation processes, such as quadrupole relaxation, will be neglected. Longitudinal relaxation in the simplest case occurs with the rate, Γ_1, between neighboring diagonal matrix elements. Since the thermal equilibrium polarization at 4 K can be neglected, longitudinal relaxation basically equalizes the populations in the four spin states. The differential equations for the diagonal elements change to:

$$\begin{array}{lll} \dot{x}_{11} & \rightarrow & \dot{x}_{11} - \frac{1}{2}(x_{11} - x_{22})\Gamma_1 \\ \dot{x}_{22} & \rightarrow & \dot{x}_{22} - \frac{1}{2}(2x_{22} - x_{11} - x_{33})\Gamma_1 \\ \dot{x}_{33} & \rightarrow & \dot{x}_{33} - \frac{1}{2}(2x_{33} - x_{22} - x_{44})\Gamma_1 \\ \dot{x}_{44} & \rightarrow & \dot{x}_{44} - \frac{1}{2}(x_{44} - x_{33})\Gamma_1 \end{array} \tag{5.8}$$

The coherence terms decay on a shorter time scale with a rate, Γ_2. This rate determines the linewidth of the resonance lines. As will be shown later, the line widths for the central and the two satellite transitions are not equal. The reasons for the broadening of the satellite lines will be discussed in chapter 6. Since the relaxation is equal for the real and imaginary parts of each matrix element, ρ_{kl}, is used in the differential equations. The off-diagonal elements vanish in thermal equilibrium giving the following set of equations:

$$\dot{\rho}_{kl}^{RFA} \rightarrow \dot{\rho}_{kl}^{RFA} - \Gamma_2 \rho_{kl}^{RFA} \qquad \text{for} \qquad k \neq l \tag{5.9}$$

At this point, the different line widths can in principle be modeled by different relaxation rates for the central and the satellite transitions. In this case, Γ_2 has to be replaced by Γ_2^{sat} for the satellite transitions $1 \rightarrow 2$ and $3 \rightarrow 4$.

Optical Pumping and Detection

As already pointed out in section 4.1.4, one possible way to understand the coupling of the electron and nuclear systems is cooling of the nuclear spins by the electron spin bath, applying the concept of spin temperature. According to this concept, the probabilities of finding the system in any of its energy levels are given by a Boltzmann distribution which defines the spin temperature, T_S. The number of spins in each state is defined by $\langle N_j \rangle = \frac{N}{Z} e^{-E_j/k_B T_S}$ with the partition function, $Z = \sum_j e^{-E_j/k_B T_S}$, and k_B being the Boltzmann constant. For normalized populations ($\sum_j N_j = 1$), N_j are the matrix elements of the density matrix in "thermal" equilibrium. The spin temperature for the degrees of polarization at normal experimental frequencies (about 10 MHz) is on the order of 10^{-3} K, where the high temperature approximation applies. The population distribution of the four spin states of the $I = 3/2$ spin system is therefore linear and can easily be calculated for each degree of polarization in the simulation.

The polarization is defined by $P = \left|\frac{\langle I_z \rangle}{I}\right|$ from which the spin temperature can be calculated. Using the relation $\langle I_z \rangle = \text{Tr}\{I_z \rho\}$ the polarization is

$$P = \frac{10}{3} \frac{\hbar\omega_0}{[4k_B T_S - \hbar(6\omega_0 - 4\omega_Q)]} \tag{5.10}$$

Equation 5.10 can be solved for an arbitrary degree of polarization which in turn reveals the populations.

With the concept of spin temperature and the equilibrium values, x_{kk_0}, optical pumping can be described as a longitudinal relaxation process with a rate, Γ_{1e}. This modifies only the differential equations of the diagonal elements of the density matrix which become:

$$\begin{array}{lcl} \dot{x}_{11} & \rightarrow & \dot{x}_{11} - (x_{11} - x_{11_0})\Gamma_{1e} \\ \dot{x}_{22} & \rightarrow & \dot{x}_{22} - (x_{22} - x_{22_0})\Gamma_{1e} \\ \dot{x}_{33} & \rightarrow & \dot{x}_{33} - (x_{33} - x_{33_0})\Gamma_{1e} \\ \dot{x}_{44} & \rightarrow & \dot{x}_{44} - (x_{44} - x_{44_0})\Gamma_{1e} \end{array} \tag{5.11}$$

In the ODNMR experiment the radio frequency, ω, is scanned over the resonances making the detuning, Δ, in equations 5.7 time dependent. For simulations of the spectra, the differential equations together with the three relaxation terms, 5.8, 5.9 and 5.11, have to be numerically integrated. Hence, the average spin, $\langle I_z \rangle$, is calculated for each time step, giving a nuclear field, $B_N \sim \langle I_z \rangle$.

The optical signal is determined by the Hanle curve developed in section 4.2. Inserting B_N for each time step into equation 4.40 gives the value of the luminescence polarization for every moment during the ODNMR experiment. The simulations performed here neglect effects such as dipole-dipole coupling, quadrupole processes, Knight shift, etc. These effects should in principle be considered separately, but they do not change the intensity distribution of the resonance lines.

5.2.2 Results of Simulation

Some simulated spectra are shown in figure 5.5. The spectra are calculated without longitudinal relaxation nor optical pumping effects. For low RF fields ($\nu_1 = 0.01\,$kHz), (figure 5.5a) the intensity distribution of the peaks is 3:4:3 as claimed in the literature [67]. However, as the RF intensity increases, the intensities of the resonance lines change. If the RF power is sufficiently high, the NMR transitions are saturated, meaning that the population difference between each state is equalized. In a continuous wave experiment, scanning over the resonances transfers population from the lower energy state to the higher energy one, increasing the population difference in the next higher transition. Since the

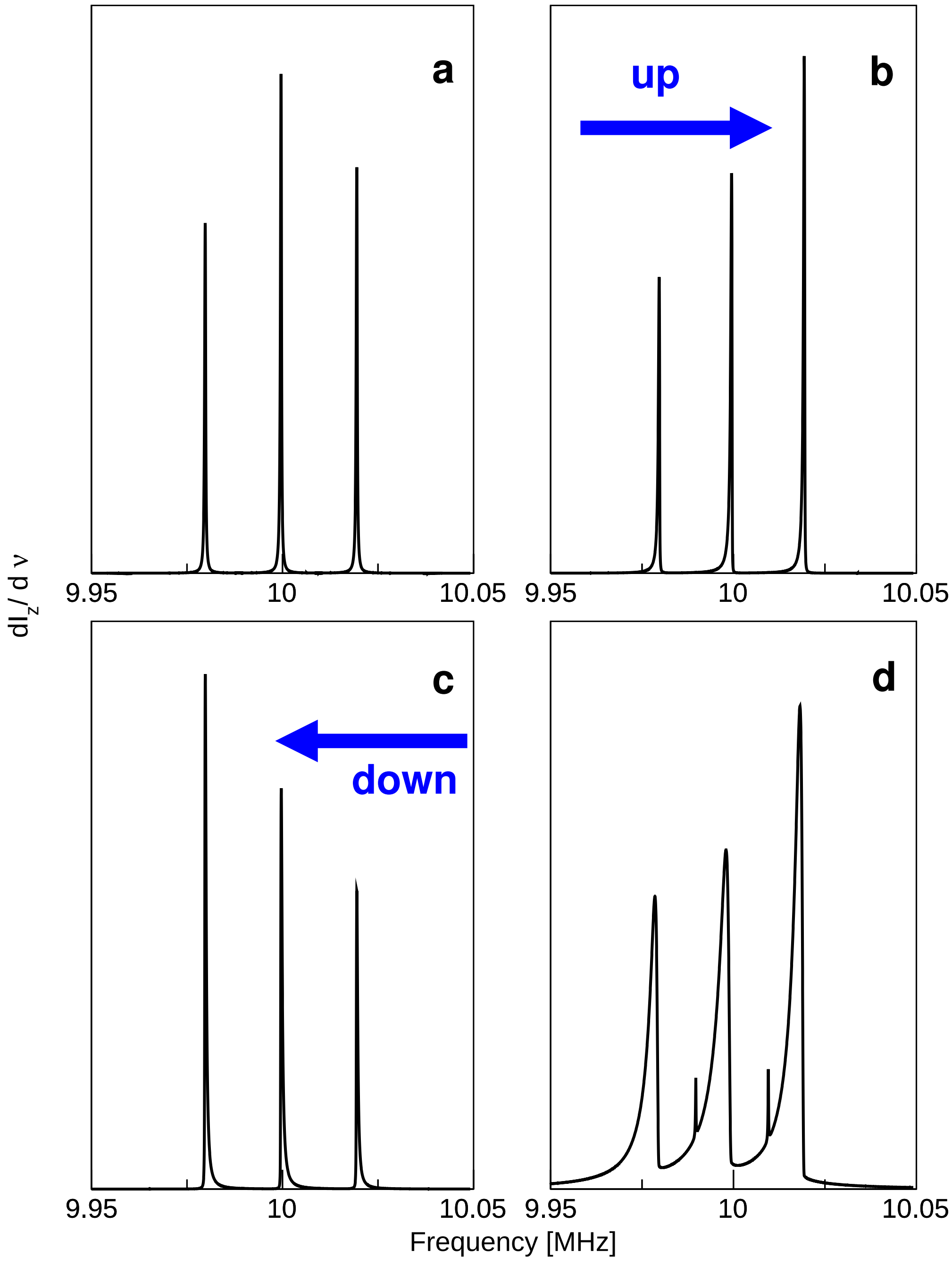

Figure 5.5: Calculated NMR spectra for different RF field strengths ($\nu_1 = \frac{\omega_1}{2\pi}$) with scan rate 25 kHz/s. a: $\nu_1 = 0.01$ kHz, b: $\nu_1 = 0.08$ kHz scan direction up, c: $\nu_1 = 0.08$ kHz scan direction down, d: $\nu_1 = 0.29$ kHz.

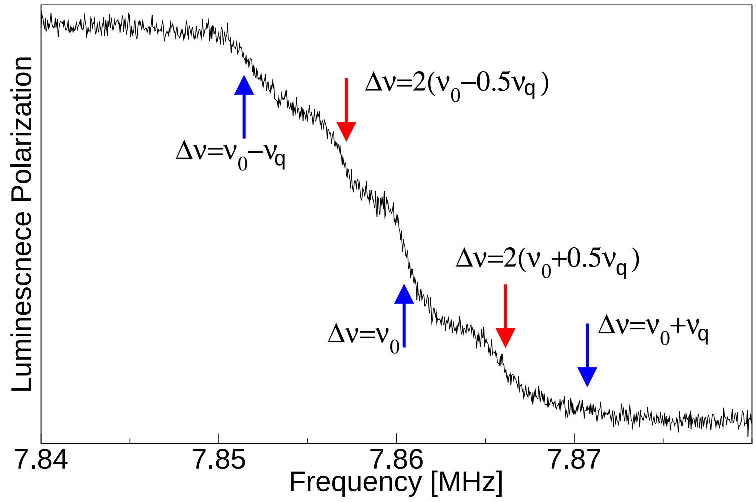

Figure 5.6: ODNMR spectrum of ^{75}As in the 19.7 nm well of sample $\#1056$. The scan rate is 5 kHz/s with an RF field of about $50\,\mu$T (i.e. $\nu_1 \sim 0.36$ kHz). The blue arrows denote single-quantum transitions; the red arrows denote two-quantum transitions, as explained in the text.

intensity of each resonance line is proportional to the population difference of its associated transition, the intensity increases for the high energy transitions in a scan from low to high frequency values. This effect can clearly be observed in figure 5.5b. If one reverses the scan direction, for linear population distributions one expects a reversed order of the intensities of the resonance lines which is shown by figure 5.5c.

Increase of the RF field, ω_1, does not only alter the intensities of the resonance lines but also permits multi-quantum transitions that appear as small lines to the left and right of the central line in figure 5.5d. They belong to the transitions $1 \rightarrow 3$ and $2 \rightarrow 4$ with the transition frequencies, $\Delta\nu = 2 \cdot (\nu_0 \pm \frac{1}{2}\nu_Q)$. These lines usually do not appear in the experimental spectra, but an example for the appearance of double quantum transitions can be seen in figure 5.6. The figure shows the ^{75}As spectrum in the 19.7 nm well of sample $\#1056$ applying an ω_1-field of about $50\,\mu$T (i.e. $\nu_1 \sim 0.36$ kHz). Between the two satellites and the central transition, two resonance lines appear. These resonances can be attributed to two-quantum transitions of ^{75}As. The simulation predicts the appearance of multi-quantum transitions at high RF fields, whereas the experiment shows these transitions already at low intensities. This fact might be explained by J. Winter [68], who analyzed the selection rules and showed that if the RF field, ω_1, has a component parallel to the external field, two quantum transitions can appear. This presumably is the case for the RF field due to the split solenoid RF coil

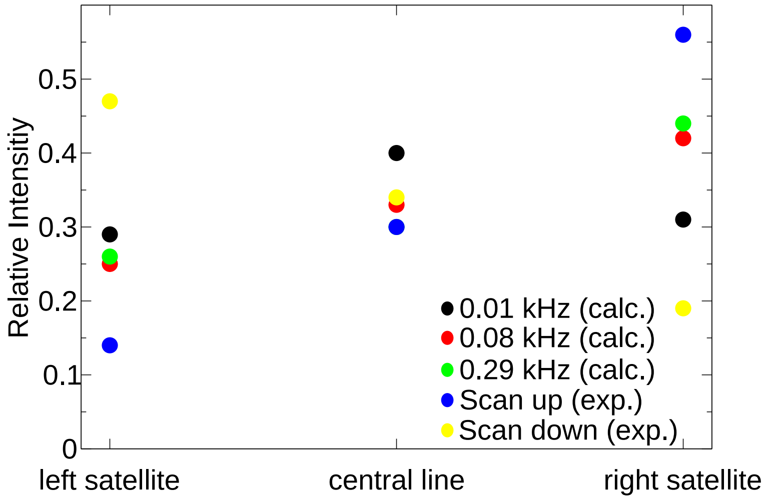

Figure 5.7: Normalized line intensities of calculated and measured ODNMR-spectra. The RF field in the simulation is measured in frequency units. The experimental data is taken from figure 5.4, the simulated data are shown in figure 5.5. The data point of 0.29 kHz (green) and the scan up (blue) overlap for the central transition.

configuration of this experiment.

Even if the intensities of these multi-quantum transitions are comparatively small (as in figure 5.5d), and therefore do not appear in other ODNMR signals, it is worth noting that their influence on the populations and therefore on the intensities of the single-quantum transitions might be sufficiently high to make quantitative analysis of these line intensities difficult.

Figure 5.7 shows the normalized intensities of the spectra from figure 5.4 and 5.5. The graph shows that the slopes and relative intensities of the experimental data from the two different scans are not equal, indicating that the population distribution is not linear and therefore cannot be described by a Boltzmann distribution. This is another indication that the proposed theory by D'yakonov with the spin temperature concept does not apply in the case of the system under investigation of this thesis.

5.3 Relaxation Times

Several relaxation processes take place in the nuclear spin system and influence the ODNMR signal. Basically, they can be divided into two groups: the relaxation due to optically oriented electrons, and the "dark" relaxation processes i.e. spin lattice relaxation. Both types of relaxation are investigated, and the results will

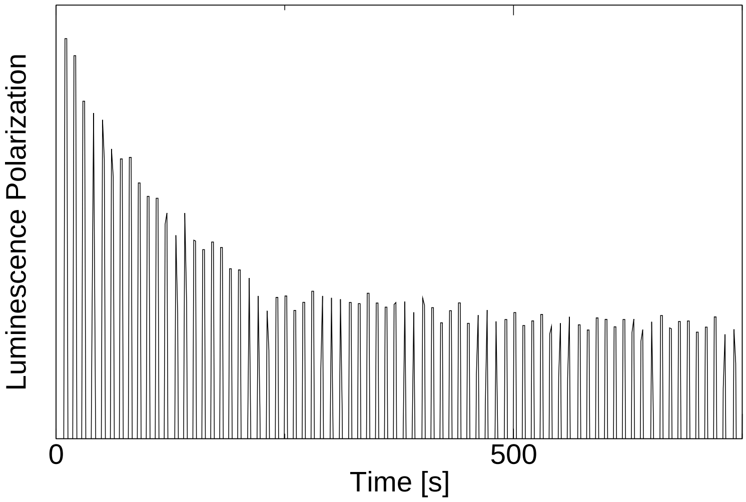

Figure 5.8: Stroboscopically measured luminescence polarization to obtain the "dark" relaxation time, T_1. The data shown belong to the relaxation of ^{75}As in an external field of 186 mT

be discussed in the subsequent sections.

5.3.1 "Dark" Relaxation

As indicated by the name, "dark" relaxation processes include all types of relaxation that occur without the influence of the optically oriented electrons, such as the relaxation of the optically pumped nuclear spin system after turning off the laser. The relaxation of each isotope is measured separately by pumping the nuclear system at a fixed external field and simultaneously saturating two of the three isotopes by RF scans over the resonances with two RF generators. After pumping the system for a sufficiently long time for the system to reach its steady state value, $B_{N\alpha}^{eq}$, the laser light is then blocked with a shutter. The laser is turned on for 0.2 s with a repetition rate of 0.1 Hz in order to measure the degree of luminescence polarization. Repeating this procedure for several minutes allows one to stroboscopically observe the Hanle curve moving to zero as the nuclear polarization relaxes. An example of such a signal is presented in figure 5.8. The influence of the light can be neglected during the short period when the shutter is open, since the hyperfine coupling constant is much larger (see next section), and therefore essentially no transfer of polarization does occur. The effect can be fitted by inserting the time dependent nuclear field

$$B_{N\alpha}(t) = B_{N\alpha}^{eq} e^{-\frac{t}{T_1}} \tag{5.12}$$

B_0	^{69}Ga	^{71}Ga	^{75}As
186 mT	300 s	340 s	185 s
250 mT	325 s	370 s	230 s

Table 5.2: "Dark" relaxation times (T_1) for all three isotopes measured for different external magnetic fields, B_0.

into equation 4.40. The resulting relaxation times for all three isotopes are listed in table 5.2. Over this relatively small range of magnetic fields, a weak increase of the relaxation time with the strength of the field is apparent.

These values are shorter than data published earlier ($T_1 = 10^3\,\mathrm{s} - 10^4\,\mathrm{s}$) [69] [70]. The difference may be due to spin diffusion: in the optically detected experiment, mainly nuclear spins within the Bohr radius of the localized excitons contribute to the signal. Spin diffusion distributes the nuclear polarization over a wider area, the size of which is determined by the diffusion constant and the relaxation to thermal equilibrium. Therefore, spin diffusion in ODNMR reduces the polarization of those nuclear spins that couple to the (localized) excitons and could reduce the relaxation time. The total nuclear spin polarization measured by conventional RF detection, however, is not affected by spin diffusion.

It is not possible to distinguish different relaxation processes; the separate contributions of the spin lattice relaxation and spin diffusion cannot be resolved. However, the relatively short values for T_1 in this particular case show that even with decent pumping efficiency, it can sometimes be difficult to create sufficient nuclear polarization. This is the case in the bulk substrate material of the samples, where there is minimal localization of excitons, and therefore, the losses due to "dark" relaxation are bigger than the relaxation due to optically oriented electrons.

5.3.2 Pumping Time

The buildup of the polarization proceeds with the pumping time, T_1^f. This time constant involves different relaxation processes such as hyperfine coupling with optically oriented electrons, spin diffusion, and dark relaxation. Unfortunately, these effects are complicated to measure separately, since the processes bringing the nuclear system into thermal equilibrium are present at any time.

To measure the pumping time, T_1^f, the transition of one isotope is saturated to destroy any polarization, and then the buildup of the polarization is observed. An example of this behavior is visible in Figure 5.2. Figure 5.9 summarizes the result for the ^{75}As nuclei.

The graph shows that at intermediate fields ($\sim 0.5\,\mathrm{T}$), the polarization is established within a few seconds, while the pumping time increases by an order

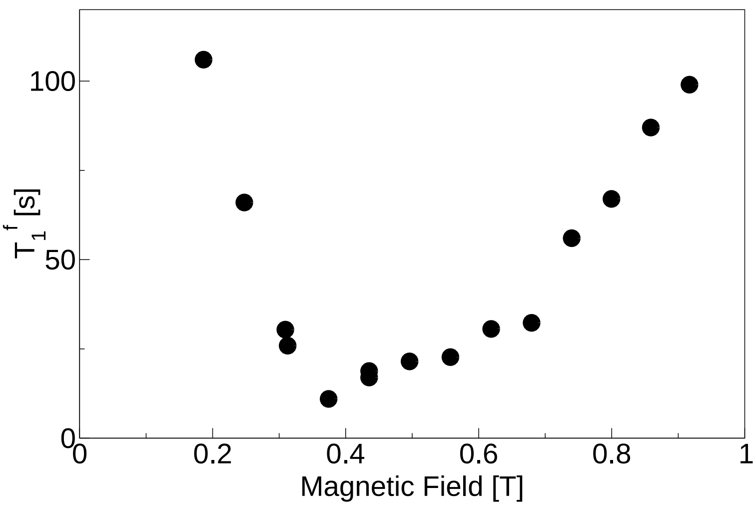

Figure 5.9: The dependence of the optical pumping time, T_1^f, of ^{75}As on the magnitude of the external field.

of magnitude at weak (< 0.3 T) and strong (> 0.8 T) fields. The hyperfine relaxation time, T_1^e, from equation 4.22 determined by D'yakonov [50] depends quadratically on the external field. This trend might apply to the data in figure 5.9 if one keeps in mind that T_1^f is composed of several field-dependent relaxation times. At intermediate fields, though, the pumping time remains in a very narrow range. The hyperfine relaxation time, T_1^e, has its minimum at zero effective field, making the hyperfine coupling most efficient at this point. This is another indication that the electron-nuclear spin system tries to establish a zero effective field for the electrons over a wide range of external fields. Below and above some critical external field value, this behavior of the system vanishes, and the D'yakonov rule for the relaxation time seems to hold.

While only saturating the ^{75}As polarization, it is found that the polarization of all three nuclear isotopes increased during the subsequent pumping period. This effect becomes apparent if one saturates the ^{75}As transition a second time, after the optical signal has reached its initial value. The second ODNMR spectrum has less intensity than the first one, indicating that the nuclear field of ^{75}As has not reached its steady state value. Therefore, the equilibrium polarization is determined by the total nuclear field rather than by an equilibration between individual nuclear spins with the electron spin.

Quantitative comparisons of the pumping times in the three different samples show that the pumping is most efficient in sample $\#1056$ and least efficient in sample $\#1294$. An example of an ODNMR spectrum of ^{75}As measured in the 19.7 nm quantum well of sample $\#1056$ is depicted in figure 5.10. Between

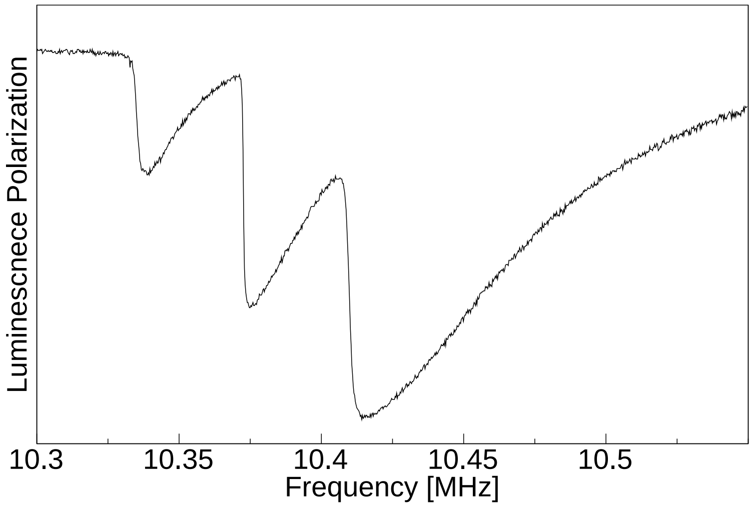

Figure 5.10: ODNMR spectrum of ^{75}As measured in the 19.7 nm quantum well of sample $\#1056$. The spectrum is taken with a scan rate of 5 kHz/s (the spectrum shows a scan lasting 50 s). The pumping time is on the order of 2 s.

each quadrupole splitted resonance line, the polarization is almost completely restored, indicating large hyperfine coupling and therefore, high localization of the electrons. This supports the theory that exciton trapping is the primary factor for the large hyperfine coupling. From PL spectra it can be seen that sample $\#1056$ has the most interface defects; therefore, excitons are trapped very easily, increasing the hyperfine interaction compared to the other samples. The PL spectra indicate that sample $\#1294$ has very smooth interfaces, which is reflected is reflected by the lower observed intensities in the ODNMR experiments. The interface roughness of sample $\#1431$ is in between the two others, shown by PL and ODNMR.

5.4 Adiabatic Rapid Passage

The continuous wave experiment described in the previous sections completely destroys the spin polarization of the measured isotope when the populations of the neighboring spin states are equalized. While the buildup of polarization under optical pumping is faster than through thermal polarization, the optical pumping time is still on the order of 10–100 s for field strengths used here, as shown above. It is therefore advantageous to detect the signal without destroying the nuclear spin polarization.

For this purpose, adiabatic rapid passage [51] is used to invert the nuclear spin polarization rather than saturate it. Therefore, the direction of the particular nuclear field changes from $-B_{N\alpha}$ to $B_{N\alpha}$. In ODNMR, this change becomes obvious in a rapid shift of the Hanle curve. The procedure is implemented by scanning the radio frequency over the resonance line while keeping the magnetic field fixed. Figure 5.11 shows an example of such an experiment carried out for the ^{69}Ga isotope; the radio frequency is scanned from $\nu_0 = 4.34$ MHz to $\nu_1 = 4.54$ MHz, thereby inverting the ^{69}Ga spins. Reversing the scan direction from ν_1 back to ν_0, the polarization of the luminescence reaches nearly its initial value, indicating that the loss of nuclear spin polarization was very small. For this experiment, the scan rate was 4 MHz/s. The figure displayed here represents an average over 60 scans, with delays of 2 s between scans to allow the polarization to be reestablished.

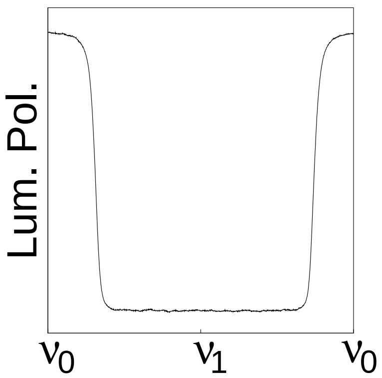

Figure 5.11: Adiabatic inversion of ^{69}Ga. The frequency is scanned from $\nu_0 = 4.34$ MHz to $\nu_1 = 4.54$ MHz and back to ν_0, thus, inverting the nuclear field twice.

The high efficiency of the adiabatic scanning is shown in figures 5.12 and 5.13, again for ^{69}Ga. For each adiabatic scan, the radio frequency was scanned from 3.57 MHz to 3.67 MHz and back with a scan rate of 300 kHz/s. The time constant of the detection is too slow compared to the scan rate; therefore, the experiment only measures the polarization between inversions of the nuclear magnetization. The data show "oscillations" rather than steps, as in figure 5.11, representing successive inversions of the ^{69}Ga nuclear field. The relative amplitude of each inversion and the absolute amplitude of the signal depend on the position of the Hanle curve and on the size of the inverted nuclear field. Small losses during each inversion cause shifts of the Hanle curve, altering the signal amplitude for subsequent inversions. However, the losses are compensated by the two other isotopes, ^{71}Ga and ^{75}As; therefore, the total nuclear magnetic field changes only slightly. The trace, for example, in figure 5.13 shows some 120 reversals of the spin polarization before most of the ^{69}Ga spin polarization is lost.

However, adiabatic inversion broadens the resonance lines due to the high RF field needed for the scan. This broadening reduces the resolution of the experiment, and fine structure such as small quadrupole splittings cannot be observed. Adiabatic inversion is carried for ^{69}Ga and ^{71}Ga (not shown), whereas the losses for inversion of the ^{75}As polarization are too large to reestablish the initial polarization.

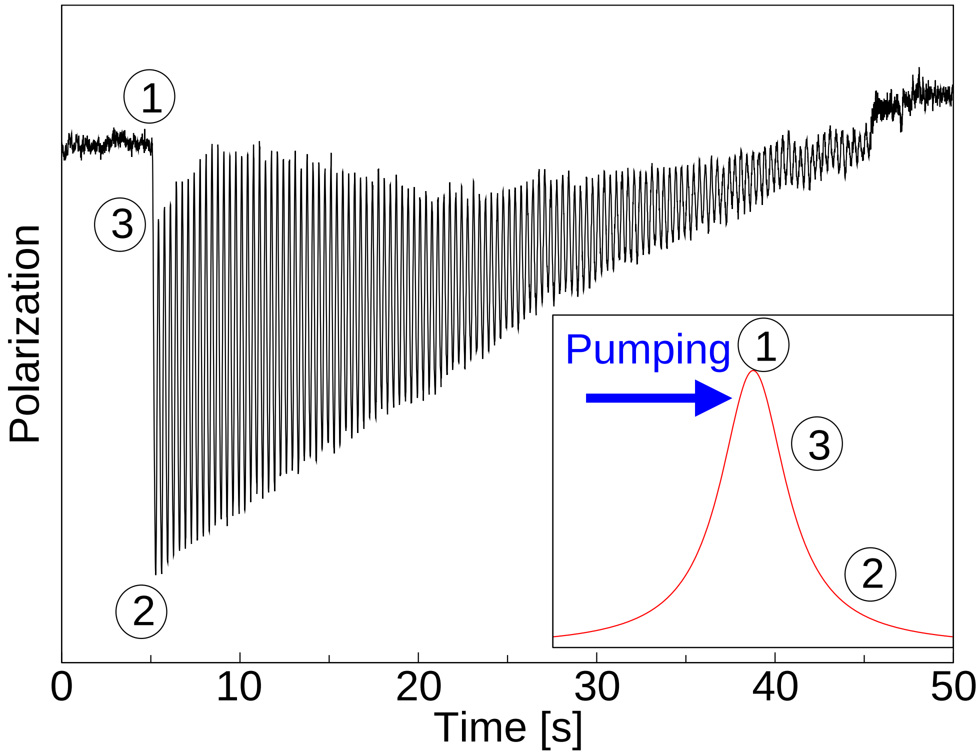

Figure 5.12: Polarization of the luminescence during successive adiabatic scans of the ^{69}Ga resonance. The scan was from 3.57 MHz to 3.67 MHz with a scan rate of 300 kHz/s. The inset shows an example of the Hanle curve. Before the adiabatic scan starts, the nuclear system has reached its equilibrium value; therefore, one detects the top of the Hanle curve, indicated by position 1. The first inversion of the nuclear field shifts the Hanle curve to the left; therefore, one detects position 2. The reverse of the scan shifts the Hanle curve back, but due to the losses, only position 3 is reached. The subsequent scans show further losses, which accumulate and reduce the relative amplitude. The absolute amplitude of the signal reaches its initial value, indicating that the other isotopes are pumped during the process.

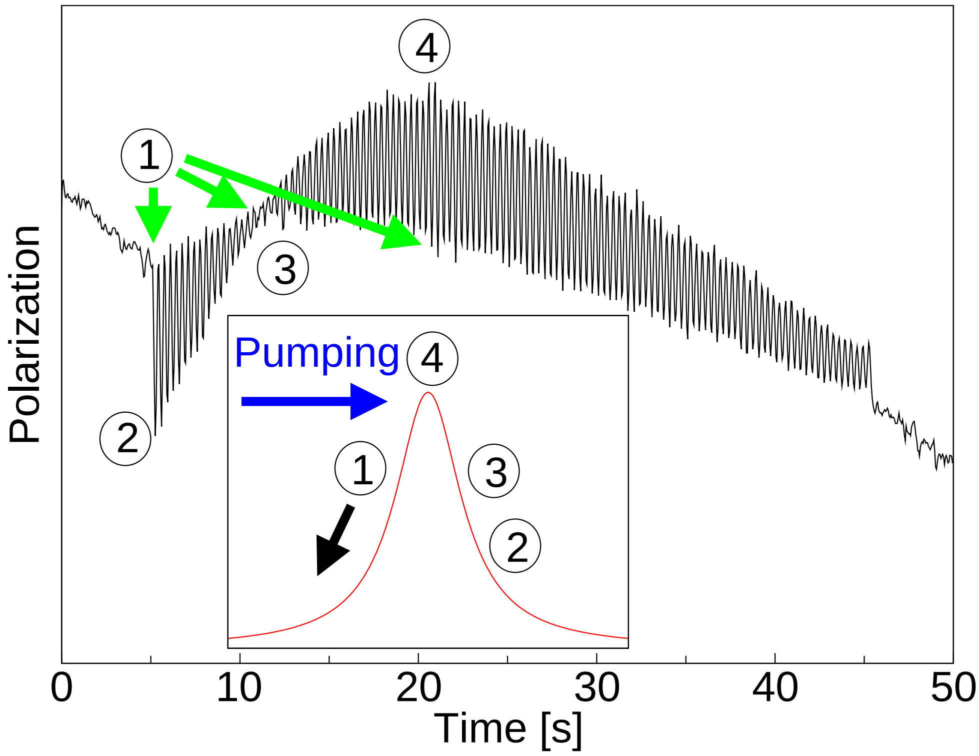

Figure 5.13: Successive adiabatic scans of the ^{69}Ga resonance with the same parameters as in figure 5.12. The system has in this case not reached its steady state, which is indicated by the decrease in the luminescence polarization before the scan. The position of the Hanle curve is on its left shoulder (1) initially. After the first inversion, the Hanle curve is shifted to the left changing the position on the curve to 2. However, the expected increase of the signal during the inversion by moving across the top of the Hanle curve cannot be observed due to the long time constant of the detection system. Reversing the scan direction brings the curve back to position 1. Due to losses, after several scans the signal is shifted between symmetrical points on both sides of the Hanle curve (1 and 3), thereby causing no change in the photoluminescence polarization since the levels are nearly equal. Persistent optical pumping of the two other isotopes eventually shifts the Hanle curve further to the right; therefore, the position moves up the shoulder of the Hanle curve. At position 4, the maximum of the Hanle curve is reached, giving the maximum signal in the figure. Successive losses of ^{69}Ga and optical pumping of ^{71}Ga and ^{75}As reduce the relative and absolute amplitude of the signal, respectively.

5.5 Summary

In this chapter, optically detected NMR spectra of GaAs/AlGaAs quantum wells are presented. The resonances are identified as belonging to the major components of the quantum well heterostructure. In agreement with the previously presented calculations, no evidence for signals from the barrier is observed. The resonance lines show large splittings which are attributed to quadrupole interactions with the perturbed nuclear system. Using a phenomenological fit function permits the ODNMR signal to be deconvoluted from the underlying NMR spectrum and reveals the widths and intensities of the resonance lines. The line widths are comparable to values published earlier using different NMR techniques, indicating that the ODNMR method does not influence them. However, the line intensities differ from the commonly accepted ones of quadrupole systems. Numerical simulation of the NMR spectra confirm this deviation from the common intensity distribution. Simulations also reveal, that the population distribution for the nuclei are different from a Boltzmann distribution. Therefore, the spin temperature concept proposed by D'yakonov does not apply in the systems under investigation. Two-quantum transitions are predicted by the simulation and are found experimentally, even at low RF field strengths.

Different relaxation times are measured. The field dependent relaxation times, T_1, obtained with the optical relaxation suppressed, reveal that spin diffusion plays an important role as a relaxation process. The pumping time, T_1^f, is measured in different magnetic fields, revealing almost no field dependence within some field range, in contrast to D'yakonov's theory.

Adiabatic inversion of the ^{69}Ga nuclear polarization and its influence on the ODNMR signal is shown. The trace of over 120 reversals of the nuclear field indicates that the two other isotopes tend to compensate the losses of the ^{69}Ga nuclei.

Chapter 6

Electric Quadrupole Effects

6.1 Introduction

So far only magnetic interactions of the nuclei with the external field and the electrons have been considered, whereas electric field couplings have been neglected. But due to the asymmetric charge distribution occurring within the nucleus, all nuclei with spin $I > \frac{1}{2}$ posses a nuclear quadrupole moment, Q. If the nucleus is at a site of lower than cubic symmetry, the quadrupole moment couples to the electric field gradients created by the surroundings.

Crystalline GaAs in general has cubic symmetry; therefore, no quadrupole interaction occurs at the site of the nucleus. However, in low-dimensional systems or heterostructures, the symmetry might be reduced by strain or dimensionality effects. The strain can be applied externally, or its source can be internal due to lattice mismatch of the different materials.

In the following sections the relationship between the quadrupole coupling and strain will be discussed. The influence of the two different sources of strain on the signal will be modeled and compared with experiment.

6.2 Quadrupole Splitting

The quadrupole interaction can be described by the nuclear quadrupole moment, Q, coupling to the electric field gradient, V_{ij}. The tensor coupling can be simplified by choosing the set of principal axes relative to which $V_{ij} = 0$ for $i \neq j$. From Laplace's equation one obtains the following condition for the diagonal elements:

$$\sum_i V_{ii} = 0 \tag{6.1}$$

Hence, for a nucleus at a site of cubic symmetry with $V_{XX} = V_{YY} = V_{ZZ}$, all three derivatives vanish, and no quadrupole interaction occurs. The Hamiltonian describing the interaction of the nuclear quadrupole moment, Q, with an electric field gradient generated by its surrounding charges is then given by [71]

$$\mathcal{H}_Q = \frac{eQ}{4I(2I-1)} \left[V_{ZZ}(3I_Z^2 - I^2) + (V_{XX} - V_{YY})(I_X^2 - I_Y^2) \right]. \tag{6.2}$$

Capital indices denote the principal axes of the field gradient tensor. The quadrupole interaction therefore removes the degeneracy of the nuclear spin states in zero magnetic field.

In high magnetic fields, as is the case in the experiments of this work, the quadrupole interaction can be taken as an perturbation to the Zeeman energy. In most cases the field gradient has axial symmetry meaning that $V_{XX} - V_{YY} = 0$

for uniaxial strain. If the external field is applied in z-direction which lies in the XZ plane, the coordinates of equation 6.2 transform to

$$I_Z = I_z \cos\theta + I_x \sin\theta \tag{6.3}$$

where θ is the angle between Z and the direction of the external magnetic field, z. The Zeeman Hamiltonian is diagonal in this case, and the energy levels can be calculated by first-order perturbation theory:

$$E_m = -\gamma_\alpha \hbar B_0 m + \frac{eQ}{4I(2I-1)} V_{ZZ} \left(\frac{3\cos^2\theta - 1}{2}\right)\left(3m^2 - I(I+1)\right) \tag{6.4}$$

The effect of the quadrupole coupling is depicted schematically in figure 6.1.

The energy levels are slightly shifted to higher or lower energy for $|m| = 3/2$ or $|m| = 1/2$, respectively. Hence the transition frequencies for $3/2 \leftrightarrow 1/2$ and $-1/2 \leftrightarrow -3/2$ are shifted by $\Delta\nu$ compared to the unperturbed system, whereas the central transition is not affected by the coupling. The splitting of the spectrum, $\Delta\nu_m$, for the transition $m \leftrightarrow m-1$ is given by

$$\Delta\nu_m = \frac{3eQ(2m-1)}{4I(2I-1)h} V_{ZZ} \left(\frac{3\cos^2\theta - 1}{2}\right). \tag{6.5}$$

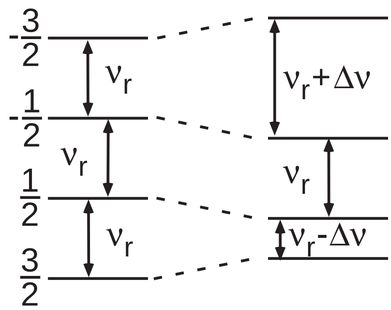

Figure 6.1: Effect of a quadrupole coupling to first order

For spin $I = 3/2$ the spectrum has a central resonance line and two symmetrically shifted satellite lines. If the geometry and symmetry of the quadrupole system in the magnetic field is known, measuring the splitting yields the electric field gradient.

As already mentioned above, gallium and arsenic in bulk materials are sitting at sites of cubic symmetry where they do not experience quadrupole interactions. However, if the system is exposed to strain, the cubic symmetry is broken, and there will be nonzero electric field gradients at the nuclear positions due to changes in the neighboring atom positions and in the chemical bonds. Lemanov [72] and Sundfors et al. [73] have introduced the tensor, $\tilde{S}$, which relates the nuclear electric field gradient, $\tilde{V}$, to the elastic strain tensor, $\tilde{\epsilon}$, of the lattice

$$V_{ij} = \sum_{lm} S_{ij,lm}\epsilon_{lm} \tag{6.6}$$

It is common to use Voigt notation in this context which obeys the following rules [74]:

$$V_j = \sum_k S_{jk}\epsilon_k, \quad j,k = 1\ldots 6, \tag{6.7}$$

$$\begin{aligned} 1 &= xx, & 4 &= yz, \\ 2 &= yy, & 5 &= zx, \\ 3 &= zz, & 6 &= xy. \end{aligned} \tag{6.8}$$

It has been shown by Shulman et al. [75] that for any cubic point-group symmetry, $\tilde{S}$ has only two independent elements: S_{11} and S_{44}. The values, S_{11} and S_{44}, for ^{75}As have been measured by Sundfors [76]:

$$S_{11} = \pm 13.2 \cdot 10^{15}\,\text{statcoulomb}\,\text{cm}^{-3} = \pm 3.96 \cdot 10^{22}\,\text{Vm}^{-2} \tag{6.9}$$

$$S_{44} = \pm 26.5 \cdot 10^{15}\,\text{statcoulomb}\,\text{cm}^{-3} = \pm 7.96 \cdot 10^{22}\,\text{Vm}^{-2} \tag{6.10}$$

The conversion from esu to SI units can be done by multiplying the esu value with the factor $(4\pi\varepsilon_0)^{-1}$ and converting statcoulomb to coulomb: $1\,\text{statcoulomb} = 3.34 \cdot 10^{-10}\,\text{C}$.

The final result for the relationship between the field gradient and the strain in the cubic case is then

$$V_{XX} = S_{11}\left(\epsilon_{XX} - \frac{1}{2}(\epsilon_{YY} + \epsilon_{ZZ})\right) \tag{6.11}$$

$$V_{XY} = S_{44}\epsilon_{XY} \tag{6.12}$$

Cyclic permutations, of X, Y and Z reveal all other field gradient components.

6.3 Resonance Line Splitting

The quadrupole splitting is measured with the setup described in chapter 3. Each isotope is investigated separately in order to have the highest possible resolution. The external field is usually set to a value such that the resonance of each isotope appears around 10 MHz. The frequency is scanned over a region of 100 or 200 kHz within 40 s, and the data is recorded with a digital oscilloscope.

In figure 6.2 NMR spectra of all three isotopes are shown, which have been recorded at the same position of the sample. The spectra stem from the 19.7 nm wide quantum well in sample $\#1431$.

On the left side of figure 6.2 one can see the optical data together with the fits, and on the right side the calculated NMR signal from the fit is shown. One can clearly observe the splitting of the ^{75}As resonance line into three transitions.

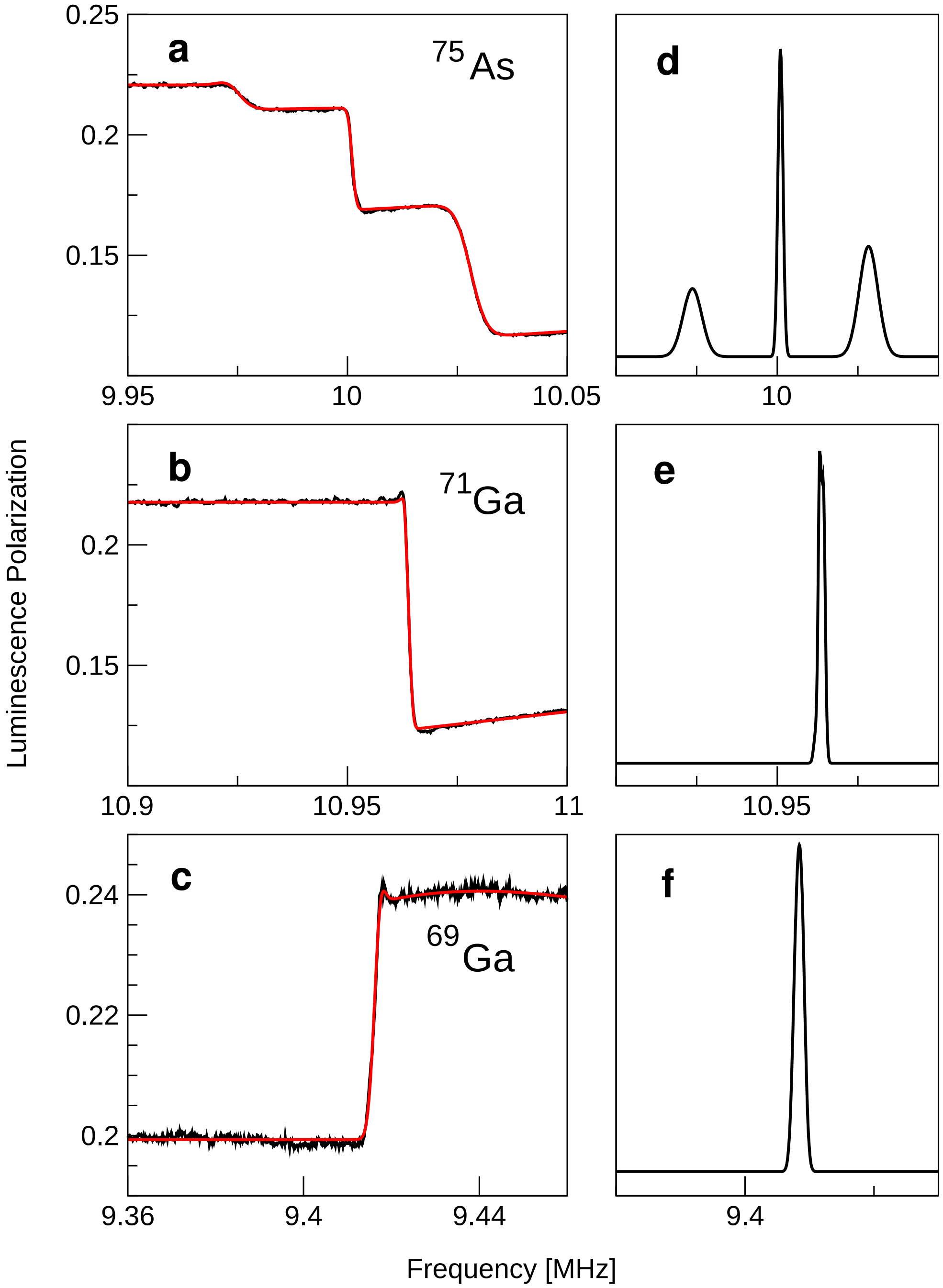

Figure 6.2: NMR spectra of all three isotopes. Figures a-c each show the ODNMR spectra (black line) plotted together with the fits (red line). Figures d-f each show the calculated NMR spectrum using the fitted parameters. All three isotopes are fitted with the assumption of quadrupole splitting, though the splitting can only be resolved for ^{75}As.

It has been ensured by measuring the splitting at different field strengths, that the splitting is independent of the external field. Therefore, the cause of the splitting is assigned to a quadrupole interaction.

The resonances of the two gallium isotopes do not show such a significant splitting, which is typically observed in the experiments with these three samples during this work. However, the lines are broadened and are best fit with the assumption of a small quadrupole splitting. The splitting is in this case on the order of 1 kHz or less, which cannot be resolved in this experiment.

Examples of typical spectra of ^{75}As for each quantum well measured at arbitrary positions are given in figures 6.3 to 6.7. Even without fitting the spectra, it is obvious that the satellite lines are broadened compared to the central line.

The quadrupole splitting is measured in five quantum wells with different thicknesses. The experiment is designed so that all measurements can be carried out within two days, taking special care to ensure that the position of excitation on the sample did not change between two measurements. The line widths for the satellite lines depend on the width of the quantum well, whereas the central line appears to be independent of the well width, as shown in figure 6.8. However, the satellite lines show a dependence on the width of the quantum well which becomes especially broad for the smallest well.

The line shapes of the satellite lines also change, depending on the quantum well width. For the 19.7 nm wide well, shown in figure 6.3, their shape is similar to that of the central line, except for the broadening. In smaller wells, a deviation from the underlying Gaussian resonance appears. It seems, that the signal for the satellite transitions in some quantum wells is kinked, with two different slopes, as indicated by the red lines in figures 6.4 and 6.5. This behavior becomes most evident for the smallest quantum well. It cannot be explained simply by a broadening of the Gaussian resonance line and is therefore not incorporated in the fit.

As already pointed out in the introduction of this chapter, strain reduces the symmetry at the site of the nucleus and induces quadrupole splitting. In order to decide which source of strain is responsible for the splitting, the broadening, and the line shape modification, two possible models will be discussed: internal and external strain.

6.4 Internal Strain

Quadrupole splitting is not observed in solids possessing cubic symmetry, such as GaAs; therefore, the symmetry in this system under study must have been reduced. As has been shown, strain would create electric field gradients at the nuclear sites. One possible reason for strain to occur is microscopic stress induced

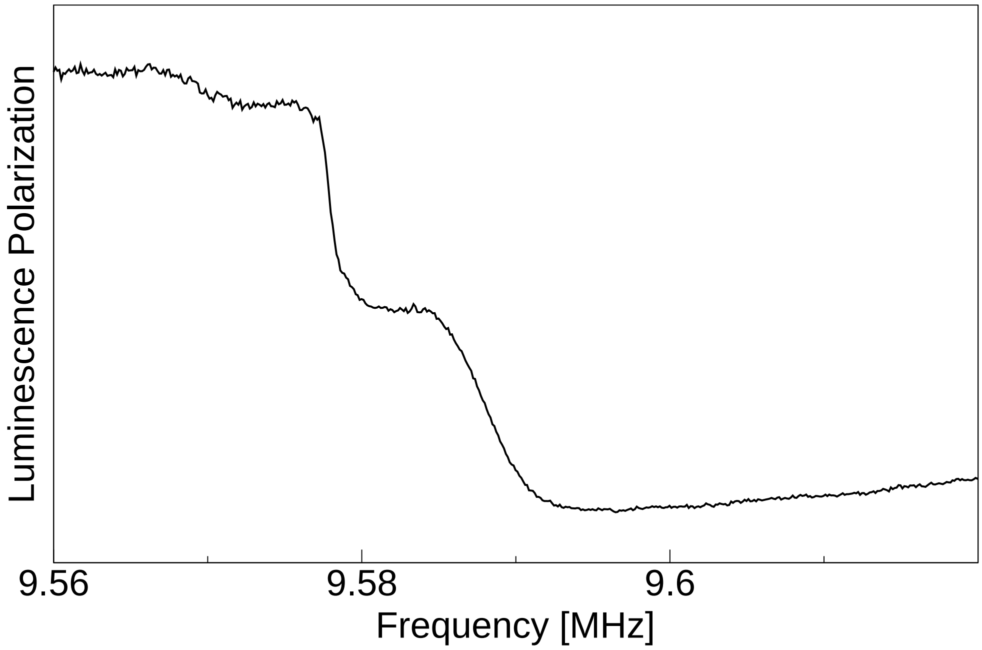

Figure 6.3: ^{75}As spectrum of 19.7 nm wide quantum well.

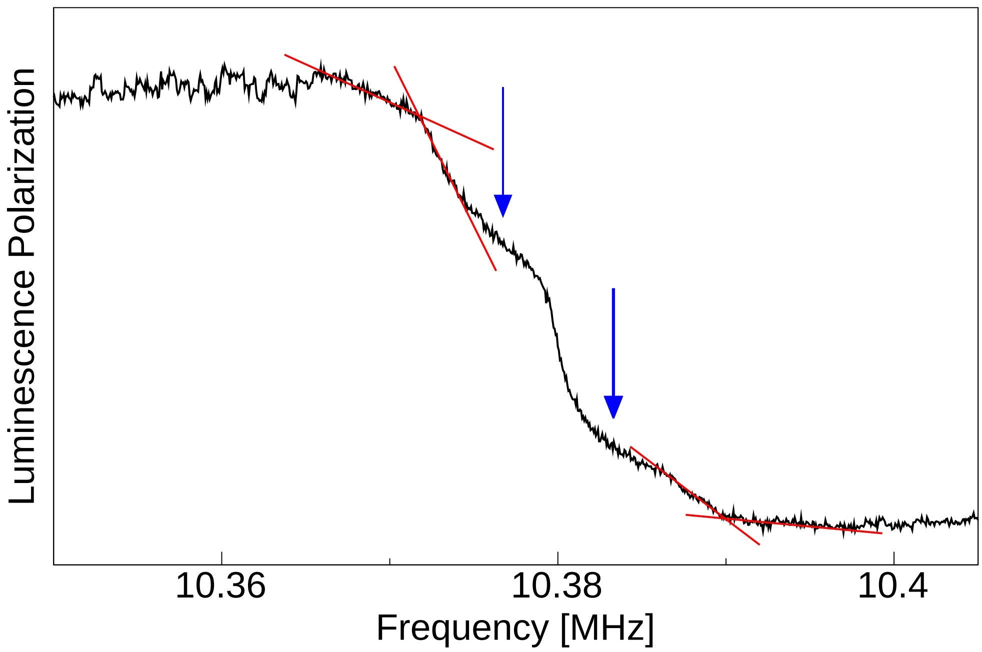

Figure 6.4: ^{75}As spectrum of 14.5 nm wide quantum well. The red lines indicate the different slopes for the satellite transitions. Blue arrows indicate possible two-quantum transitions, as already pointed out in section 5.2.2.

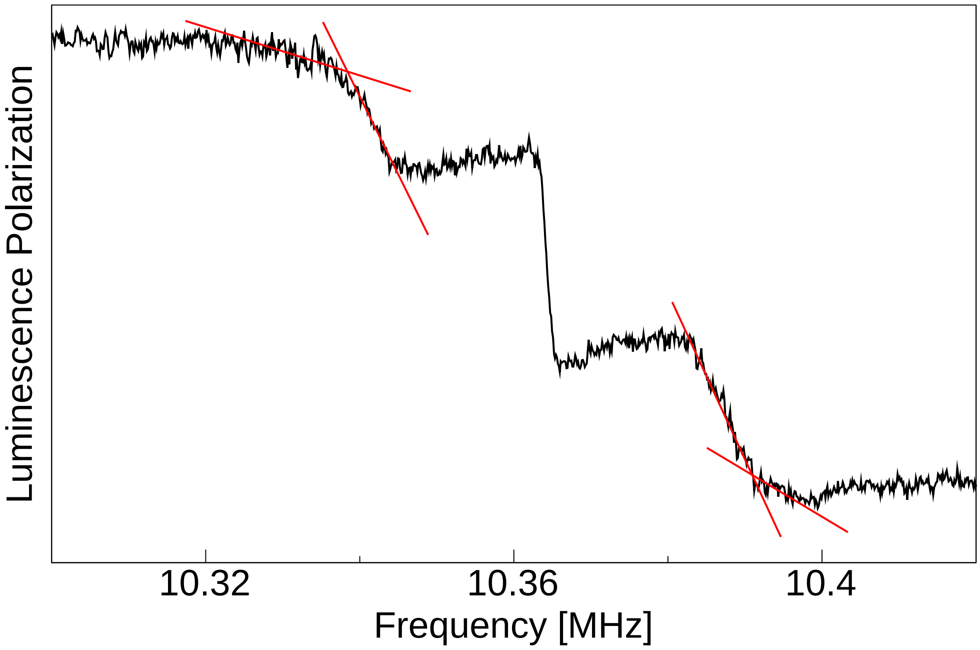

Figure 6.5: ^{75}As spectrum of 11.7 nm wide quantum well. The red lines indicate the different slopes for the satellite transitions.

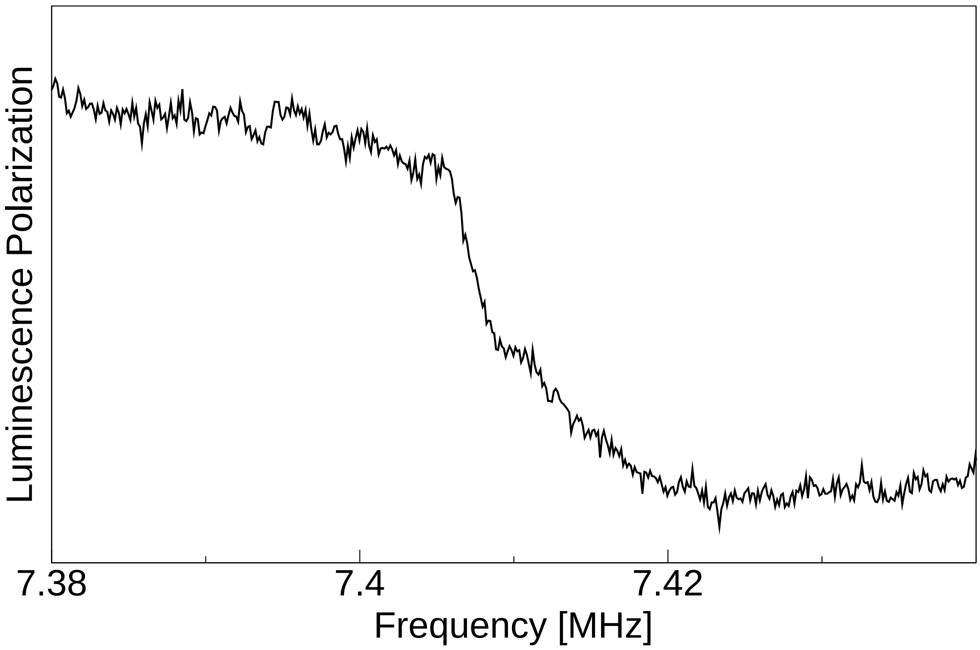

Figure 6.6: ^{75}As spectrum of 10.5 nm wide quantum well.

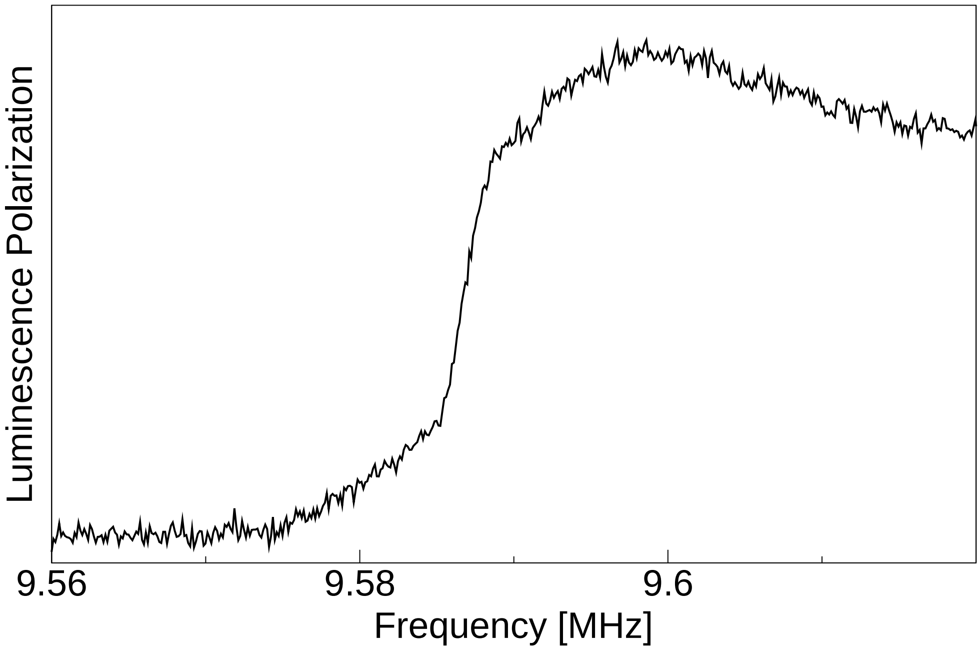

Figure 6.7: ^{75}As spectrum of 6.8 nm wide quantum well. The satellite lines are completely smeared out.

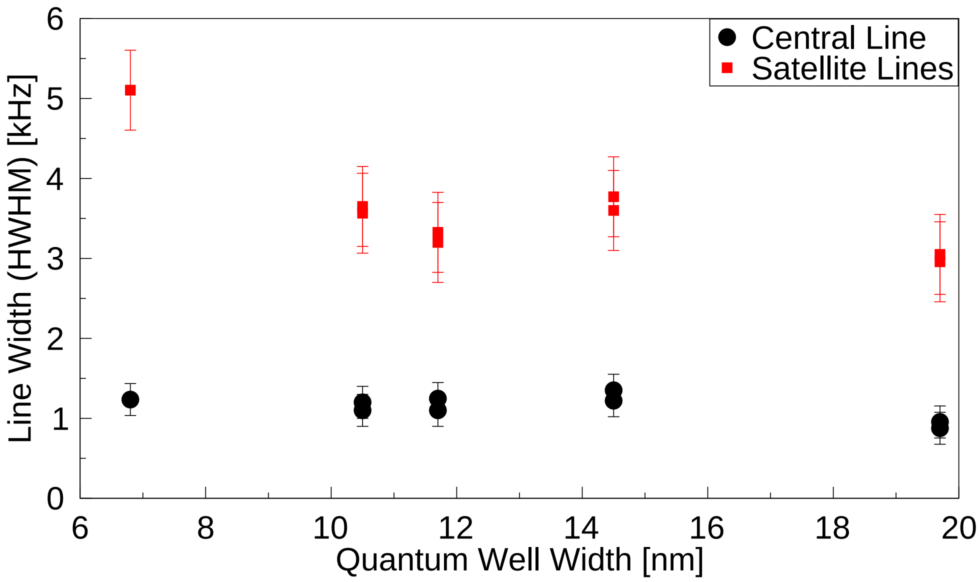

Figure 6.8: The line width dependence of the central and satellite lines of ^{75}As on the quantum well width.

internally by the growth of the heterostructure.

Although the growth of AlGaAs onto GaAs is considered to be lattice matched, the two materials differ in lattice constant by a small amount. Such lattice mismatch can be accommodated by uniform lattice strain in sufficiently thin layers [77]. The in-plane lattice constant, $a_{||}$, of such a so-called "pseudomorphic" interface remains constant throughout the structure. To calculate the strain in each layer, the interface is at first assumed to be ideal; in other words, the bulk atomic structure is maintained up to the interface. For a system with a thin layer of AlGaAs grown on a GaAs substrate buffer layer that is much thicker than the AlGaAs layer, the in-plane lattice constant of the system is that of the GaAs substrate [78]: $a_{||} = a^{GaAs} = 0.5653\,\text{nm}$ [28]. Thus, the in-plane lattice constant in the GaAs quantum wells grown onto the AlGaAs barrier is equal to the bulk one. The in-plane strain is given by [78]:

$$\epsilon^i_{||} = \frac{a_{||}}{a^i} - 1 \tag{6.13}$$

where i denotes the two different materials, GaAs and AlGaAs. The lattice constant of $Al_{0.35}Ga_{0.65}As$ can be calculated using Vegard's law, which claims that the material properties such as the lattice constant change linearly with the concentration of aluminum in the material from GaAs to AlAs. Taking $a^{AlAs} = 0.5660\,\text{nm}$ [28], the lattice constant of $Al_{0.35}Ga_{0.65}As$ is $a^{AlGaAs} = 0.56555\,\text{nm}$. The in-plane strain of GaAs for the ideal interface is $\epsilon^{GaAs}_{||} = 0$ according to equation 6.13, and $\epsilon^{AlGaAs}_{||} = -4.42\cdot 10^{-4}$ for AlGaAs . The strain perpendicular to the interface is given by:

$$\epsilon^i_{\perp} = \frac{a^i_{\perp}}{a^i} - 1 \tag{6.14}$$

with the lattice constant, $a^i_{\perp}$, perpendicular to the interface. This parameter is not equal in the two materials and depends on the elastic constants (c_{11}, c_{12}, c_{44}) of the material and the orientation of the interface [78]:

$$a^i_{\perp} = a^i \left[1 - 2\frac{c_{12}}{c_{11}}\left(\frac{a_{||}}{a^i} - 1\right)\right] \tag{6.15}$$

The elastic constants for $Al_{0.35}Ga_{0.65}As$ can also be calculated with Vegard's law from the constants of GaAs and AlAs, and the results are summarized in table 6.1. Again, the strain in GaAs for an ideal interface is zero, and in the AlGaAs layer the lattice constant perpendicular to the interface is $a_{\perp} = 0.56578\,\text{nm}$, resulting in $\epsilon^{AlGaAs}_{\perp} = 4.07\cdot 10^{-4}$. Inserting these results into equation 6.11 reveals axial symmetry for the electric field gradient, and the resulting line shift due to internal strain can be calculated with equation 6.5.

The investigated layers have certainly non-ideal interfaces, hence the strain is distributed across the interface, causing nonzero strain in the GaAs quantum

	a [nm]	c_{11}	c_{12}	c_{44}
GaAs	0.5653	1.223	0.547	0.600
AlAs	0.5660	1.250	0.534	0.542
$Al_{0.35}Ga_{0.65}As$	0.56555	1.23245	0.55805	0.5797

Table 6.1: Lattice constant, a, and elastic constants, c_{11}, c_{12} and c_{44}, for GaAs and AlAs taken from [78] and for $Al_{0.35}Ga_{0.65}As$ calculated by Vegard's law.

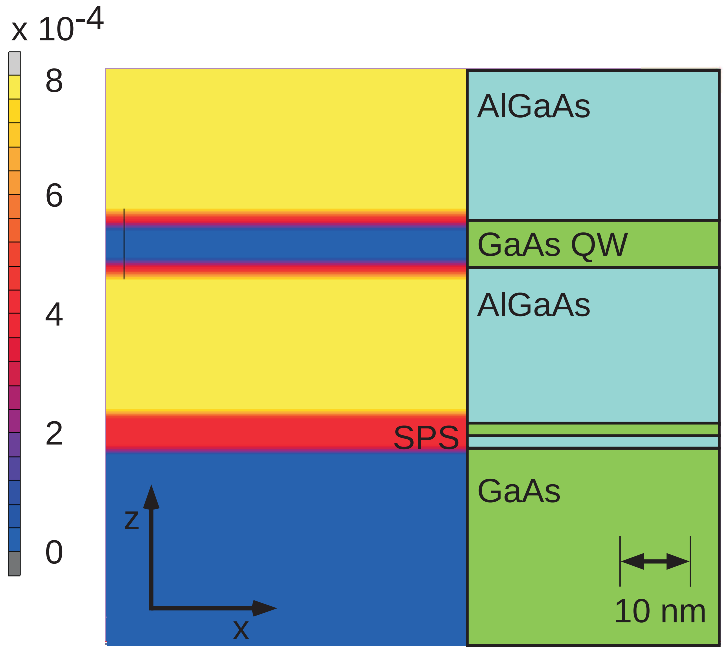

Figure 6.9: On the left, the distribution of the ϵ_{zz}-component of the strain tensor as a result of finite element calculations is shown. On the right, the structure of the sample is depicted. The strain is calculated with respect to the GaAs substrate lattice constant, which gives about a factor of 2 for the maximum strain compared to $\epsilon_{\perp}^{AlGaAs}$ calculated in this section.

wells parallel and perpendicular to the plane of the interface. Simulations with a commercial program (Marc Mentat 2000) using the finite element (FE) method is carried out in order to determine the strain distribution. The program uses a continuum model and the elastic theory, as briefly explained in this section. The sample is modeled as being pseudomorphic, grown on a thick GaAs substrate (100 nm×100 nm×100 nm). One SPS layer is set on top of the substrate, followed by a 30 nm AlGaAs barrier, a 10 nm GaAs quantum well, and a 30 nm barrier on top. Since the dimension in the lateral direction is much bigger than its thickness, the quantum well is not assumed to be "free standing" which is taken into account by setting the appropriate boundary conditions. This condition suppresses the strain relaxation towards the sample-side planes in the x- and y-direction; therefore, no shear strain components can arise.

The simulation calculates the strain in comparison to the GaAs bulk lattice constant for the whole sample. Hence the maximum strain value in the AlGaAs layer is about twice as big as the value given for $\epsilon_{\perp}^{AlGaAs}$ just prior to this section. The calculation reveals only a strain component perpendicular to the interface plane. It is linearly distributed over the GaAs/AlGaAs interface and reaches about 2.5 nm into the quantum well. The strain at the interface is about half of the maximum strain in the AlGaAs barrier. The center of the quantum well is strain-free, down to a well width of 5 nm, where the influence of both interfaces interfere, as is shown by calculations of different well widths.

This result of the distribution of the strain is used in order to simulate the NMR spectra for different quantum well widths. The total NMR spectrum is yielded by calculating the spectrum for each monolayer separately and then adding all monolayer signal contributions together. Each signal is weighted with the expectation value of the electron.

The total quadrupole splitting, $\delta\nu_q$, consists of a constant part, $\delta\nu_q^{ext}$, of presumably an external source, as will be pointed out in sections 6.5 and 6.6, and a strain-dependent part, $\delta\nu_q^{int}$. The latter is calculated using equations 6.5 and 6.11, with the strain, ϵ_{zz}, from the FE calculations. The Gaussian resonance lines all have all equal widths (1 kHz HWHM) and intensities in the simulation. The simulated NMR spectra together with their integrated signals for three different quantum well widths are depicted in figure 6.10.

It is clear that the influence of the strain becomes less important for wider wells, since the number of strained monolayers remains constant for each quantum well. The FE simulation shows, that about 9 monolayers within the quantum well at each interface are strained, which means that the splitting varies by about 2 kHz from monolayer to monolayer. The effect of this huge variation of splitting is manifested in small wiggles in the spectra of figure 6.10. However, these wiggles have an effect on the integrated signal. They appear as broad wings in addition to the resonance, and their contribution to the signal is big enough in

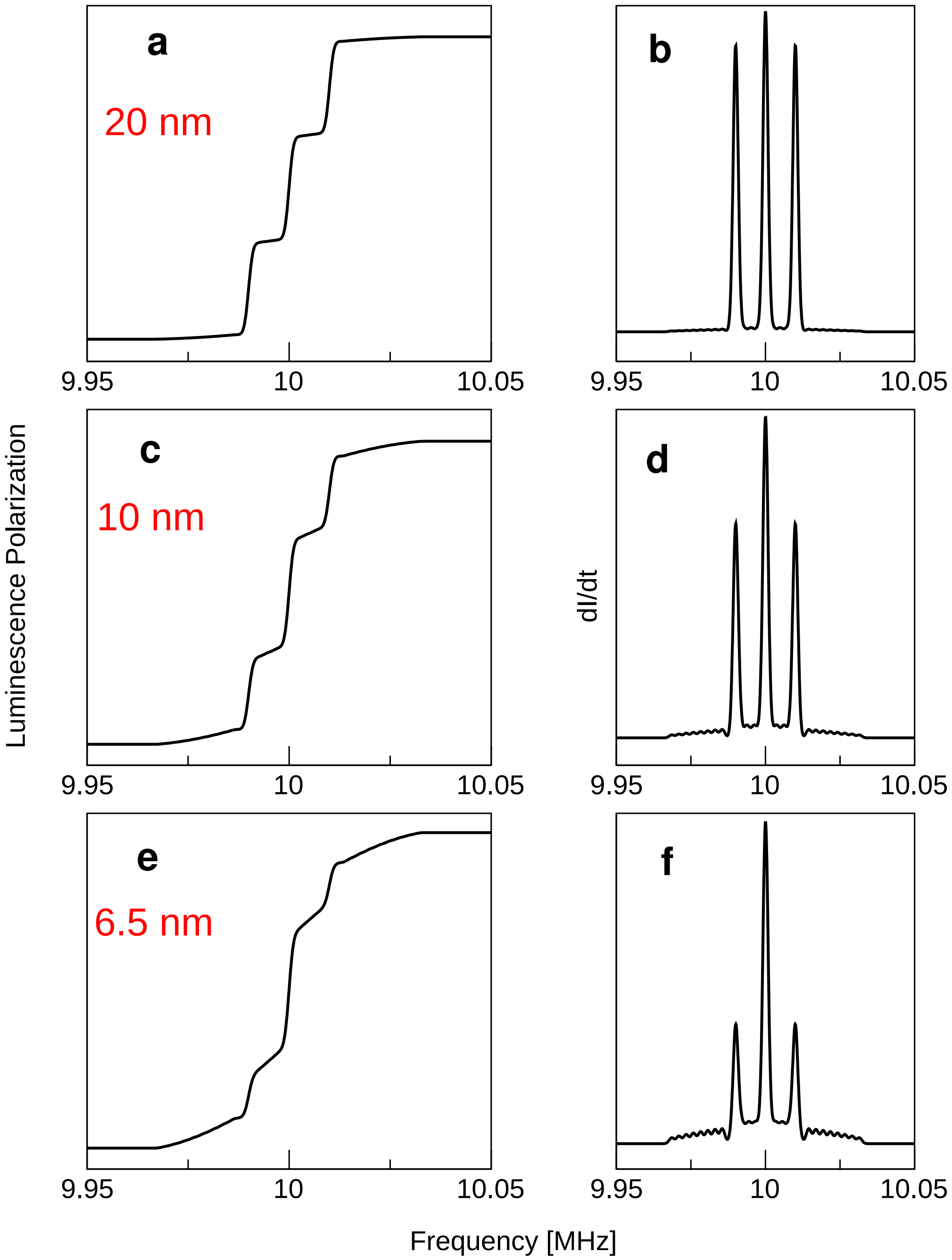

Figure 6.10: Simulation of NMR spectra exposed to internal strain due to lattice mismatch. On the left, the integrated NMR signal is shown; on the right side, the calculated spectra are depicted. The simulation is carried out for different quantum well widths: (a,b) 20 nm, (c,d) 10 nm and (e,f) 6.5 nm. The influence of the strain arises as small wiggles on either side of the satellite lines, and becomes most evident for small well widths.

order to be detectable by ODNMR. The width and slope of the wings depend on the quantum well width and on the constant splitting, $\delta\nu_q^{ext}$, for which the fitted values are used in the simulation.

Comparison of the integrated NMR spectra with the measured ODNMR spectra in figures 6.3 to 6.7 indicates that these data also might show a similar trend. However, the simulation is not fully consistent with the data. The simulation still shows sharp resonances that do not appear in the ODNMR spectrum. One interpretation is that the strain perpendicular to the interface plane is not the only contribution to the line broadening. An important contribution to the interface strain, which is not included in the simulation, is the strain arising from monolayer splittings. In an ideal model this splitting creates a new interface parallel to the growth direction.

The FE simulation for a monolayer step in the x-direction reveals that in addition to the hydrostatic strain, ϵ_{zz}, a shear strain component, ϵ_{xz}, of the same order of magnitude appears. This should have an important influence on the NMR signal for two reasons: the NMR signals to the left and right of the monolayer step are different due to the presence of a different number of monolayers, but more importantly, the EFG-tensor components, V_{XX} and V_{YY}, are not equal anymore. Hence, the electric field gradient lacks axial symmetry in the vicinity of the step, and an asymmetry factor must be introduced into equation 6.2 [71]. Therefore, the quadrupole splitting due to the two strain components becomes different in regions close to the monolayer step compared to the rest of the quantum well. The interface defects usually form islands with varying sizes, meaning that monolayer splitting occurs in the x- and y-directions. These different orientations of interfaces in the well create some distribution of strain amplitudes and directions. This distribution should smear out the broadened satellite resonance line, which has not been simulated but might be observed in the spectra.

6.5 External Strain

The broadening of the satellite lines can be attributed to internal strain, as shown in the previous section. However, internal strain does not explain the very large splitting, which is included in the simulation of the NMR spectra as a constant splitting, $\delta\nu_q^{ext}$. The reason for this constant splitting is likely to be externally applied strain.

The sample is glued with silver based thermal epoxy to the sample holder, meaning the sample is affixed with the GaAs bulk substrate down onto copper. These two materials have different thermal expansion coefficients, whereby the changes of contraction during the cooling process cause strain at the GaAs/copper interface. The linear expansion coefficient, α, for expansion over a temperature range, ΔT, in one dimension is defined by

$$\frac{\Delta l}{L_0} = \alpha \Delta T \tag{6.16}$$

where Δl is the expansion and L_0 the original length. The relative strain, ϵ, is also defined as the change of length, Δl, over the total length, L_0.

Hence the strain induced at the interface can be estimated with

$$\epsilon = (\alpha^{Cu} - \alpha^{GaAs})\Delta T. \tag{6.17}$$

The values for the temperature-dependent expansion coefficients for GaAs and copper are taken from [63] and [79], and the relative strain after cooling from room temperature down to 4 K is approximately $\epsilon \approx 2 \cdot 10^{-3}$ parallel to the plane of the interface. The strain perpendicular to this plane should be on the same order of magnitude since all components of the elasticity tensor of GaAs are of the same order of magnitude. Since α^{GaAs} is smaller than α^{Cu}, the sample is contracted at the interface with the sample holder as depicted schematically in figure 6.11. The strain is certainly not constant throughout the sample but weakens drastically in the growth direction, meaning that the strain per layer is the smallest on the top of the sample. Therefore, one expects a dependence of the externally induced strain on the vertical position of the quantum well within the sample. Most of the sample thickness is bulk material (500 μm), and the MBE-grown portion on top of the buffer layer is 660 nm thick. The quantum wells are grown with the widest ones at the bottom and the smallest ones on top of the sample; hence, the external strain can be expected to be weakest in the smallest quantum well.

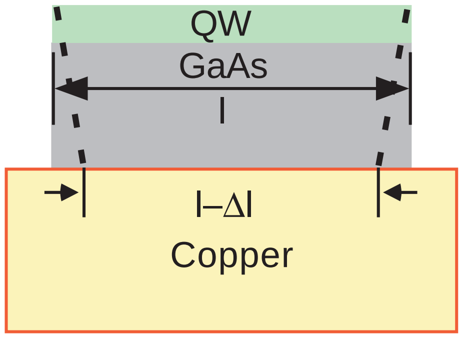

Figure 6.11: Cross section of the sample holder. The quantum well sample has a bulk GaAs substrate base and is glued to the copper sample holder.

The dependence of the splitting of the resonance lines on the quantum well position is measured for five different quantum wells (see figures 6.3 to 6.7). The results are shown in figure 6.12, where the splitting is plotted against the distance of the middle of each quantum well from the top of the sample.

A dependence of the strain from the position of the quantum well can be clearly observed as predicted by the model. However, it is too simple to extract detailed information about the distribution of strain within the sample. In particular, the influence of the thermal expansion coefficient of the epoxy is not

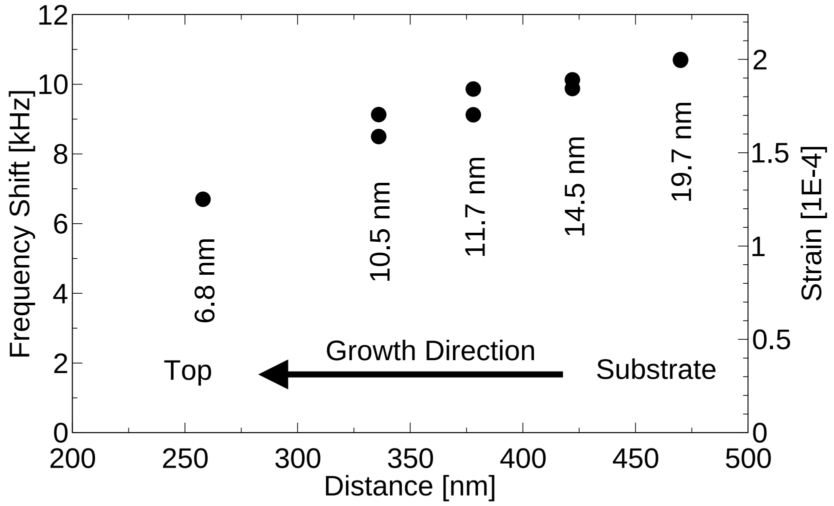

Figure 6.12: Dependence of the quadrupole splitting on the position of the quantum well in the growth direction. The distance of the middle of each quantum well is measured from the top of the sample.

considered. However, if one assumes for the sake of simplicity an uniaxial strain distribution in the lateral direction of the sample in each layer, the electric field gradient has axial symmetry. The strain can then be calculated from the splitting with equations 6.5 and 6.11 and is depicted on the right scale in figure 6.12. The strain is reduced by one order of magnitude from the bottom to the top and is comparable to other experiments involving external strain applied to GaAs quantum wells published in [80].

The strain distribution is not as simple as shown in figure 6.11 but shows inhomogeneities, resulting in differences of quadrupole splitting of the resonances across the sample. The splitting is measured for different positions on the sample, and the results are depicted in figure 6.13. The splitting varies from about 1 kHz, which is not resolvable, to about 12 kHz (or even more in measurements not shown here) and are probably caused by inadequately affixing the sample to the holder. These variations in strain might lead to a broadening of the resonance lines, since the detected signal stems from a relatively large area of 100 μm in diameter. The simulation of the NMR signal from section 6.4 shows, that a small broadening could be induced by very small strain variations on the order of $\Delta\epsilon = 10^{-5}$. Small variations of external strain within the excitation radius would affect all monolayers in the quantum well and therefore have an impact on the NMR signal. However, the distribution of the strain differences can be assumed to be of the same type for all quantum wells, and the broadening is therefore expected to be constant in all layers. Therefore, the distribution of

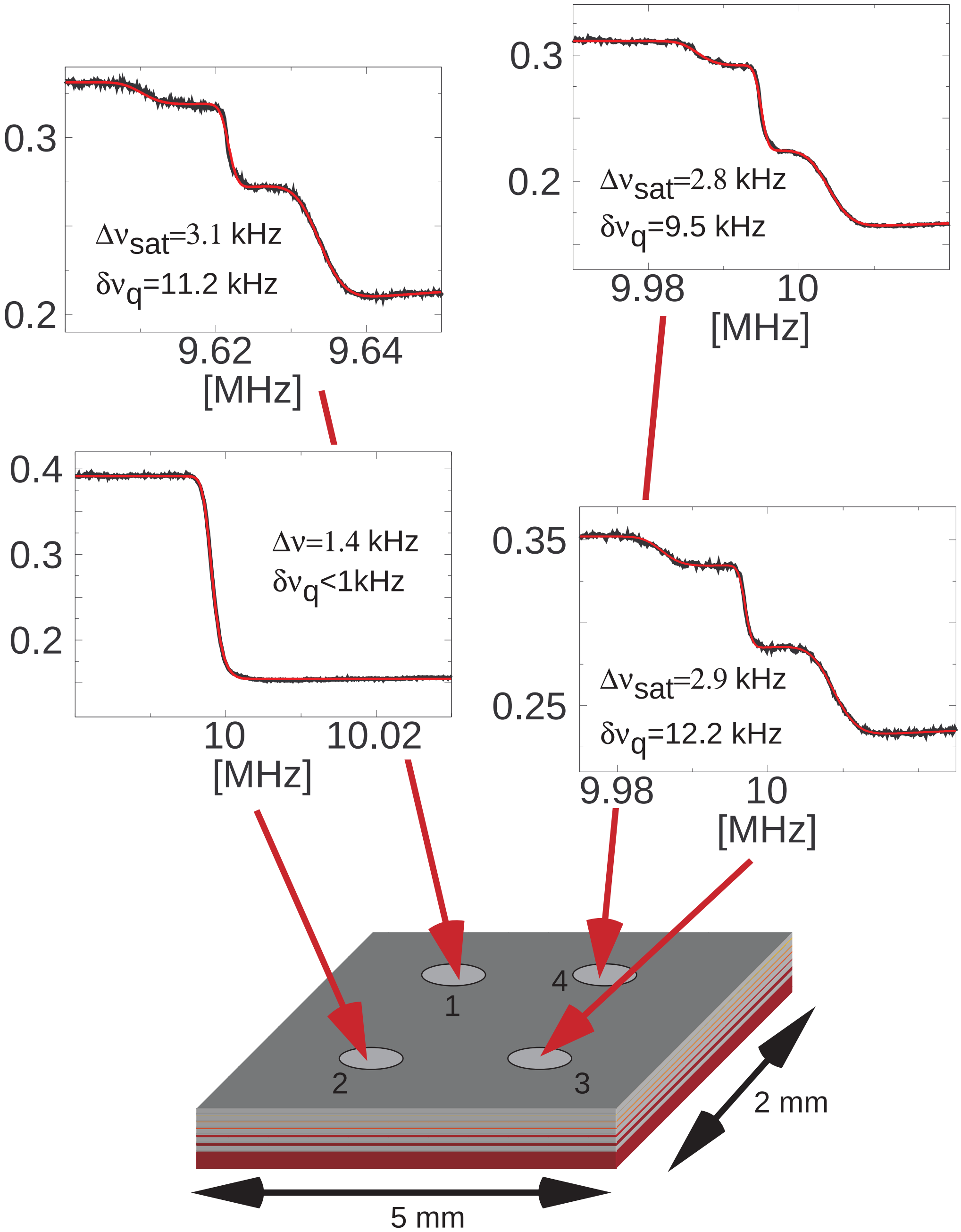

Figure 6.13: Quadrupole splitting in the ^{75}As of 19.7 nm quantum well for different positions on the sample. The spectra show the evolution of the luminescence polarization during the rf scan. The width of the central line is about 0.9 kHz in all figures. $\Delta\nu_{sat}$ denotes the width of the satellite lines (HWHM) and $\delta\nu_q$ is the quadrupole splitting. For position 2 the quadrupole splitting is not resolved; therefore, it is fitted with, $\delta\nu_q = 0$, in order to obtain the linewidth $\Delta\nu$ of the resonance line.

external strain might be one reason for the broadening of the satellite lines, but does not explain the quantum well width-dependence of the broadening.

6.6 Electric Field Effects

Another source for quadrupole splitting not considered thus far is the influence of homogeneous electric fields in the sample and the influence of excitons. Since the nuclei in GaAs are located at positions that lack inversion symmetry, the quadrupole moment of the nuclei couples to a homogeneous electric field [81]. The matrix element of the induced EFG of this indirect process is [82] [83]

$$V_{ij} = (V_{ij})_{E=0} + \sum_k C_{ijk} E_k \tag{6.18}$$

The coupling constant, C_{ijk}, vanishes except for $i \neq j \neq k$, and all these elements are equal, leaving C_{14} in Voigt notation as the only independent element. The coupling constant of ^{75}As is $C_{14} = 1.55 \cdot 10^{12}$ m^{-1} [82].

The electric field across the quantum wells is on the order of 10^7 Vm^{-1}, which is measured by applying an external electric field, compensating the internal one, which is evident from blue shifts of the PL line. This field creates an electric field gradient of about 10^{19} Vm^{-2}, which creates a splitting on the order of 10^4 Hz. This is on the order of the splitting that is attributed to external strain. Experiments with an external electric field applied to the sample show that the quadrupole splitting can be modified by several kHz; therefore, the electric field is part of the source for the quadrupole splitting.

The electric field is constant in all quantum wells; therefore, a quantum well width dependence of the splitting as depicted in figure 6.8 should not occur. As already pointed out, the splitting is most obvious for the arsenic transition in most experiments, whereas the splitting is hardly resolvable for the gallium resonances. This cannot be explained by the different quadrupole moments of the three isotopes, because the ratio of the coupling constants are not equal to the ratio of the splittings. However, if one assumes that the splitting by the external strain is partially compensated by the splitting due to the coupling to the electric field, the derivation of the splitting ratios can be understood.

A further source of electric fields has its origins in the optical means of the experiment, i.e., the excitons. The exciton is an electron-hole pair that interacts through an attractive Coulomb interaction. Hence, the exciton creates an electric field at the site of the nucleus. In order to obtain an upper limit approximation for the field created by the exciton, only the field created by a spherical electron cloud with the radius of the exciton is considered. The field on the "surface" of this electron with a radius of 10 nm is about 10^6 Vm^{-1}. The electric field gradient is therefore at least an order of magnitude smaller than the one discussed above. The influence of the excitonic electric field can therefore be neglected as a source for quadrupole splitting.

The direct electric field gradient for such a simple complex can be estimated to be $-2 \cdot 10^{14}$ Vm^{-2} at a distance of 10 nm away from the center of the exciton. This is significantly smaller than any other electric field gradient discussed so far, and therefore does not contribute significantly to the splitting or the broadening of the quadrupole satellite lines.

6.7 Summary

In this chapter the influence of quadrupole interaction of the nuclei with electric field gradients caused by the neighboring atoms is discussed. The experimental data clearly reveal splitting of the resonance lines that was produced by quadrupole interactions. The data also show significant broadening of the satellite lines. The reduction of the cubic symmetry of GaAs is attributed to strain within the quantum well and an electric field across the sample. Two possible reasons for strain are discussed, and their influence on the spectra is modeled. From these models it can be deduced that the source of the splitting is externally-applied strain by the mounting of the sample and a homogeneous electric field across the sample. These two effects partially cancel each other, resulting in quadrupole splitting ratios which cannot be explained by the quadrupole moment ratios of the three isotopes. Excitonic effects are shown to play only a minor role for the spectra. The broadening of the resonance lines is caused by internal strain created by lattice mismatch of GaAs and AlGaAs and by monolayer splitting, which creates an additional shear strain component.

Chapter 7

Conclusions

This thesis presents advancements in the spectroscopic method of optically detected nuclear magnetic resonance (ODNMR) applied to semiconductor heterostructures to investigate nanoscopic structural details in these systems. Experiments are carried out on type I GaAs/AlGaAs quantum wells of various thicknesses, investigating new aspects about the behavior of the coupled electron-nuclear spin system. Characterization and interpretation of the specific features of the ODNMR spectra are carried out, providing spectroscopic applications for studying low-dimensional heterostructure systems. Utilizing the sensitivity and selectivity of ODNMR, structural information is revealed about GaAs/AlGaAs interfaces and quantum wells.

A high degree of nuclear spin polarization is achieved by optically pumping the coupled electron-nuclear spin system. The hyperfine coupling constant, governing the electron-nuclear interaction, is derived for quantum wells of various thicknesses by calculating the electronic wavefunction within a quantum well. The coupling can be described as magnetic fields having both nuclear and electronic origins, and values of these fields are estimated.

The dependence of the luminescence polarization on both the external and nuclear magnetic fields, the so called Hanle effect, is derived. This dependence enables optical detection of nuclear magnetic resonance. Hanle curves for different well widths are shown, and temperature and laser intensity influences are discussed. Hanle measurements are carried out by suppressing nuclear polarization and are compared to Hanle curves shifted by the influence of nuclear magnetic fields. The size of the maximum magnetic field is measured separately for each isotope in quantum wells of different thicknesses.

Continuous wave ODNMR is applied to the quantum wells in three samples of different interface quality. The spectra show the very high sensitivity of the ODNMR technique, allowing the detection of less than 10^{11} nuclear spins. Utilizing the spectral selectivity of the optical method allows separate investigations of quantum wells of specific thicknesses. Using a phenomenological fit function permits the ODNMR signal to be deconvoluted from the underlying NMR spectrum and reveals the widths and intensities of the resonance lines. The results are compared with numerical simulations using density matrix formalism.

The ODNMR technique is used to investigate different relaxation processes governing the optical pumping process. The field dependence of the optical pumping relaxation time is measured, and the "dark" relaxation time is obtained separately for each isotope by suppressing optical pumping.

As a polarization-conserving method, adiabatic rapid passage through the nuclear resonance is implemented. The nuclear polarization is inverted rather than saturated; therefore, reversal of the RF scan direction restores the initial polarization. More than 120 scans are possible, implying that losses are relatively small during the inversion of the nuclear polarization.

It is shown that delocalized optically oriented electrons do not contribute to polarizing the nuclear spin system. It is assumed that trapping of excitons at interface defects plays the key role in amplifying the hyperfine interaction. A model is presented, to approximate the effect on the hyperfine relaxation time, T_{1e}, and it is found that the relaxation time is decreased by one to two orders of magnitude compared to unbound excitons. Therefore, optical pumping becomes more efficient than other relaxation processes, and eventually, a nuclear polarization can build up. The theoretical model is supported by comparison of different samples, revealing a dependence of the hyperfine relaxation time on the interface quality.

The calculation of the nuclear magnetic field acting on the electrons shows significant well width dependence and reaches values of over 20 T in narrow (5 nm) wells. Comparison with experimentally obtained nuclear fields from Hanle curve shifts show that the nuclear system is polarized to a very high degree, reaching levels of 20% or more. The effective electronic magnetic field acting on the nuclei is calculated for a 20 nm wide quantum well and is, at best, on the order of a few micro tesla, too small to be resolved with the current experimental setup.

New information about the hyperfine coupling mechanisms of the electron-nuclear spin system is obtained and demonstrates that the coupling to the electrons becomes very efficient at zero effective magnetic field. This coupling results in an external field dependence of the optically pumped nuclear field. It is found experimentally that within some range of external magnetic field strengths, the nuclear field tries to cancel out the external field, creating an effective field nearly equal to zero felt by the electrons. This behavior is observed as a locking of the top of the Hanle curve to the externally applied field during a field scan and becomes apparent in the field dependence of the optical pumping time, T_1^f. Destroying the polarization of only one isotope will cause the other two isotopes to compensate the losses of total nuclear field, which becomes obvious in the adiabatic rapid passage experiments.

The ODNMR resonances are identified as belonging to the major components of the GaAs quantum well heterostructure. It is shown from calculations that nuclei situated in the barrier do not contribute noticeably to the ODNMR signal, due to the small penetration depth of the electron wavefunction into the barrier. In agreement with the wavefunction calculations, no evidence for signals from the barrier is observed. The line widths are comparable to values published earlier using different NMR techniques, indicating that the ODNMR method does not drastically influence them. However, the line intensities differ from the commonly accepted ones of quadrupolar systems. Numerical simulations of the NMR spectra confirm this deviation from the common intensity distribution. The simulations also reveal that the population distribution for the nuclei are different from a Boltzmann distribution. Therefore, the spin temperature concept proposed by D'yakonov does not apply for the quantum well systems under investigation. Two-quantum transitions are predicted by the simulation and are observed experimentally, even at low RF field intensities.

Nuclear spin diffusion distributes the polarization from nuclei within the exciton trapping site to neighboring nuclear spins. This effect causes broadening of the shifted Hanle curves due to an inhomogeneous nuclear magnetic field distribution. The field dependent "dark" relaxation times, T_1, obtained with the optical relaxation being suppressed, reveal that spin diffusion plays an important role as a relaxation process in optically *detected* nuclear magnetic resonance.

The resonance lines show large splittings which are attributed to quadrupole interactions of the nuclei with electric field gradients caused by the neighboring atoms. The reduction of the cubic symmetry of GaAs is attributed to interfacial effects at the AlGaAs/GaAs barrier, to strain within the quantum well applied externally by the mounting of the sample, and to a homogeneous electric field across the sample. These latter two effects partially compensate each other, leading to splitting ratios between the three isotopes in the GaAs quantum well, which deviate from the ratios of the quadrupole moments between the isotopes. The ODNMR data also show significant broadening of the satellite lines, which arises from internal strain created by lattice mismatch of the heterostructure and by monolayer splitting (interface roughness), which creates an additional shear strain component.

Bibliography

[1] A. Overhauser. Polarization of nuclei in metals. *Physical Review*, 92:411, 1953.

[2] G. Lampel. Nuclear dynamic polarization by optical electronic saturation and optical pumping in semiconductors. *Physical Review Letters*, 20:491–3, 1968.

[3] A. I. Ekimov and V. I. Safarov. Optical electron-nuclear resonance in semiconductors. *Pis'ma v Zhurnal Eksperimental'noi i Teoreticheskoi Fiziki*, 15:453–5, 1972.

[4] A. I. Ekimov and V. I. Safarov. Optical detection of dynamic polarization of nuclei in semiconductors. *Pis'ma v Zhurnal Eksperimental'noi i Teoreticheskoi Fiziki*, 15:257–61, 1972.

[5] V. L. Berkovits, A. I. Ekimov, and V. I. Safarov. Optical orientation in a system of electrons and lattice nuclei in semiconductors. experimental. *Zhurnal Eksperimental'noi i Teoreticheskoi Fiziki*, 65:346–61, 1973.

[6] M. I. D'Yakonov, V. I. Perel, V. L. Berkovits, and V. I. Safarov. Optical effects due to polarisation of nuclei in semiconductors. *Zhurnal Eksperimental'noi i Teoreticheskoi Fiziki*, 67:1912–24, 1974.

[7] B. P. Zakharchenya, M. E. Kompan, and V. G. Fleisher. Semiconductor magnetization by light and nuclear magnetic resonance during optical pumping in a transverse field. *Zhurnal Eksperimental'noi i Teoreticheskoi Fiziki, Pis'ma v Redaktsiyu*, 19:734–7, 1974.

[8] V. G. Fleisher, V. L. Vekua, R. I. Dzhioev, and B. P. Zakharchenya. Polarisation instability in an electron nuclear spin system of n-type semiconductor, with optical orientation in weak magnetic fields. *Zhurnal Eksperimental'noi i Teoreticheskoi Fiziki, Pis'ma v Redaktsiyu*, 21:547–51, 1975.

[9] V. K. Kalevich and V. L. Korenev. Nonlinear properties of an electron-nuclear spin system of algaas crystals in a strong magnetic field. *Fizika Tverdogo Tela*, 30:2071–5, 1988.

[10] B. P. Zakharchenya, V. K. Kalevich, V. D. Kul'kov, and V. G. Fleisher. Optical orientation of the electron-nucleus spin system in a semiconductor in an inclined magnetic field. *Fizika Tverdogo Tela*, 23:1387–94, 1981.

[11] D. Paget, G. Lampel, B. Sapoval, and V. I. Safarov. Low field electron-nuclear spin coupling in gallium arsenide under optical pumping conditions. *Physical Review B (Solid State)*, 15:5780–96, 1977.

[12] D. Paget. Optical detection of nmr in high-purity gaas under optical pumping: Efficient spin-exchange averaging between electronic states. *Physical Review B (Condensed Matter)*, 24:3776–93, 1981.

[13] D. Paget. Optical detection of nmr in high-purity gaas: direct study of the relaxation of nuclei close to shallow donors. *Physical Review B (Condensed Matter)*, 25:4444–51, 1982.

[14] F. Meier and B.P. Zakharchenya. *Optical Orientation*. Elsevier Science, 1984.

[15] G. P. Flinn, R. T. Harley, M. J. Snelling, and A. C. Tropper. Optically detected nuclear magnetic resonance in semiconductor quantum wells. *Journal of Luminescence*, 45:218–20, 1989.

[16] G. P. Flinn, R. T. Harley, M. J. Snelling, A. C. Tropper, and T. M. Kerr. Optically detected nuclear magnetic resonance of nuclei within a quantum well. *Semiconductor Science and Technology*, 5:533–7, 1990.

[17] M. Schreiner, M. Krapf, H. Pascher, G. Denninger, G. Weimann, and W. Schlapp. Optically detected electron spin polarization and hanle effect in algaas/gaas heterostructures. *Superlattices and Microstructures*, 11:409–14, 1992.

[18] M. Schreiner, H. Pascher, G. Denninger, S. A. Studenikin, G. Weimann, and R. Losch. Nuclear spin relaxation in algaas/gaas heterostructures observed via optically detected magnetic resonance (odmr) experiments. *Solid State Communications*, 102:715–20, 1997.

[19] M. Schreiner, H. Hochstetter, H. Pascher, and S. A. Studenikin. Lineshapes of optically detected nuclear magnetic resonance in gaas/algaas heterostructures. *Journal of Magnetic Resonance*, 124:80–6, 1997.

[20] T. Wimbauer, M. S. Brandt, M. W. Bayerl, N. M. Reinacher, M. Stutzmann, D. M. Hofmann, Y. Mochizuki, and M. Mizuta. Recombination centers in gaas/al/sub 0.4/ga/sub 0.6/as heterostructures investigated by optically and electrically detected magnetic resonance. *Physical Review B (Condensed Matter)*, 58:4892–902, 1998.

[21] S. K. Buratto, D. N. Shykind, and D. P. Weitekamp. Time-sequenced optical nuclear magnetic resonance of gallium arsenide. *Physical Review B (Condensed Matter)*, 44:9035–8, 1991.

[22] J. A. Marohn, P. J. Carson, J. Y. Hwang, M. A. Miller, D. N. Shykind, and D. P. Weitekamp. Optical larmor beat detection of high-resolution nuclear magnetic resonance in a semiconductor heterostructure. *Physical Review Letters*, 75:1364–7, 1995.

[23] S. E. Barrett, R. Tycko, L. N. Pfeiffer, and K. W. West. Directly detected nuclear magnetic resonance of optically pumped gaas quantum wells. *Physical Review Letters*, 72:1368–71, 1994.

[24] D. Gammon, S. W. Brown, E. S. Snow, T. A. Kennedy, D. S. Katzer, and D. Park. Nuclear spectroscopy in single quantum dots: nanoscopic raman scattering and nuclear magnetic resonance. *Science*, 277:85–8, 1997.

[25] J. M. Kikkawa and D. D. Awschalom. All-optical magnetic resonance in semiconductors. *Science*, 287:473–6, 2000.

[26] G. Salis, D. T. Fuchs, J. M. Kikkawa, D. D. Awschalom, Y. Ohno, and H. Ohno. Optical manipulation of nuclear spin by a two-dimensional electron gas. *Physical Review Letters*, 86:2677–80, 2001.

[27] S. Eshlaghi. *GaAs/AlGaAs Quantentoepfe: MBE-Wachstum, Charakterisierung und laterale Modulation mittels fokussierter Ionenstrahlen*. Universitaetsverlag, 2000.

[28] J.H. Davies. *The physics of low-dimensional systems*. Cambridge University Press, 1 edition, 1998.

[29] A. R. Denton and N. W. Ashcroft. Vegard's law. *Physical Review A (Statistical Physics, Plasmas, Fluids, and Related Interdisciplinary Topics)*, 43:3161–4, 1991.

[30] L. De Caro, C. Giannini, L. Tapfer, H. P. Schonherr, L. Daweritz, and K. H. Ploog. Validity of vegard's rule for the lattice parameter and the stiffness elastic constant ratios of the algaas ternary compound. *Solid State Communications*, 108:599–603, 1998.

[31] L. De Caro, C. Giannini, L. Tapfer, H. P. Schonherr, L. Diweritz, and K. H. Ploog. Validity of vegard's rule for the lattice parameter and the stiffness elastic constant ratios of the algaas ternary compound. *Solid State Communications*, 108:77–81, 1998.

[32] Li Ming-Fu. *Modern semiconductor quantum physic*. World Scientific, 1994.

[33] H.C. Casey and M.B. Panish. *Heterostructure Lasers*. Academic Press, 1978.

[34] K.J. Moore. *Optical properties and band alignments of III-V heterostructures*, volume 206. NATO ASI Series,B, 1989.

[35] P. D. Altukhov, A. A. Bakun, A. V. Krutitskii, A. A. Rogachev, and G. P. Rubtsov. Magnetic properties of excitons associated with a surface-charge layer in silicon. *Pis'ma v Zhurnal Tekhnicheskoi Fizika*, 15:17–21, 1989.

[36] C. Weisbuch, R. C. Miller, R. Dingle, A. C. Gossard, and W. Wiegmann. Intrinsic radiative recombination from quantum states in gaas-al/sub x/ga/sub 1-x/as multi-quantum well structures. *Solid State Communications*, 37:219–22, 1981.

[37] G. Bastard, C. Delalande, M. H. Meynadier, P. M. Frijlink, and M. Voos. Low-temperature exciton trapping on interface defects in semiconductor quantum wells. *Physical Review B (Condensed Matter)*, 29:7042–4, 1984.

[38] C. Delalande, M. H. Meynadier, and M. Voos. Effect of temperature on exciton trapping on interface defects in gaas quantum wells. *Physical Review B (Condensed Matter)*, 31:2497–8, 1985.

[39] M. I. D'Yakonov and V. I. Perel. Spin relaxation of conduction electrons in noncentrosymmetric semiconductors. *Fizika Tverdogo Tela*, 13:3581–5, 1971.

[40] S. N. Jasperson and S. E. Schnatterly. An improved method for high reflectivity ellipsometry based on a new polarization modulation technique. *Review of Scientific Instruments*, 40:761–7, 1969.

[41] A. Abragam. *The principles of nuclear magnetism*. Claredon Press, 1 edition, 1961.

[42] M.I. D'yakonov and V.I. Perel. *Theory of optical spin orientation of electrons and nuclei in semiconductors*. North Holland Physics Publisher, 1 edition, 1984.

[43] W Kohn. Shallow impurity states in si and ge. *Solid State Physics*, 5:257–320, 1957.

[44] M. Grundmann and D. Bimberg. Anisotropy effects on excitonic properties in realistic quantum wells. *Physical Review B (Condensed Matter)*, 38:13486–9, 1988.

[45] G. Bastard, E. E. Mendez, L. L. Chang, and L. Esaki. Exciton binding energy in quantum wells. *Physical Review B (Condensed Matter)*, 26:1974–9, 1982.

[46] R. C. Miller, D. A. Kleinman, W. T. Tsang, and A. C. Gossard. Observation of the excited level of excitons in gaas quantum wells. *Physical Review B (Condensed Matter)*, 24:1134–6, 1981.

[47] C. Kittel. *Einfuehrug in die Festkoerperphysik*. Oldenbourg, 6 edition, 1983.

[48] M. J. Snelling, G. P. Flinn, A. S. Plaut, R. T. Harley, A. C. Tropper, R. Eccleston, and C. C. Phillips. Magnetic g factor of electrons in gaas/al/sub x/ga/sub 1-x/as quantum wells. *Physical Review B (Condensed Matter)*, 44:11345–52, 1991.

[49] M. V. Marquezini, J. Tignon, T. Hasche, and D. S. Chemla. Refractive index and absorption of gaas quantum wells across excitonic resonances. *Applied Physics Letters*, 73:2313–15, 1998.

[50] M. I. D'yakonov and V. I. Perel. Optical orientation in a system of electrons and lattice-nuclei in semiconductors. theory. *Zhurnal Eksperimental'noi i Teoreticheskoi Fiziki*, 65:362–76, 1973.

[51] M. Goldman. *Spin temperature and nuclear magnetic resonance in solids*. Claredon Press, 1. edition, 1970.

[52] W. Heller, A. Filoramo, Ph Roussignol, and U. Bockelmann. Direct measurement of exciton diffusion in quantum wells. *Solid State Elctronics*, 40:725–8, 1996.

[53] M. J. Snelling, A. S. Plaut, G. P. Flinn, A. C. Tropper, R. T. Harley, and T. M. Kerr. Spin relaxation in optically excited quantum wells. *Seventh International Conference on Dynamical Processes in Excited States of Solids*, 1990.

[54] A. Melliti, M. A. Maaref, and R. Planel. Exciton localization and interisland exciton diffusion in interrupted-growth gaas-alas quantum well. *Journal of Luminescence*, 78:25–31, 1998.

[55] Wu Qiang, R. D. Grober, D. Gammon, and D. S. Katzer. Imaging spectroscopy of two-dimensional excitons in a narrow gaas/algaas quantum well. *Physical Review Letters*, 83:2652–5, 1999.

[56] G. Bernatz, S. Nau, R. Rettig, H. Jansch, and W. Stotz. Experimental investigation of structures of interior interfaces in gaas. *Journal of Applied Physics*, 86:6752–7, 1999.

[57] K. Leosson, J. R. Jensen, W. Langbein, and J. M. Hvam. Exciton localization and interface roughness in growth-interrupted gaas/alas quantum wells. *Physical Review B (Condensed Matter)*, 61:10322–9, 2000.

[58] R. Grousson, V. Voliotis, N. Grandjean, J. Massies, M. Leroux, and C. Deparis. Microroughness and exciton localization in (al,ga)as/gaas quantum wells. *Physical Review B (Condensed Matter)*, 55:5253–8, 1997.

[59] D. Gammon, B. V. Shanabrook, and D. S. Katzer. Excitons, phonons, and interfaces in gaas/alas quantum-well structures. *Physical Review Letters*, 67:1547–50, 1991.

[60] U. Jahn, S. H. Kwok, M. Ramsteiner, R. Hey, H. T. Grahn, and E. Runge. Exciton localization, photoluminescence spectra, and interface roughness in thin quantum wells. *Physical Review B (Condensed Matter)*, 54:2733–8, 1996.

[61] W. Hanle. *Zeischrift für Physik*, 30:93, 1924.

[62] U. Fano. Description of states in quantum mechanics by density matrix and operator technics. *Reviews of Modern Physics*, 29:74–93, 1957.

[63] Landolt-Boernstein. *Semiconductor*. Springer, 1. edition, 1982.

[64] C. Weisbuch and C. Hermann. Optical detection of conduction-electron spin resonance in gaas, gainas, and gaalas. *Physical Review B (Solid State)*, 15:816–22, 1977.

[65] V. K. Kalevich, V. D. Kul'kov, and V. G. Fleisher. Optical cooling of the spin system of nuclei in a semiconductor lattice in a rotating system of coordinates. *Fizika Tverdogo Tela*, 22:1208–11, 1980.

[66] W. E. Carlos, S. G. Bishop, and D. J. Treacy. Nuclear-magnetic-resonance studies of strain in isovalently doped gaas. *Physical Review B (Condensed Matter)*, 43:12512–21, 1991.

[67] M.H. Cohen and F. Reif. Quadrupole effects in nuclear magnetic resonance studies of solids. *Solid State Physics*, 5:321, 1957.

[68] J. Winter. *C.R. Acad. Sci.*, 241:375, 1955.

[69] C. R. Bowers. Microscopic interpretation of optically pumped nmr signals in gaas. *Solid State Nuclear Magnetic Resonance*, 11:11–20, 1998.

[70] J. A. McNeil and W. G. Clark. Nuclear quadrupolar spin-lattice relaxation in some iii-iv compounds. *Physical Review B (Solid State)*, 13:4705–13, 1976.

[71] C.P. Slichter. *Principles of magnetic resonance*. Springer, 3. edition, 1990.

[72] V. V. Lemanov. Nuclear magnetic resonance in elastically deformed rock salt. *Soviet Physics Jetp*, 13:543–5, 1961.

[73] R. K. Sundfors, R. K. Tsui, and C. Schwab. Experimental gradient elastic tensors: Measurement in i-vii semiconductors and the ionic contribution in iii-v and i-vii compounds. *Physical Review B (Solid State)*, 13:4504–8, 1976.

[74] W. Voigt. *Lehrbuch der Kristallphysik*. Teubner, 1. edition, 1910.

[75] R. G. Shulman, B. J. Wyluda, and P. W. Anderson. Nuclear magnetic resonance in semiconductors. ii. quadrupole broadning of nuclear magnetic resonance lines by elastic axial deformation. *Physical Review*, 107:953–8, 1957.

[76] R. K. Sundfors. Experimental gradient-elastic tensors and chemical bonding in iii-v semiconductors. *Physical Review B (Solid State)*, 10:4244–52, 1974.

[77] G. C. Osbourn. Strained-layer superlattices from lattice mismatched materials. *Journal of Applied Physics*, 53:1586–9, 1982.

[78] C. G. Van der Walle. Band lineups and deformation potentials in the model-solid theory. *Physical Review B*, 39:1871–83, 1989.

[79] Landolt-Boernstein. *Technik*. Springer, 6. edition, 1964.

[80] D. J. Guerrier and R. T. Harley. Calibration of strain vs nuclear quadrupole splitting in ill-v quantum wells. *Applied Physics Letters*, 70:1739–41, 1997.

[81] K. A. Dumas, J. F. Soest, A. Sher, and E. M. Swiggard. Electrically induced shifts of the gaas nuclear spin levels. *Physical Review B (Condensed Matter)*, 20:4406–15, 1979.

[82] D. Gill and N. Bloembergen. Linear stark splitting of nuclear spin levels in gaas. *Physical Review*, 129:2399–2403, 1963.

[83] J. G. Kempf and D. P. Weitekamp. Method for atomic-layer-resolved measurement of polarization fields by nuclear magnetic resonance. *27th Conference on the Physics and Chemistry of Semiconductor Interfaces*, 2000.